Universiteit Utrecht

Data analysis from the beam test at DESY for the FoCal prototype

-

Alexandros Apostolou

July 24, 2013

Master Thesis
Report number: UU(SAP) 13-9

Supervisors:
Dr. Gert-Jan Nooren
Prof. Thomas Peitzmann

Utrecht University
Faculty of Science/Department of Physics and Astronomy
Institute for Subatomic Physics
Buys Ballot laboratory
PO BOX 80 000, 3508 TA Utrecht, The Netherlands

To my beloved grandmother

Abstract

FoCal, which stands for Forward Calorimeter, is a project to which the Subatomic Physics Institute of the Utrecht University contributes. The goal of FoCal project is the construction and development of a new high resolution electromagnetic calorimeter. This calorimeter will measure electromagnetic showers and tracks in the forward direction at the ALICE experiment at CERN, Switzerland. In this thesis, data taken from a beam test by the constructed FoCal prototype at DESY, Germany on March 2012 are analysed. Beams of pure electrons at 2 and 5 GeV were used. Two steps are followed in this analysis, for both different energy data sets: The first is the investigation of the longitudinal shower profiles in order to study the behaviour of the detector and calculate its energy resolution. Multiple methods are followed for detector calibration to improve the energy resolution. The second is the investigation of the lateral shower profiles which leads us in the calculation of the Moliere radius. Lateral profiles also help us to investigate the alignment of the prototype. In addition, some preliminary work with the scintillator trigger system and chip testing is also shown. All the results from the analysis are compared to the values calculated from the simulations and theory. The results from the analysis of the longitudinal and lateral profiles of the first testing of the FoCal prototype show that FoCal prototype behaves well as an electromagnetic calorimeter but the energy resolution that it shows is still away from what it was expected. Of course, modifications, changes and improvements can be made and the goals of the project could be probably reached.

Contents

Chapter 1

Introduction

Particle physics is the branch of the physics devoted to the constituents of matter and their fundamental interactions. So in a way it is the base in the pyramid of all the physical processes that take place in nature. The requirement for the detection of subnucleus particles and their properties has driven science to design particle detectors, i.e. calorimeters. Nowadays, many of the experiments made to investigate particles and their properties are called "accelerator" based experiments. The use of very complicated and expensive accelerators provides a more controlled environment for the experiments together with much higher rates of data acquisition. Calorimeters are used to investigate physical processes which are reconstructed from the created particles and their momenta in different particle collision events. Finding the momentum and the track of a particle can lead to particle identification and energy measurements. One of the most important properties of calorimeters is that their resolution increases with the energy of the incident particle. This property makes calorimeters an excellent device for particle physics experiments. Another significant advantage of calorimeters is their ability of "filtering". Usually an electromagnetic calorimeter stops all electromagnetically interacting particles (except muons), but it only partially stops hadrons. So if we place a hadronic calorimeter behind the electromagnetic calorimeter the first one won't measure any contamination from electrons or photons. The same argument holds for the most penetrating particles, i.e. the muons: after the hadronic calorimeter one expects to observe only muons. The two basic properties mentioned and even more make calorimeters an essential tool in high energy particle experiments.

The primary purpose of a calorimeter is the energy measurement of the particles traversing its body. In order to perform these measurements, several physical processes must be investigated. There are two large families of calorimeters, the electromagnetic and the hadronic. Electromagnetic calorimeters are optimized for energy measurement of leptons (mostly electrons and positrons) and photons. The showers caused by these particles are fully described by QED theory. On the other hand, the hadronic showers that occur in hadronic calorimeters are only partially described by QED. Now the strong interactions play an important role and determine the nature of the processes. In this section we will describe the relevant electromagnetic processes when particles traverse the matter. Moreover, we are going to describe how, due to these processes, a particle incident on matter can cause an electromagnetic shower. We will briefly refer to the characteristic parameters of a shower. We have to point out at this point that most parameters of a calorimeter in practice have a dependence on the Z value of the material of the absorber. Then we explain the problems one faces calculating the energy resolution and response of calorimeters and the fluctuations slipping into the measurements. The emphasis will be given on electrons and photons, since we're dealing an electromagnetic calorimeter. Finally, we will also briefly describe the mip (minimum ionizing particle) concept.

1.1 Sampling and homogeneous calorimeters

Calorimeters are distinguished according their composition into two classes [1]:

1. Homogeneous calorimeters, in which the absorber and the active signal producing medium are the same thing.
2. Sampling calorimeters, in which these two roles are played by different media.

Homogeneous calorimeters

The main advantage of these detectors is their excellent energy resolution, explained by the fact that the whole energy of a particle is deposited in the active medium. On the other hand, homogeneous calorimeters are not suitable for position measurements and particle identification because they cannot be easily segmented either longitudinally or laterally. In addition, since these devices use materials with a large interaction length, make them unsuitable for being used as hadronic calorimeters. Homogeneous calorimeters are widely used in neutrino and astroparticle physics experiments in which large volumes are needed.

Homogeneous calorimeters can be divided into four classes [1]:

- Semiconductor calorimeters: In this case, the production of electron-hole pairs in the material and more specifically in its conduction band gives rise to an electric signal. These detectors provide an excellent energy resolution. Examples of semiconductor materials used are (mostly) silicon and germanium.
- Scintillator calorimeters: The medium is a material where the ionization tracks from the particles produce light. Examples of materials used are BGO, CsI, and PbWO4 crystals.
- Cherenkov calorimeters: The medium in this case is a transparent material in which relativistic electrons in the shower produce Cherenkov photons. As a result, the signal collected is in the form of light. Lead-glass calorimeters are a widely used example.
- Noble liquid calorimeters: The medium is a noble gas (Ar, Kr, and Xe) operated under very specific conditions (e.g. cryogenic temperature). In noble liquid calorimeters it is possible to collect both ionization and scintillation signals.

Sampling calorimeters

We mentioned before that the energy resolution of sampling calorimeters is generally worse than that of homogeneous calorimeters. The main reason for this is the presence of sampling fluctuations originating from the absorber layers coming in between the active layers. The energy resolution is typically in the range $5 - 20\%/\sqrt{E(GeV)}$ for electromagnetic calorimeters. On the other hand, sampling calorimeters are relatively easy to segment longitudinally and laterally, and therefore they have most of the times better space resolution and better capability in particle identification than homogeneous detectors.

Sampling calorimeters are classified according to the type of the active medium [1]:

- Scintillation calorimeters: These sampling calorimeters use organic (plastic) scintillators arranged in layers or plates. The signal is collected in the form of light. They are relatively cheap and can be constructed in a large variety of shapes and volumes. Moreover, they can be easily segmented, have a relatively fast response and an acceptable light yield.

- Gas calorimeters: Gas calorimeters have been widely used mainly because of their low cost and segmentation possibilities. The signal here is collected in the form of electric charge. However, they have a mediocre energy resolution. In addition, their stability and uniformity of the response are modest, because the gain is very sensitive to several factors such as the gas pressure, the gas temperature, the high voltage settings, etc.

- Solid-state calorimeters: In most of the cases of solid-state sampling calorimeters the active medium is silicon. The signal is collected in the form of electric charge. The main advantage of these detectors compared to the gas calorimeters is that the density of the active layers is 1000 times larger. This allows the construction of more compact devices with a much higher signal-to-noise ratio. This high signal-to-noise ratio relies also on the fact that, for example, only 3.6 eV are needed to produce an electron-hole pair in Si, while for a gas the is almost 30 eV. The main disadvantages of this technique are the high cost, which makes it unaffordable to use in large-scale detectors, and the poor radiation resistance. Silicon sampling calorimeters often have a very dense absorber like tungsten.

- Liquid calorimeters: Liquid sampling calorimeters are widely used in high energy physics experiments mainly with argon as the active medium. Liquid sampling calorimeters show a relatively good uniformity and they are also easy to calibrate because the active medium is homogeneously distributed inside the volume. The produced signal is also in principle uniform and doesnt suffer from several variations. They have good energy resolution and a stable response with time. They are also not very sensitive to radiation. The drawbacks are the cryogenic equipment, which complicates the operation and increases the cost of the detector and that liquid calorimeters have a relatively slow charge collection. The signal in liquid calorimeters is collected in the form of electric charge.

1.2 Passage through matter and energy loss

In this part the various processes contributing to the energy loss of photons and charged particles are being reviewed. Charged particles lose their energy continuously. Photons on the other hand might traverse a significant distance through a material without suffering from an interaction. The most characteristic value of the physical processes for all the particles is the amount of energy loss per unit of traversed distance (radiation length) dE/dx. The mean rate of energy loss (or stopping power) is given by the Bethe-Bloch equation [2]

$$-\frac{dE}{dx} = Kz^2\frac{Z}{A}\frac{1}{\beta^2}[\frac{1}{2}ln\frac{2m_ec^2\gamma^2\beta^2T_{max}}{I^2} - \beta^2 - \frac{\delta(\beta\gamma)}{2}] \tag{1.1}$$

where K is a constant, Z is the atomic number of the absorber, A is the atomic weight of the absorber, m_e the mass of the electron, $\delta(\beta\gamma)$ is the density effect correction to ionization energy loss, I is the mean excitation energy, T_{max} is the maximum kinetic energy which can be imparted to a free electron in a single collision, and β is equal to v/c.

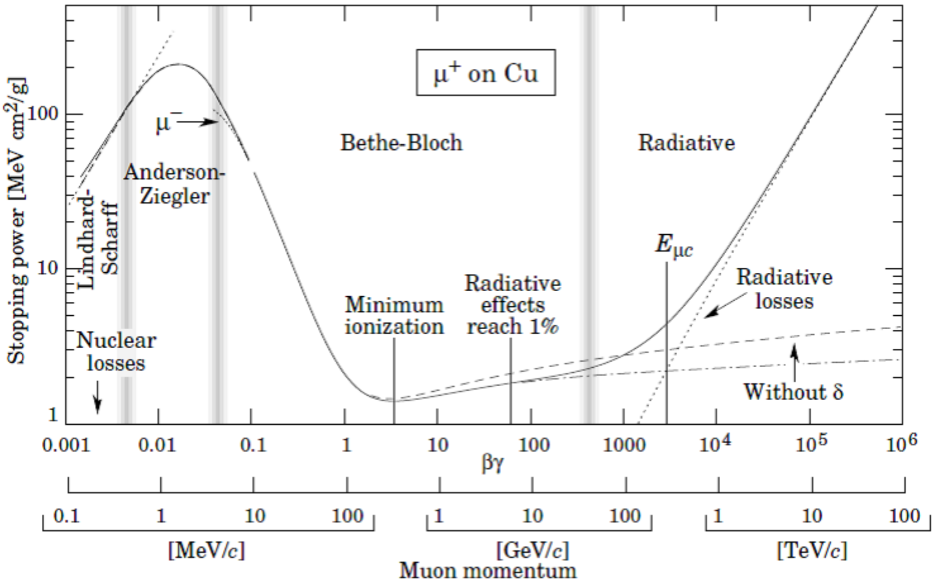

Figure 1.1: Energy loss (stopping power) for positive muons in copper as a function of the parameters $\beta\gamma$.[2]

The processes that mostly contribute to the energy loss for charged particles are [2]:

- Ionization: The charged particle knocks the electron of an atom out of its bound state. As a result the atom is ionized.
- Excitation: A charged particle may excite an atom without ionizing it. The atom goes into an excited state due to the particle traversing it. The energy loss is equal to the amount of light emitted when the atom returns back to its ground state.
- Bremsstrahlung: When a high energetic charged particle traverses a strong electric field it will emit photons. In principle it is the deceleration of the charged particle when it is being deflected.
- Cherenkov radiation: The amount of energy loss of a particle due to this process is negligible. Nevertheless, this effect is useful for particle detection. Cherenkov radiation is emitted when a particle passes a dielectric medium at a speed higher than the phase velocity of light in that medium.
- At high energies, δ rays are produced. These are high energetic electrons that got knocked out of their atomic orbit. These electrons have enough energy to ionize other atoms.

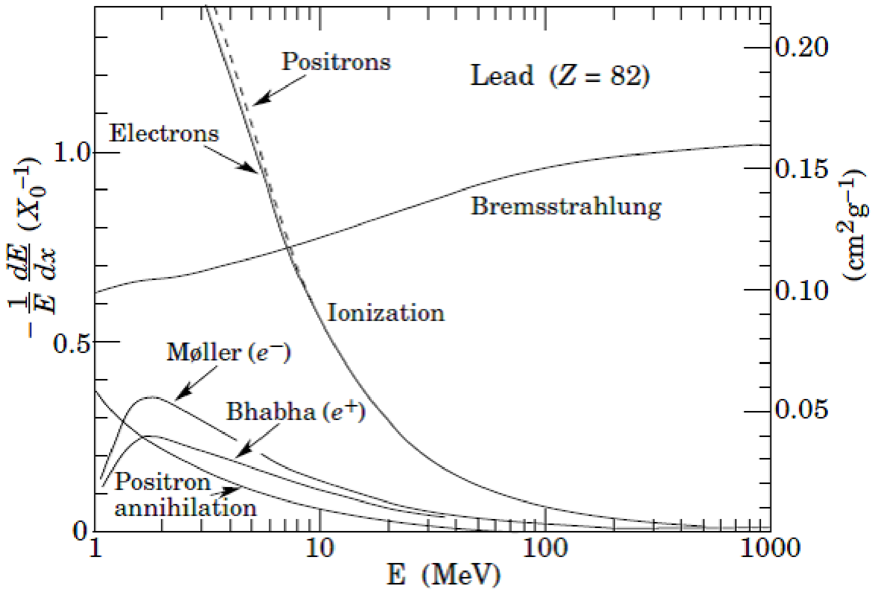

Figure 1.2: Fractional energy loss per radiation length in lead as a function of energy.[2]

In figure 1.2 the relative importance of the various processes as function of the energy of the particle is shown. At low energies ($\leq$ 10 MeV), ionization is the dominant process of energy loss, while for energies above 10 MeV Bremsstrahlung is the dominant process (mostly for dense materials). The contributions for positrons are almost equal with these from electrons. Electron and positron scattering is considered as ionization when the energy loss per collision is below 0.255 MeV, and as Moller (for electrons) and Bhabha (for positrons) scattering when it is above this value.

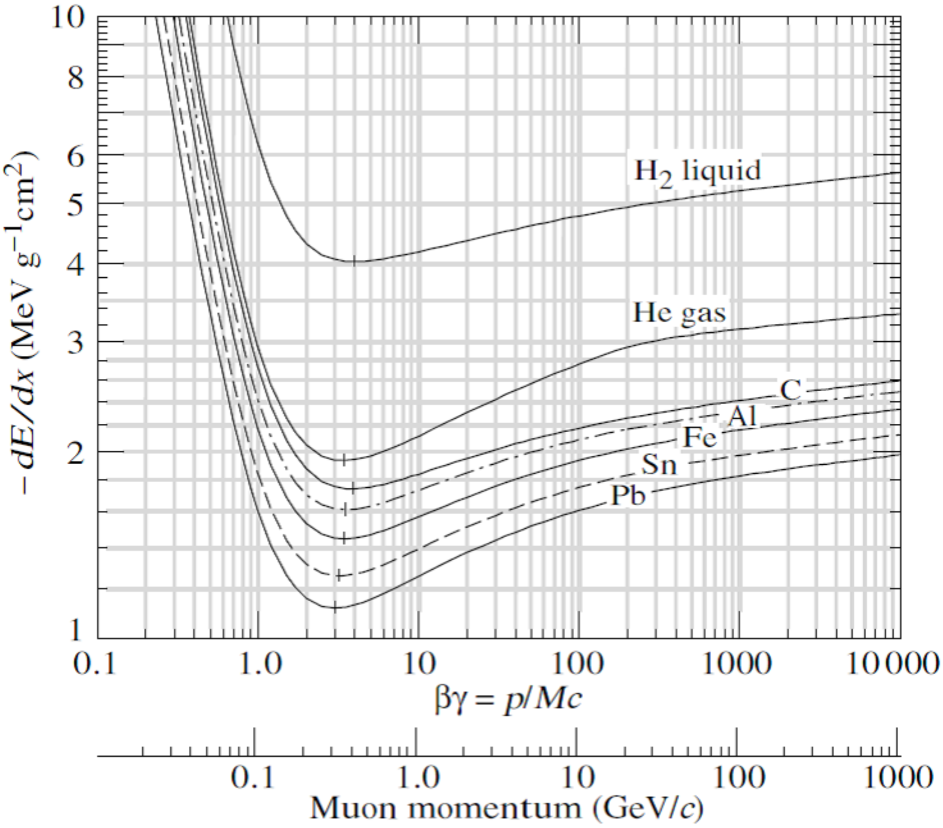

Figure 1.3: Energy loss in various materials as a function of parameters $\beta\gamma$.[3]

The processes of which photons are most likely to suffer are [2]:

- Photoelectric effect: An atom absorbs a photon and emits an electron. It returns to its ground state by emitting another electron or an X-ray. This process strongly depends on the atomic number Z.
- Compton scattering: A photon interacts with an (atomic) electron. Part of the photons energy is transferred to the scattering electron. After this process a photon has significantly lower energy.
- Pair production: When a photon, with (at least) twice the rest mass of an electron, traverses a strong electric field it might produce an electron- positron pair. The photon is then disappeared. This process becomes dominant for materials with a high Z value and high photon energies. The produced leptons (electrons and positrons) lose their energy subsequently as described above.
- Photo nuclear interactions: In these reactions the target nucleus is broken up due to its interaction with the photon.

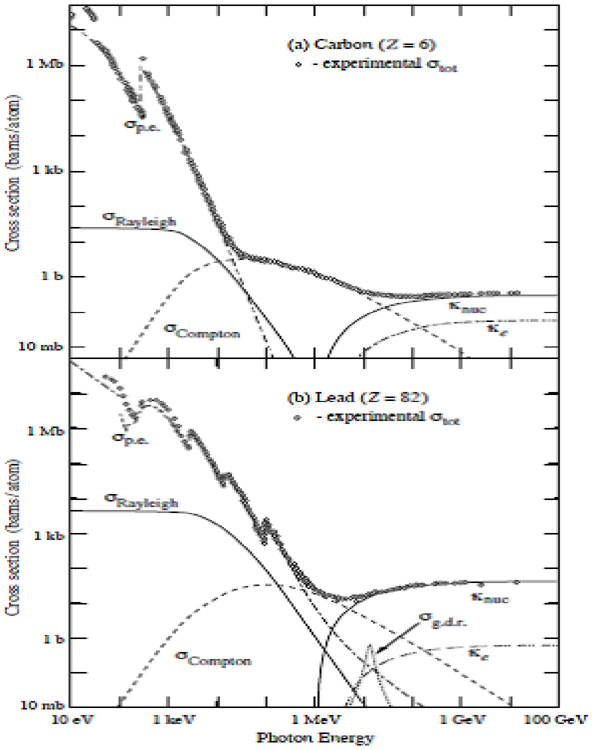

Figure 1.4: Photon total cross sections as a function of energy in carbon and lead, showing the contributions of different processes.[2]

1.3 Electromagnetic cascades

When photons or leptons (electrons and positrons) traverse an absorber they create a shower of particles. In this way they deposit their energy in the medium. A high energetic photon might travel approximately one radiation length inside the detector before it converts to an electron-positron pair. Then the leptons interact and produce either Bremsstrahlung photons or a pair of photons via annihilation (positrons). These in turn can, if they are energetic enough, convert themselves again. Otherwise these photons interact and lose their energy via the other processes (scattering). (see figure 1.4)

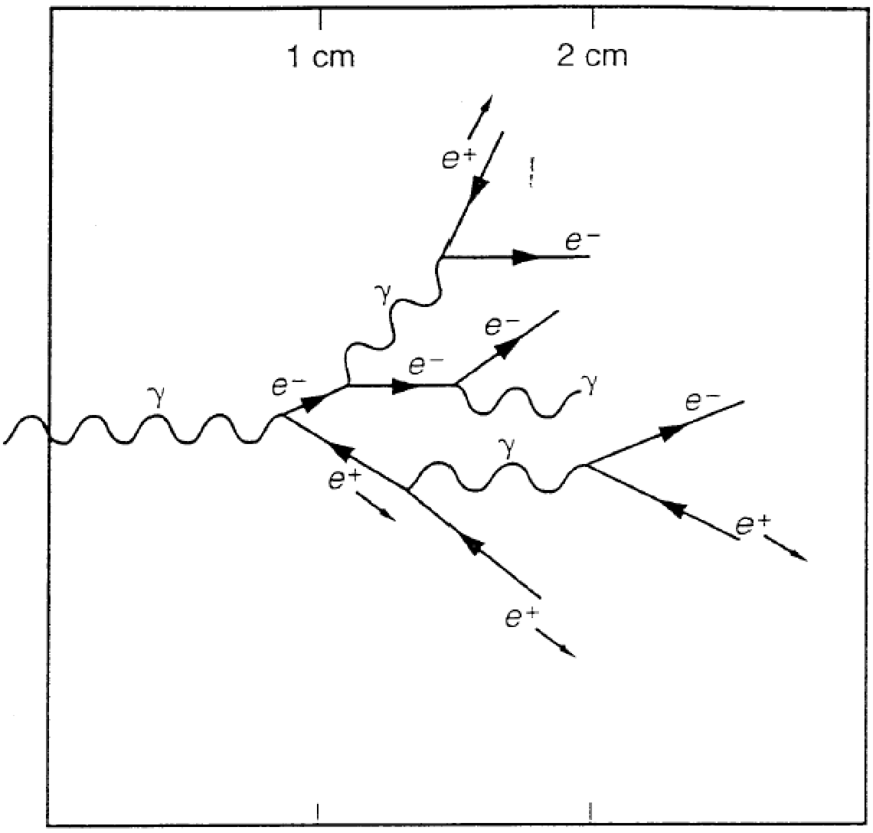

Figure 1.5: Illustration of an e/m shower produced by a photon.[4]

In the beginning stadium of the shower, per every collision event, new particles get created. At high enough energies, in the particle shower the number of particles is approximately doubled in every process/step. The electron and positron each emit one bremsstrahlung photon after another radiation length. Each particle has an energy E equal to $E(n) = E_0/2n$ where E_0 the initial energy of the particle and n the number of steps in the shower [4]. There is a depth where the average energy of the shower particles is such that on average no new particles are formed any more. This point is called the "shower maximum". After this point the particles lose their energy until at the end the photons get absorbed via the photoelectric effect and the electrons deposit their energy by ionization. The main features of electromagnetic showers (e.g. their longitudinal and lateral sizes) can be described in terms of one parameter, the radiation length X_0, which depends on the characteristics of the material [5]

$$X_0(g/cm^2) = \frac{716gcm^{-2}A}{Z(Z+1)ln(\frac{287}{\sqrt{Z}})} \tag{1.2}$$

where Z and A are the atomic number and weight of the material, respectively.

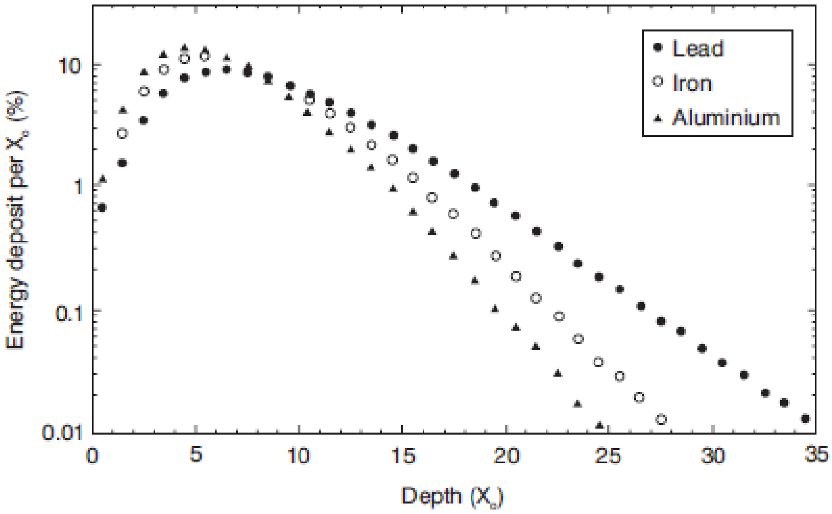

Figure 1.6: Longitudinal profiles of 10 GeV electron showers developing in lead, iron and aluminium.[1]

The radiation length affects the rate at which electrons lose energy by bremsstrahlung, since it represents the average distance x that an electron needs to travel in a material to reduce its energy to 1/e of its original energy E_0 [5]

$$< E(x) >= E_0 e^{\frac{-x}{X_0}} \tag{1.3}$$

Similarly, a photon beam of initial intensity I_0 traversing a block of material is absorbed mainly through pair production [5]. After travelling a distance $9/7X_0$, its intensity is reduced to 1/e of the original intensity

$$< I(x) >= I_0 e^{\frac{-7x}{9X_0}} \tag{1.4}$$

One more important concept is the critical energy, ϵ. There are two slightly different definitions which are used to define this concept. In the first one, is the energy at which the electron ionization losses and bremsstrahlung losses become equal [5]. This energy depends on the features of the material and is approximately given by

$$\epsilon = \frac{610MeV}{Z + 1.24} \tag{1.5}$$

In the second definition, critical energy is the energy at which the ionization loss per X_0 equals the electron energy E

$$\frac{dE}{dx}(ionization) = \frac{E}{X_0} \tag{1.6}$$

It is well known that average longitudinal shower profiles can be described by a gamma distribution [6]

$$< \frac{1}{E}\frac{dE(t)}{dt} >= f(t) = \frac{bt^{\alpha-1}\beta e^{-\beta t}}{\Gamma(\alpha)} \tag{1.7}$$

where the center of gravity t and the depth of the maximum can be calculated from the shape parameter α and the scaling parameter β according to

$$\tau = \frac{\alpha}{\beta} \tag{1.8}$$

and

$$T = \frac{\alpha - 1}{\beta} \tag{1.9}$$

Eq. 7 can be also equivalently written as follows [5]

$$\frac{dE}{dt} = E_0 \beta \frac{\beta t^{\alpha-1} e^{-\beta t}}{\Gamma(\alpha)} \tag{1.10}$$

where $t = x/X_0$ is the depth inside the material in radiation lengths and α and β are parameters related to the nature of the incident particle. The shower maximum, i.e. the depth at which the largest number of secondary particles is produced, is approximately located at

$$t_{max} = ln \frac{E_0}{\epsilon} + t_0 \tag{1.11}$$

where the t_{max} is measured in radiation lengths, ϵ is the critical energy, E_0 is the incident particle energy, and t_0 = -1(+1) for electrons (photons). This formula shows the logarithmic dependence of the shower length, and therefore draws the detector thickness needed to absorb a shower, in relation to the incident particle energy.

The calorimeter thickness containing 95% of the shower energy is approximately given by [5]

$$t_{95\%} = t_{max} + 0.08Z + 9.6 \tag{1.12}$$

where t_{max} and $t_{95\%}$ are measured in radiation lengths.
A measurement of the transverse size, integrated over the full shower depth, is given by the Moliere radius (R_m), which can be approximated by [5]

$$R_m(g/cm^2) = 21(MeV) \frac{X_0}{\epsilon(MeV)} \tag{1.13}$$

It represents the average lateral deflection of electrons at the critical energy after traversing one radiation length. On average, about 90% of the shower energy is contained in a cylinder of radius 1 R_m. Since for most calorimeters the Moliere radius is of the order of a few centimetres, one can conclude that electromagnetic showers are quite narrow. In addition, a showers transverse size is roughly energy independent. The parts of a segmented calorimeter must be comparable in size to (or smaller than) one Moliere radius if the calorimeter is used for precision measurements of the shower position.

1.4 Fluctuations in calorimeters

In an electromagnetic calorimeter the measurement of energy is based on the principle that the energy released in the detector by the particles of the shower, mainly through ionization and excitation, is always proportional to the energy of the incoming incident particle. The intrinsic energy resolution of an ideal calorimeter, i.e. a calorimeter with infinite size and no response deterioration due to instrumental effects (problems in signal collection, mechanical non-uniformities etc.) is proportional to the total track length of the shower [5]

$$\sigma(E) \div \sqrt{L_0} \tag{1.14}$$

where the symbol $\div$ is showing the proportionality. One can also mathematically derive the expression for the energy resolution [5]

$$\frac{\sigma(E)}{E} \div \frac{1}{\sqrt{L_0}} \div \frac{1}{\sqrt{E_0}} \tag{1.15}$$

The actual energy resolution of a real calorimeter is influenced by other contributions/fluctuations and can be written in a more general way as [5]

$$\frac{\sigma(E)}{E} = \frac{a}{\sqrt{E}} \oplus \frac{b}{E} \oplus c \tag{1.16}$$

where the symbol $\oplus$ indicates the quadratic sum.
The first term on the right-hand side is called the "stochastic term", and includes the shower intrinsic fluctuations. The second term is called the "noise term" and the third term is the "constant term". Each term of the above equation has different importance which depends on the energy of the incident particle. Therefore, a calorimeter resolution and response can vary for experiments operating in different energy ranges since every time there are different contributions. These contributions are discussed below [5].

Stochastic term

This term is due to the fluctuations related to the physical development of the shower. In homogeneous calorimeters intrinsic fluctuations are small because the energy deposited in the active volume of the detector by the beam of particles does not vary event by event. On the other hand, in sampling calorimeters the energy deposited in the active medium fluctuates event by event because the active layers are interleaved with the absorber layers. These fluctuations are called "sampling fluctuations" and represent the most important limitation to the energy resolution of this kind of detectors. The observed fluctuations are due to variations in the number of charged particles N_{ch} which transverse the active layers. This number is proportional to E_0/f where f is the thickness of the absorber layers in radiation lengths. Thus, the contribution to the energy resolution is

$$\sigma(E) = \frac{1}{\sqrt{N_{ch}}} \tag{1.17}$$

If someone wants to achieve energy resolution comparable to that of typical homogeneous calorimeters, he needs to have absorber thickness at least a few percent of one radiation length. The typical energy resolution of sampling electromagnetic calorimeters is in the range $5 - 20\%\sqrt{E(GeV)}$. Another important parameter of the sampling calorimeters is the sampling fraction f_{samp}, which is equal to

$$f_{samp} = \frac{E_{mip}(active)}{E_{mip}(active) + E_{mip}(absorber)} \tag{1.18}$$

where E_{mip}(active) and E_{mip}(absorber) indicate the energies deposited by an incident minimum-ionizing particle in the active part and in the absorber part of the detector respectively.

Noise term

The source of this contribution to the energy resolution comes from the electronic noise of the readout and depends on the detector technique and on the features of the readout mechanism. In calorimeters in which the signal is collected in the form of light, such as homogeneous calorimeters or scintillator-based sampling calorimeters, one can achieve really low levels of noise. This can be easily succeeded since most of the times the first step of the electronic readout procedure is a photosensitive device, a phototube, which provides a high-gain multiplication of the original signal with almost no noise. On the other hand, the noise is larger in detectors in which the signal is collected in the form of charge because the first stage of the readout chain is usually a pre-amplifier which adds noise to the signal. The noise contribution to the energy resolution increases with decreasing energy of the incident particles (see eq 1.16) and at energies below a few GeV may become dominant. In sampling calorimeters the noise term can be decreased by increasing the sampling fraction, because the larger the sampling fraction, the larger the signal produced from the active part of the calorimeter and therefore the higher the signal-to-noise ratio.

Constant term

This term includes contributions which do not depend on the energy of the particle. Instrumental effects that cause variations of the calorimeter response produce non- uniformities to the detectors behaviour. These non-uniformities can originate from the detector geometry (for instance if there is a misalignment between the absorber and active layers), from imperfections in the detector mechanical structure, errors in the readout system, temperature reasons, detector ageing, radiation damage, etc. The problems that might arise due to the causes mentioned can be solved to a large extent if they behave in a periodic pattern, so if they show the same behaviour for several different measurements and events, as is the case if they are related to the detector geometry, or if they originate from the readout chain. On the other hand, other effects such as mechanical imperfections are randomly distributed and therefore more difficult to correct.

Additional contributions to the constant term

Examples of additional contributions are [5]:

- Longitudinal leakage. Space lack and cost constraints, limit the thickness of a calorimeter operating in a high-energy physics experiment. Therefore high energetic showers can lose part of their energy beyond the end of the active calorimeter volume. This leakage fluctuates event by event and as a result the energy resolution gets worse. This effect can be in part corrected by weighting the energy deposited by each shower in the calorimeter and especially in its last part (in the tail of the shower).

- Lateral leakage. Usually, in order to minimize the noise contribution coming from the electronics, a relatively small volume of calorimeter cells is used to reconstruct an electromagnetic shower. As a consequence, a fraction of the shower energy can be lost outside this volume. This fraction fluctuates event by event (same as longitudinal leakage), and therefore introduces an additional problem in the energy measurements. Thus, the choice of the optimum lateral size is obviously very critical for the energy measurements.

- Other losses. Calorimeters are most of the times placed on complicated mechanical structures and equipped with cables and electronics. In addition, when operating inside a bigger detector system or a test area, they are usually placed after other detectors and/or tracking devices.

As a consequence, electrons and photons coming from the interaction point have to traverse a significant amount of inactive material before reaching the active volume of the calorimeter. In this way the particles lose part of their energy before reaching the calorimeter. The energy lost due to this reason fluctuates event by event, and this can lead to deterioration of the energy resolution. There are several techniques to recover part of these losses. Moreover dead (inactive) regions are often present inside the calorimeter volume because detectors are usually built part by part and in some cases the active area of one part of the detector is overlapping or covering the active area of another part of the detector. The quality of the energy measurement is reduced when there is a shower developing in these areas. As a result, the energy resolution of the calorimeter might become worse. This can have an impact also on the measurement of the amount of energy passing the detector.

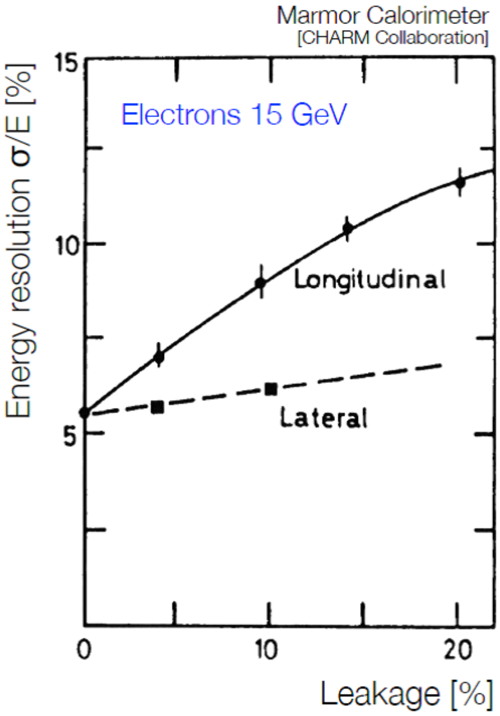

Figure 1.7: Lateral and longitudinal leakage versus energy resolution for electrons with energy 15GeV in the Marmor calorimeter, CHARM collaboration.[3]

1.5 The minimum ionizing particle and the muon

A minimum ionizing particle (or MIP) is a particle whose mean energy loss rate dE/dx through matter is close to the minimum. In practice such a particle is really a theoretical concept. This concept occurs when the kinetic energy of particles is at least twice larger than their rest mass. The electrons (or protons) can be considered as minimum ionizing particles when their kinetic energy is greater than 1 MeV [7]. Since the ionization losses of these particles are only weakly dependent on their momentum, it is generally accepted that a minimum ionizing particle loses its energy in a constant pace along its path through the absorber. In our case a minimum ionizing particle loses the same amount of energy in every layer from the beginning of its track through the detector till the end. For most of the times a low energetic - at the order of GeV - muon is considered to be a MIP. As one can see from figures 1.1 and 1.6 the MIP is found in the region of $\beta\gamma$= 3-4. The concept of the MIP has many applications in calorimeters (calculating sampling factors etc.).

Chapter 2

The FoCal calorimeter

2.1 Physics motivation

The Forward Calorimeter is a possible upgrade of the ALICE (A Large Ion Collider Experiment) experiment at the CERN LHC, Switzerland. It is a finely granular silicon-tungsten calorimeter capable of covering pseudorapidities up to $\eta = 5$. This new calorimeter will provide unique capabilities to study small-x gluon distributions via direct photon detection and will also improve the capabilities of ALICE for more general photon and jet measurements [8]. In this way, one can study not only the properties of hot and dense partonic matter, but also the cold dense partonic matter. The FoCal also will have unique capabilities to investigate Parton Distribution Functions (PDFs) in a new regime of very small x-Bjorken and low Q^2.

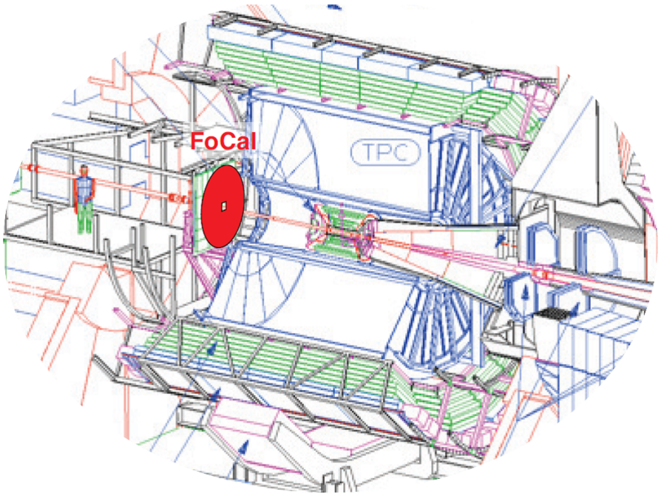

Figure 2.1: Position of the FoCal calorimeter in the ALICE detector at CERN, Switzerland.[9]

The investigation of the PDFs is the primary physics objective of the FoCal by providing high precision measurements of direct photons in p+p and p+A collisions. The FoCal will also add capabilities to measure jets, as well as coincident gamma-jet and jet-jet in the same reactions, providing further constraints on small x PDFs.
A key feature of FoCal is the ability to reconstruct neutral pion decays at forward rapidity and up to large transverse momenta $p_T > 20\mathrm{GeV/c}$. This not only provides a precise measurement of π^0 production, which is the dominant background for the direct photon measurement, but also allows for a direct rejection of decay photons [8]. The typical opening angles of π^0 decays at forward rapidity are relatively small, due to the longitudinal Lorentz boost. Such particle decays can be reconstructed with a high-granularity compact silicon-tungsten sampling electromagnetic calorimeter with ability of longitudinal segmentation.

Table 2.1: Pseudo rapidity ranges and granularity of existing forward calorimeters at LHC and the ALICE FoCal proposal.[8]

	ATLAS Inner Wheel	**CMS End-Cap**	**LHCb Ecal**	**ALICE FoCal @ 3.5m**	**ALICE FoCal @ 8m**
η range	2.5-3.2	1.5-3.0	1.8-4.3	2.5-4.5	3.3-5.1
Gran.(deg)	5.7	0.5	≥ 0.18	≈ 0.016	≈ 0.007

To sum up the new capabilities of the FoCal calorimeter which will in turn enhance the ALICE detector capabilities we can mention:

- measurements of direct photons and jets from parton-parton scattering.
- measurements of thermal photons for elliptic flow studies.
- distinguishing neutral pions and photons in a rapidity and transverse momentum range significantly beyond existing detectors.
- improvement of the general capabilities of ALICE for measurements involving direct photons, pions and other neutral hadrons, as well as jets in much higher rapidities.

The most important demand for the calorimeter that is imposed by these conditions is the high and spatial resolution.

2.2 Current design of FoCal prototype

The Utrecht Focal group has built a prototype sampling calorimeter which has been tested to several beam tests at CERN facilities, Switzerland and DESY facilities, Germany. In the construction of the prototype many members of the technical staff of Utrecht University and Nikhef (Amsterdam) took part.
The shape of the prototype is a rectangular parallelepiped. It consists of 24 layers of tungsten (absorber) and silicon (active medium). In each layer tungsten and silicon have a thickness of 3.3 mm and 1 mm respectively. The length of the prototype is 10 cm and its transverse size is a square shape of 40 x 40 mm. The idea behind the prototype is that it must be thick for photons and thin for hadrons. Both longitudinal and transversal sizes are carefully chosen (based on equations 1.2, 1.5, and 1.11-1.13) so that the prototype can contain a (full) shower of tens of GeV. The estimated Moliere radius is 11 mm with a layer thickness of 0.97 X_0 (24 layers correspond to almost 24 X_0). For tungsten we have Z=74, A=184, and for silicon Z=14, A=28. The expression for the radiation length of a mixture of materials is

$$\frac{1}{X_0} = \sum V_i/X_i \tag{2.1}$$

where V_i and X_i are respectively the volume fraction and the radiation length of the different materials. Thus for the FoCal detector (we consider only tungsten and silicon as materials and not air,glue etc.) the radiation length is calculated as follows

$$\frac{1}{X_0} = \frac{0.87}{3.5\text{ mm}} + \frac{0.04}{93.6\text{ mm}} \approx 4\text{ mm} \tag{2.2}$$

which is almost equal to the thickness of each layer as mentioned before in this paragraph. The same procedure is followed for the Moliere radius but this time instead of X_i we put the Moliere radius of each material as

$$\frac{1}{R_m} = \frac{0.87}{9.3\text{ mm}} + \frac{0.04}{48\text{ mm}} \approx 11\text{ mm} \tag{2.3}$$

To achieve such a small Moliere radius, while having enough layers for an acceptable sampling fraction, a highly longitudinally compact design is required. If we do the same for the maximum shower position according to eq. 1.12 we find for the 5 GeV

$$t_{max} = ln\frac{5000\text{ MeV}}{9.2\text{ MeV}} - 1 \approx 5.3X_0 \tag{2.4}$$

The choice of the tungsten as the most ideal material was due to the fact that we need both small radiation length and Moliere radius, while at the same time large nuclear interaction length. So looking at the table of atomic and nuclear properties of the materials from [3], one can see that tungsten is generally the most suitable candidate. Moreover, silicon can be very thin and this allows keeping the effective R_m still very small. Thus, a Si/W sandwich structure is ideally suited for the requirements of FoCal.
Each layer of the prototype contains:

- 4 2x2 cm MIMOSA23 chips
- 4 printed circuit boards on which the MIMOSA23 chips are mounted
- 4 stainless steel spacers
- 2 square tungsten plates on which the printed circuit boards (PCB's) are mounted
- 2 tungsten filler plates
- Several internet cables for data transfer and temperature monitoring

In two of the sides of the tower we have placed copper plates responsible to cool the chips using a liquid cooling mechanism (see figure 2.3a upper left image).

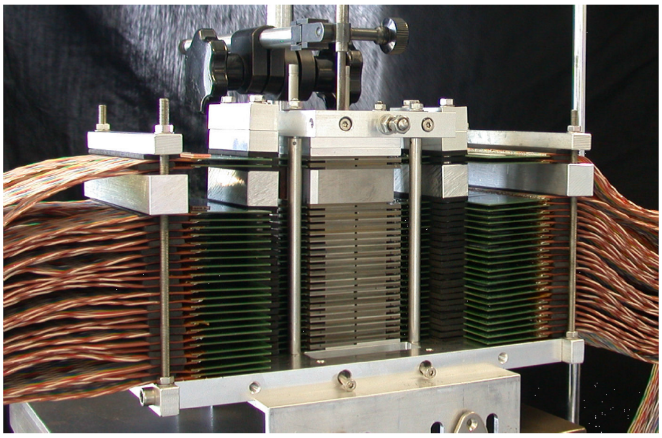

Figure 2.2: The group prototype. In the center of the body of the prototype one can see the tungsten plates while left and right the PCB's where the MIMOSA23 chips are connected. The cooling system of copper plates is not placed. It can be clearly seen in figure 2.3a upper left.[10]

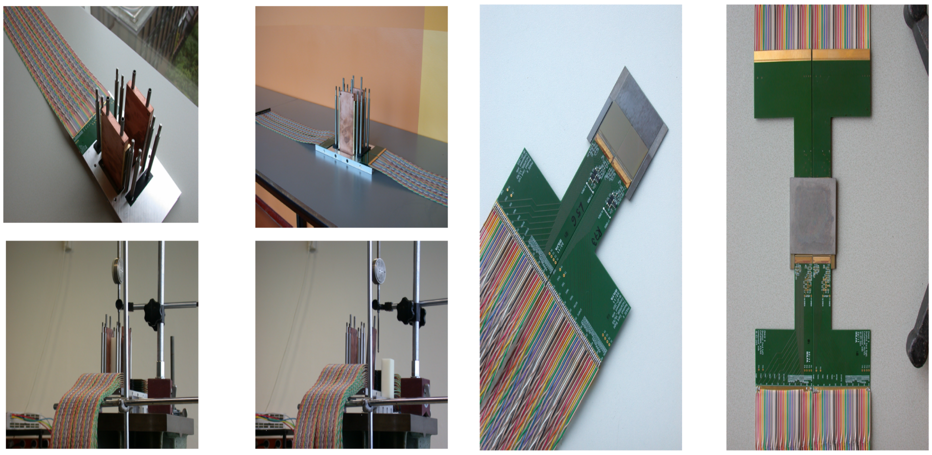

Figure 2.3: a)Assembly of the tower of the FoCal prototype with the copper plates used for cooling seen in upper left image and b)MIMOSA chips mounted on PCBs, with two chips with a tungsten plate mounted in the left one and a complete layer in the right one.[10]

The MIMOSA23 chip is a so called Monolithic Active Pixel Sensor (MAPS). It is a member of the CMOS family (Complementary MetalOxideSemiconductors) chips designed for the measurement of ionizing radiation. These kinds of semiconductors are often used in high energy physics experiments. The most significant reasons for selecting MAPS is that they are integrated circuits and therefore relatively cheap [10]. In addition they show extremely high granularity and there is a potential for extreme positional resolution. Last but not least by using MAPS one can exploit the pixel counting (i.e. the pixels firing each time) as an option for calculating the energy response of the calorimeter. The active area of the MIMOSA23 chips consists of 640 x 640 square pixels. Each of these pixels has a surface of 30μm x 30μm. The small pixel pitch of 30 μm allows very fine sampling of the shower core. The whole FoCal prototype set up with 24 layers has almost 40 million pixels in total. On the left side of the MIMOSA23 chip a wide strip contains the row drivers that manage the readout process and at the bottom a similar wide strip is responsible for the readout logic. In this zone each column is connected to a discriminator whose characteristics can be manually adjusted, that converts the collected charge of a pixel to a single bit so that this bit can later be used in data read out. At the bottom edge of the readout zone one finds the electrical connections to the PCBs of the readout channels, power supply, etc. Every chip is read out in 640μsec by a ”switch” which is called rolling shutter.

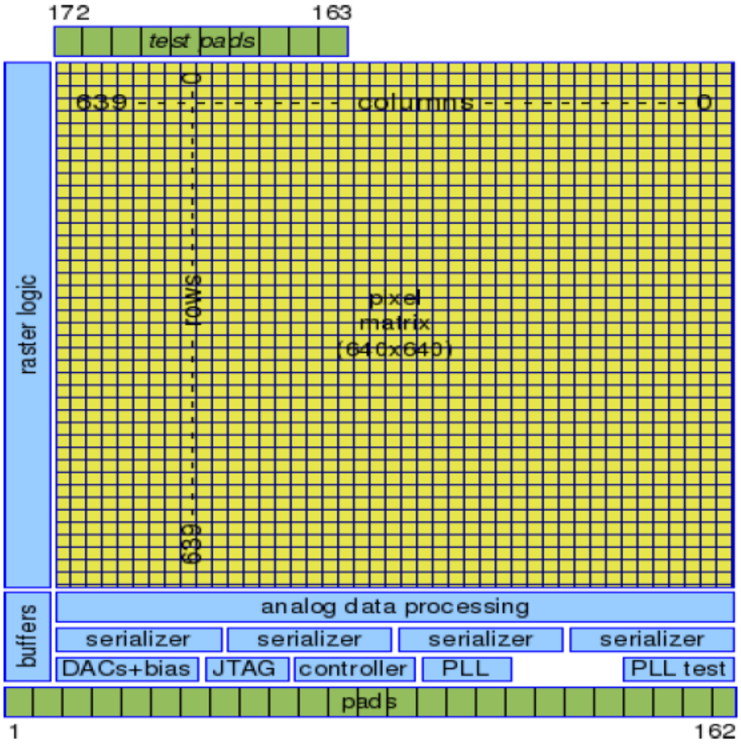

Figure 2.4: MIMOSA23 chip schematic portrayal. The active area of the chip is yellow coloured while the rest is called ”dead” area.[10]

Every individual MIMOSA23 chip has 4 output channels. Every channel contains 160 columns of the total 640 divided into 4 subgroups of 40 columns of the pixel array. Now the first 4 bits on a channel are the bits in the first column of every group. The next 4 bits are the bits in the second column of each group etc. The 96 channels of every 24 chips are connected to a concentrator board and this in turn to a complicated FPGA (Field Programmable Gate Array) system called Spartan6 [11]. The Spartan task is to synchronize the data of the different chips. Having in total 96 chips in the FoCal prototype, four Spartans are used. After data being processed by the Spartans these 96 channels continue to the Virtex6 boxes [9]. There are two Virtex6 boxes in total in each of which a pair of Spartans6 is connected. The Virtex6 box is another FPGA system that sequences the data from the Spartans6 and drives it to memory. The final step contains the Virtex6 board that stores and sequences the incoming bits and sends them to final storage in the memory of the DAQ (figure 2.5). The trigger data coming from the scintillator system are also being sent in the Virtex6 and follow the same route to the DAQ computer [11].

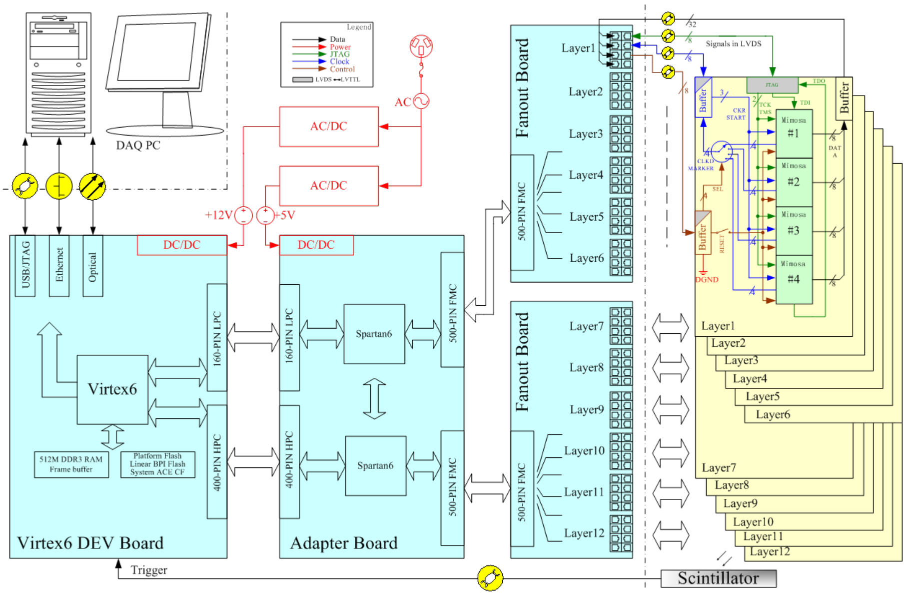

Figure 2.5: Schematic of the data processing procedure from FoCal to the DAQ computer for 12 layers (48 channels). The scintillator grey box used for the trigger is for us the scintillator system consisted of several scintillators.[11]

The data are read in a continuous way and being saved in frames. There are two kind of frames, the triggered and the triggerless. With the help of the external trigger system we keep the data we want to analyse in the triggered frames. Each trigger creates its own triggered frame. Frames can be visualized as a big column in which each frame is an element. So, we have one frame after the other and each one contains data from the showers. Each frame is being read in 640μsec (it is 640μsec "long"). What we want is to avoid reading the same data (hits) more than one time. So if there is a trigger that occurs in a time window less than 640μsec from the previous trigger, we skip reading its frame. This can be succeeded by applying in our data an extra condition which is called the "pile-up" condition.

2.3 Beam test DESY

In this section, some preliminary work done before and during the beam test at DESY is described. This work includes tests on the trigger system which uses scintillators, results form the trigger data obtained from the beam test and finally results from the MIMOSA23 chip testing. In figure 2.6 one can see the test set up. A collimator was used to make the beam thinner, together with a combination of five scintillators (front, back, present, horizontal, vertical) which was used as an external trigger system. The spill triggers are caused from the incoming particles. The combination of front and back represent all the particles going through the detector and exiting it. Combination of present and front represent all particles entering FoCal while present and back the beam related particles exiting it. Finally, the present-horizontal-vertical triggers show the particles entering FoCal in its central part. The last combination of scintillators that produces the so called central trigger was used in the analysis in order to be quite sure that the particles enter the prototype more or less in its center. The active area of both horizontal and vertical scintillators is 10mm width x 30 mm length. Thus, when we place one in front of the other vertically, the active area of the coincidence of the two becomes 10 mm x 10 mm in the x-y plane.

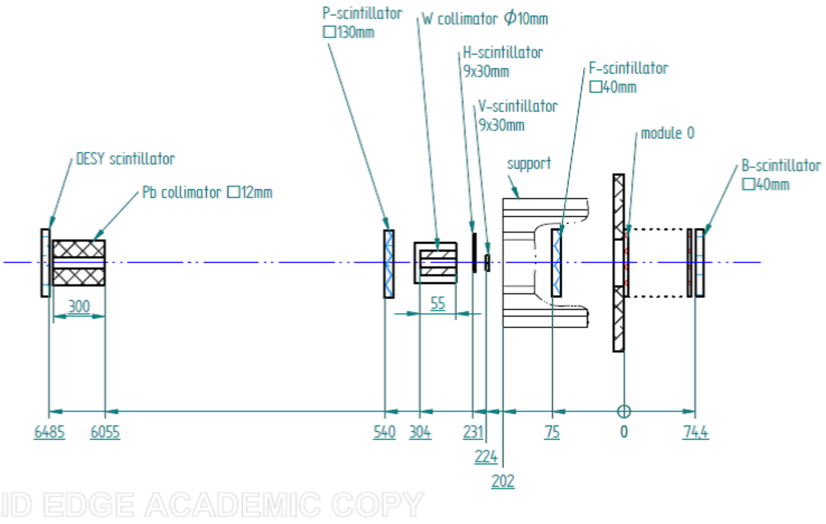

Figure 2.6: The DESY beam test set up. Distances are in mm.[12]

2.3.1 Trigger system and scintillators

The purpose of this part was to run some tests for the front and back scintillators that we were going to use in our FoCal prototype beam test to investigate their behaviour and get familiar with the equipment that is generally used when someone is using scintillators. Both were square scintillators with a surface of 16 cm^2 and a thickness of 1 cm. Scintillators can be of several types such as organic crystals, organic liquids, plastic scintillators, inorganic crystals, glasses. The type of scintillator that we used was plastic. The scintillator, which is coupled with a photomultiplier absorbs some energy of the incoming particle and re- emits it in the form of light. Then, the photomultiplier absorbs the light emitted by the scintillator and converts it in the form of electrons via the photoelectric effect. These electrons result in an electrical pulse. A photomultiplier is a member of vacuum phototubes, which are extremely sensitive detectors of light. They multiply the current produced by incident light by as much as 100 million times, enabling for example individual photons to be detected when the incident flux of light is very low. In general, the first test conducted for a scintillator is to look at the signal it produces using the oscilloscope. By looking at the signal and the height of the pulses at the oscilloscope we can define the threshold of the pulses so that we have the less possible noise in our measurements. By choosing the threshold level, with the use of several electronic units (see Appendix A) it is possible to find the ideal working plateau (optimal voltage) for the scintillators (figures 2.7, 2.8). The plateau represents a region in which the counting rate is the least sensitive to changes and ensures a minimum of counting variations.

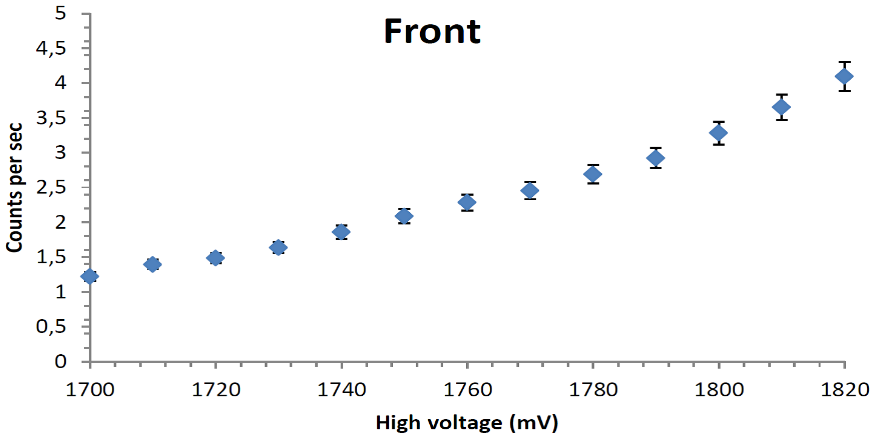

Figure 2.7: Counts rate for the front scintillator.

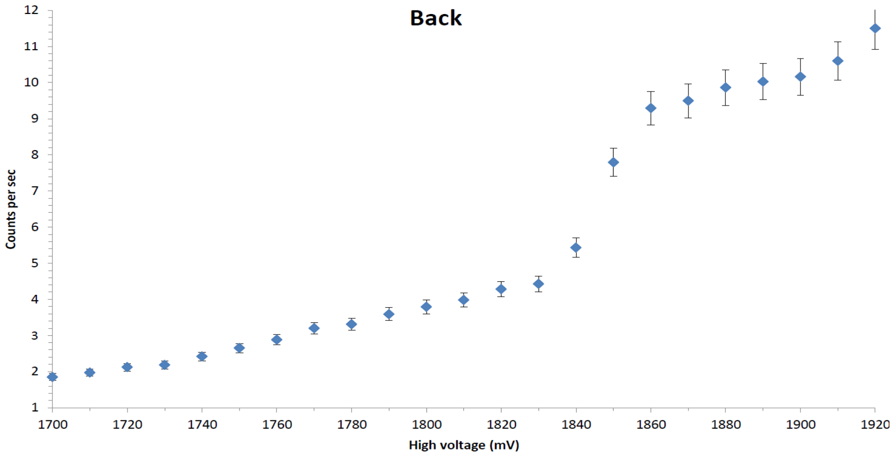

Figure 2.8: Counts rate for the back scintillator.

In addition, we measured the coincidence counts for our scintillators and we calculated the accidental coincidence counts in order to see if our measurements were affected (figures 2.9, 2.10). In order to count the coincidence counts we placed the two scintillators one above the other with their active areas overlapping. The particles detected by the scintillators for the tests were cosmic radiation, i.e. muons. The working plateaus for the front scintillator was 1770V and for the back scintillator was 1790V. For these values the coincidence counts measured were almost 10 per minute while the accidental coincidence counts were very low and thus, they dont affect our measurements (see Appendix A, table A.1). The threshold for the discriminator was set at -30 mV.
Accidental coincidence counts were calculated from

$$N_{A.C} = \Delta\tau \times f_f \times f_b \tag{2.5}$$

where $\Delta\tau$ is the width of the signal (coincidence time window) and f_f ,f_b are the pulse frequencies of the front and back scintillator respectively. The numerical results are shown in Appendix A, table A.1.

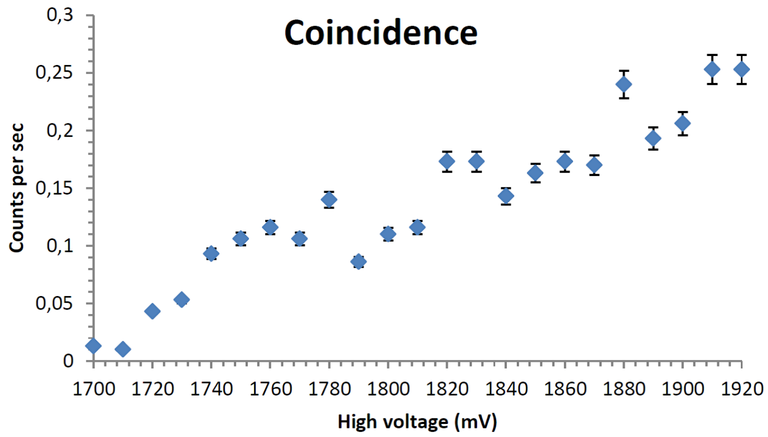

Figure 2.9: Coincidence counts per sec for both scintillators working at the same voltage.

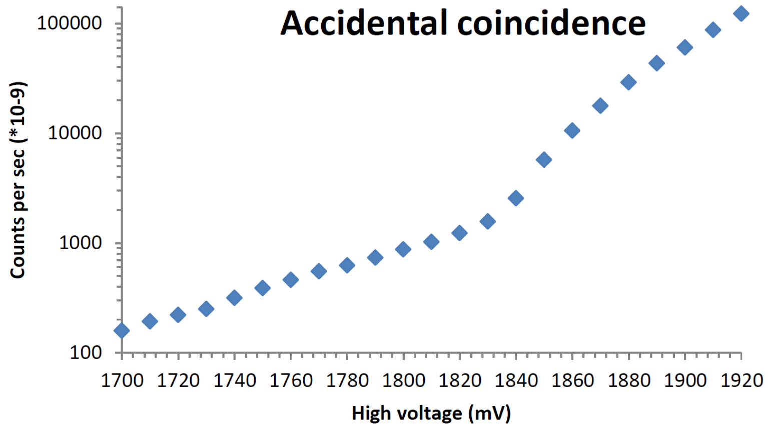

Figure 2.10: Accidental coincidence counts per sec for both scintillators working at the same voltage.

We also tested the behaviour of the counts by increasing the threshold by a step of 10 mV and we expected the counts to decrease. Indeed what we saw is the counts being less each time we increased the threshold.

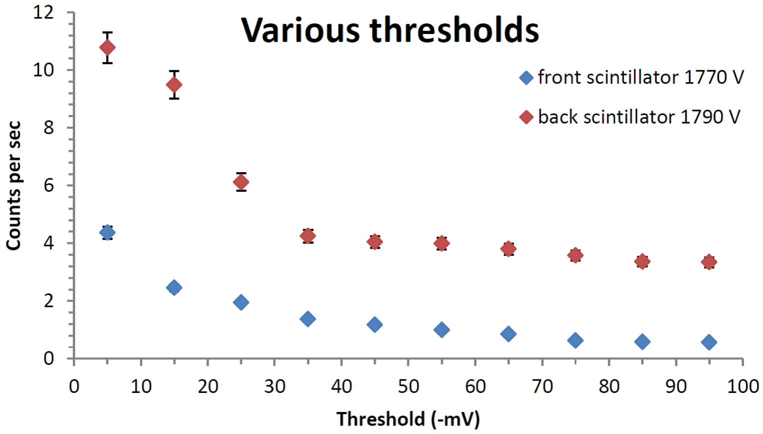

Figure 2.11: Counts per sec for the various thresholds.

2.3.2 Trigger data from beam test

In this section we present the trigger data obtained from the beam test at DESY. The trigger system that we used had five triggers as we saw in figure 2.6. This quick study of the number of triggers was done to check if both Virtex6 boxes count the same numbers or if there were problems in counting and in the synchronization of the triggers/signals. Three runs were analysed, however herein we only present the results from the run 114 (for more see Appendix A, table A.2).

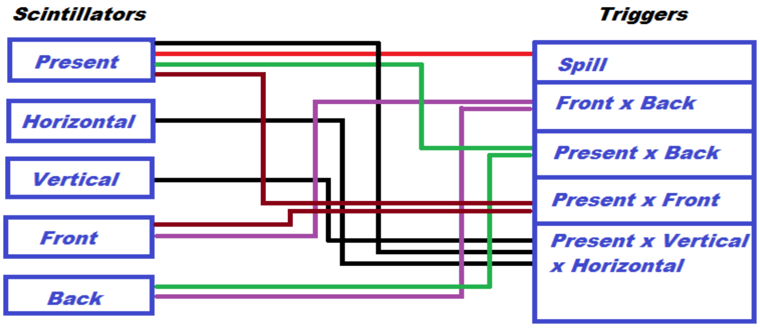

Figure 2.12: Schematic of the scintillators combinations to obtain the triggers.

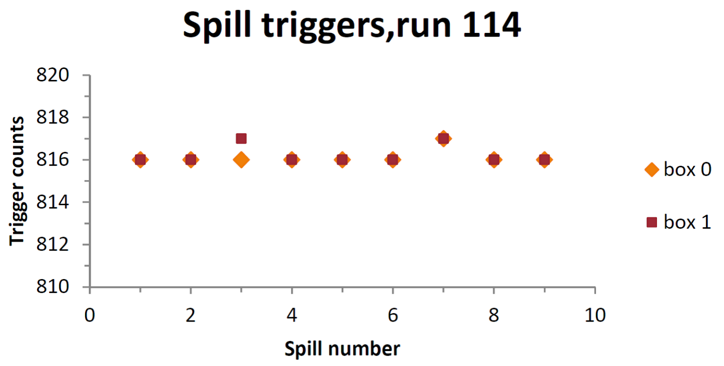

Figure 2.13: Spill trigger counts for the two Virtex boxes.

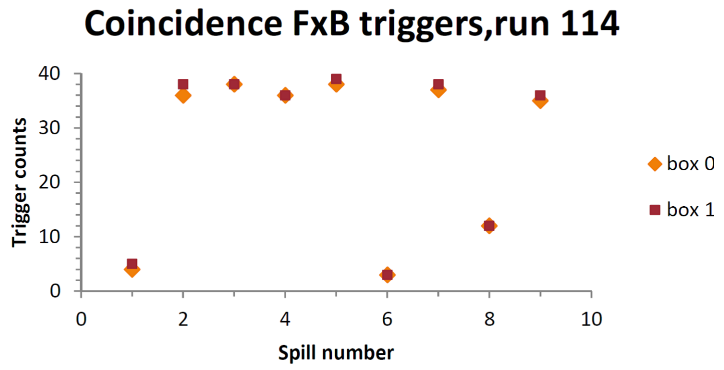

Figure 2.14: Coincidence FxB trigger counts for the two Virtex boxes.

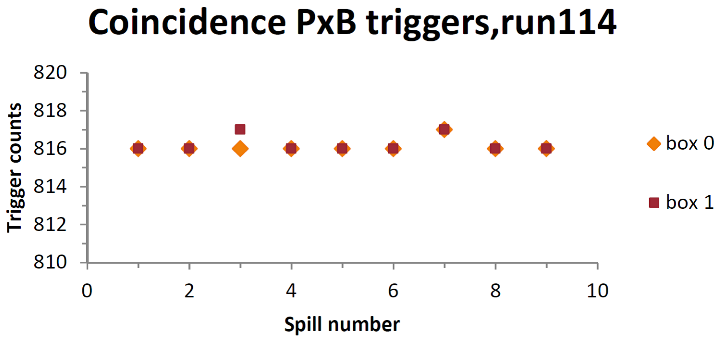

Figure 2.15: Coincidence PxB trigger counts for the two Virtex boxes.

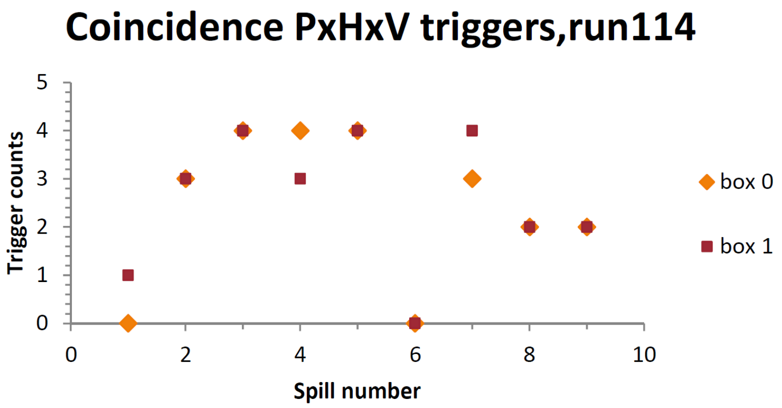

Figure 2.16: Coincidence PxHxV trigger counts for the two Virtex boxes.

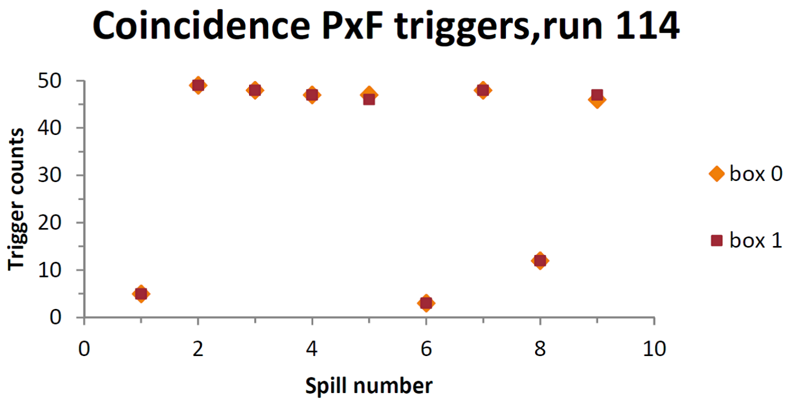

Figure 2.17: Coincidence PxF trigger counts for the two Virtex boxes.

As it can be seen from figures 2.13-2.17, there were some problems in the trigger counting. Therefore it can be concluded, that the two Virtex boxes did not measure the same number of triggers either due to problems with the two boxes (counting procedure) or with the synchronization between them[1]. Nevertheless, the differences are quite small, so this could not be considered as a major problem of the function of the Virtex6 boxes.

---

[1] Later on, the electronic problems causing the two Virtex6 boxes to count different number of trigger bits were fixed for later beam tests at PS and SPS, CERN.

2.3.3 MIMOSA23 chip testing

In this part, the results from a test that was done to check the orientation of the MIMOSA23 chips in the set up is presented. To conduct this test a LED was used as a source of light. The following procedure was followed: Inside a big metallic box we placed the 4 chips of a layer on a frame (see figure 2.18 right). We also placed the LED in a different frame that could be electrically and very precisely moved both horizontally and vertically. Then by moving the LED up, down right and left we radiated the 4 chips. In this way we can observe in figures 2.19-2.23 in which direction the spot of the LED is moving in each of the four chips. For the LED we consider the +y to be in the up direction, the +x in the right direction and the (x=0, y=0) point to be in the center of the chips in x direction and in the middle of the distance between chips 0 and 1 which is 10 mm. Chips 0 and 3 as well as chips 1 and 2 were adjoined. The coordinates of the LED are in mm.

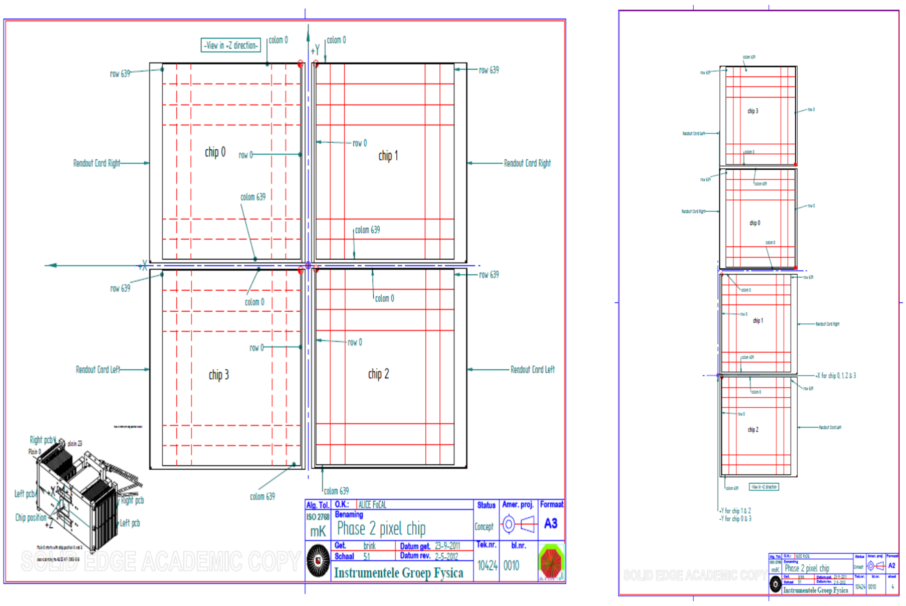

Figure 2.18: Left: 4 chips set up in a layer in the prototype Right: 4 chips testing set up.[12]

We changed the y and x several times so that we could cover all four chips to study their individual orientation. First we checked the chips without the LED. What we expect to see is that there are no hits in all four chips. The result (figure 2.18) confirms our expectation. In the following plots chip 0 has coordinates 0 ≤ y ≤ 2 cm and 0 ≤ x ≤ 2 cm, chip 1 has 0 ≤ y ≤ 2 cm and 0 ≥ x ≥ -2 cm, chip 2 has 0 ≥ y ≥ -2 cm and 0 ≥ x ≥ -2 cm, chip 3 has 0 ≥ y ≥ -2 cm and 0 ≤ x ≤ 2 cm.

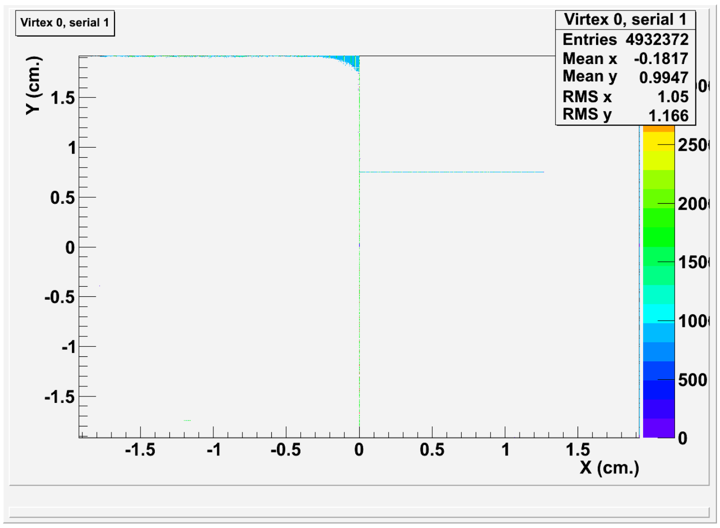

Figure 2.19: 4 chips with no LED. No hits in the plot are observed. The lines in light blue and the light blue area is most likely caused due of the defective chip.

Next, we moved the LED to (0, 10), (0,15) and (0, 20) points. We observe that the hits in the plots move in the opposite way. This implies that chip 0 has reverse y direction. Moving the LED to the right to (0,10) and (5,10) for chip 0 we see that hits follow the same direction.

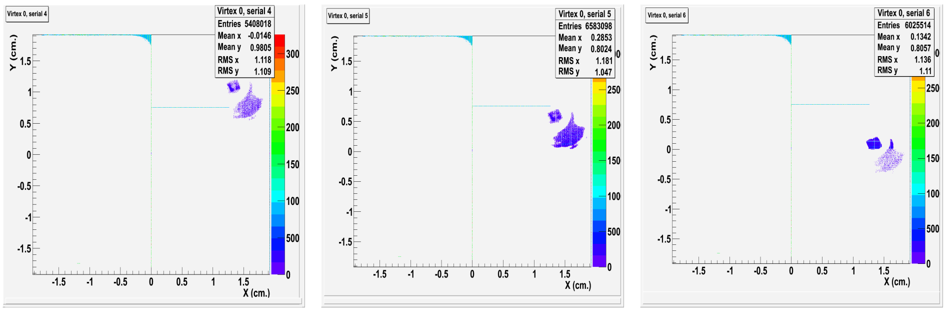

Figure 2.20: Chip 0: moving LED up leads the hits to move down (reversed y direction).

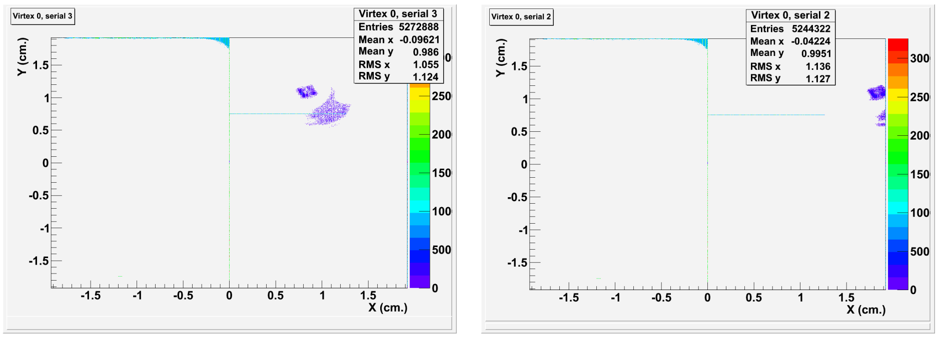

Figure 2.21: Chip 0: moving LED to the right leads the hits to move also to the right (not reversed x direction).

We followed the same steps for chips 1, 2 and 3. What we see is that chip 1 and 2 has both x and y direction not reversed and chip 3 has the y direction reversed while its x direction is not. Here, only the plots for chip 3 are presented as a proof of the statement about its y direction.

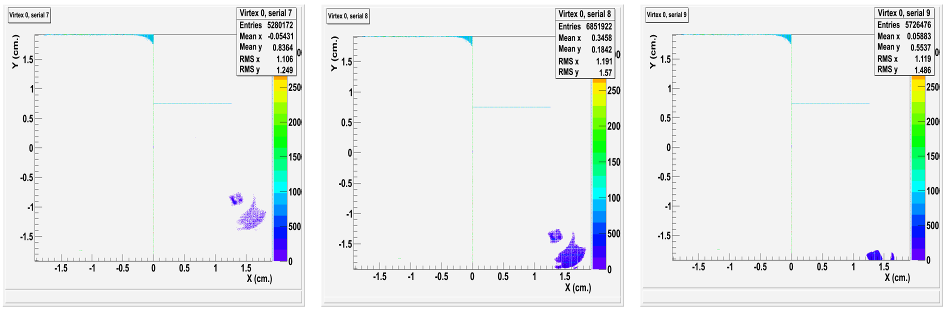

Figure 2.22: Chip 3: from left to right (0,30), (0,35), (0,40). The LED pattern in the chip is going to lower y values (reversed y direction).

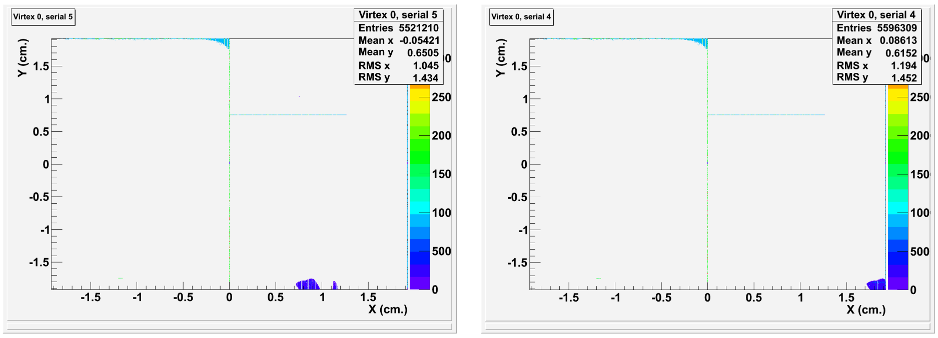

Figure 2.23: Chip 3: from left to right (0,40), (5,40). The LED pattern in the chip is going to higher x values (not reversed x direction).

The results obtained are very useful since in this way we can define the orientation of the chips connected in a layer in the prototype. Looking at figure 2.18(left) we see that all four chips have the same +x and +y. This happens due to the fact that chips 0 and 3 are placed reversed in the layer (see figure 2.24). In this way we decide the final coordinate system for the detector (see also [13]).

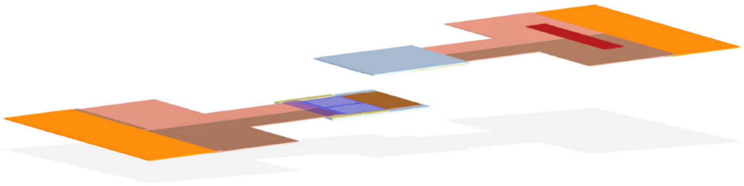

Figure 2.24: Left part is chips 1 and 2 while the reversed right part is chips 0 and 3.[12]

Chapter 3

Data analysis results

In this chapter, the longitudinal and lateral profiles of the data taken from the FoCal prototype in the DESY beam test are presented. Beams consisting of pure electrons with energies at 2 and 5 GeV were used. The 2 GeV beam is considered to be the lowest energy limit for the FoCal calorimeter. FOCAL behaviour investigation and study of both longitudinal and lateral profiles are the major parts of this analysis. Moreover analysis made in order to test the trigger system and the prototype's alignment is also shown. In the first part we deal only with the 5 GeV data but later in the main analysis we also include the 2 GeV data.

Since the beam test at DESY was the first for the Utrecht group FoCal prototype we faced several problems. Nevertheless, the data obtained were sufficient for the kind of analysis we wanted to have. However, since test at DESY was the first for the prototype, it is considered quite important as it was used as a "reference" for the future tests made, in order to avoid the same mistakes and omissions. Since one major problem was the malfunction of the chips, it is important to mention the chips that didn't work or were totally disconnected before starting with the analysis (table 3.1). In total 35 out of 96 chips are either broken or disconnected (more than the 1/3 of the chips used in the whole calorimeter).

Table 3.1: Full list of broken or disconnected chips at the beam test at DESY. Quadrant number according to ALICE coordinate system. X and Y are the coordinates direction.

ChipNumber	Layer	Quadrant	x	y
25	1	3	+	-
95	3	1	-	+
54	6	2	-	-
90	7	2	-	-
8	8	0	+	+
11	8	1	-	+
10	8	2	-	-
9	8	3	+	-
59	10	1	-	+
13	12	3	+	-
35	13	1	-	+
60	14	0	+	+
19	16	1	-	+
31	17	1	-	+
65	18	3	+	-
76	19	0	+	+
79	19	1	-	+
78	19	2	-	-
77	19	3	+	-
0	20	0	+	+
3	20	1	-	+
2	20	2	-	-
1	20	3	+	-
44	21	0	+	+
47	21	1	-	+
46	21	2	-	-
45	21	3	+	-
68	22	0	+	+
71	22	1	-	+
70	22	2	-	-
69	22	3	+	-
72	23	0	+	+
75	23	1	-	+
74	23	2	-	-
73	23	3	+	-

3.1 Raw data at 2 and 5 GeV

In this section a first look in the raw data takes place. Looking at the raw data gives a brief idea about the prototype's behaviour. Moreover, the longitudinal profiles are also presented, of which later the energy resolution calculation and prototype's calibration will take place. To select a subset of the data the central trigger condition is imposed, which reassures that the beam enters the prototype in it's center (see section 2.3).

3.1.1 Hit distribution

The analysis begins by showing the hit distribution for different layers in the x,y plane, which is the plane vertical to the beam since beam is parallel to the z axis of the detector. The beam is coming towards the page and the plots are vertical to the direction of the beam. (figures 3.1-3.3).

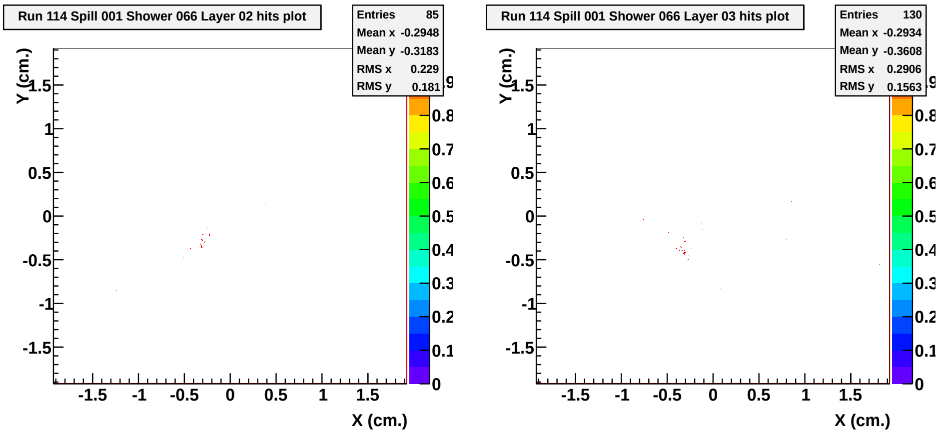

Figure 3.1: From left to right: Hit distribution plots for 5 GeV, run 114, spill 001, shower 066, layer 2 and 3.

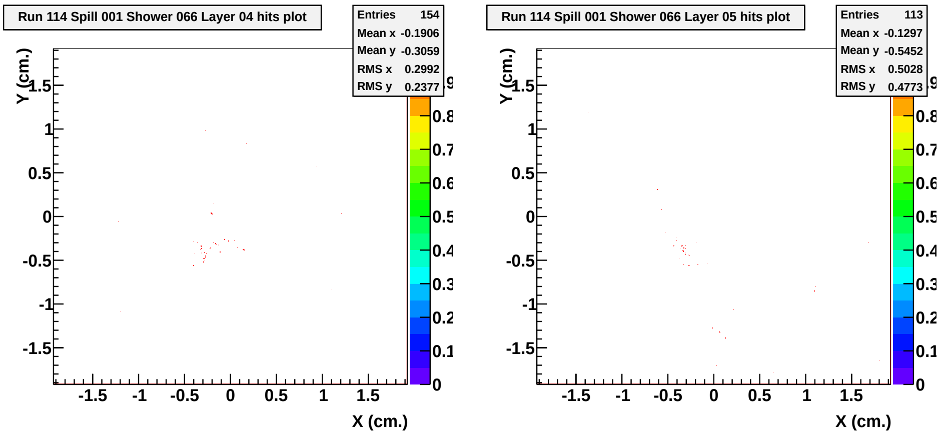

Figure 3.2: From left to right: Hit distribution plots for 5 GeV, run 114, spill 001, shower 066, layer 4 and 5.

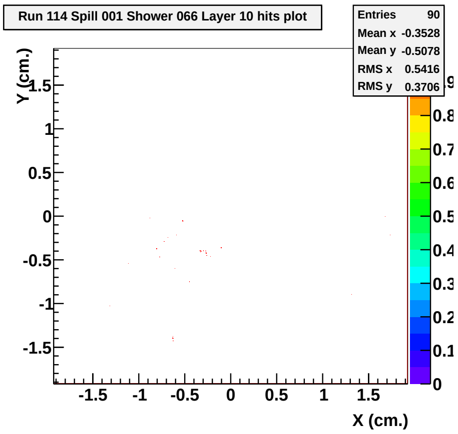

Figure 3.3: Hit distribution plots for 5 GeV, run 114, spill 001, shower 066, layer 10.

From the figures above, one can notice that the number of hits in the first layers is increasing until we reach layer 5 and then this number starts to decrease. The shower maximum is at layer 5 (almost 5 radiation lengths) according to equation 1.11. The same holds for several showers at 5 GeV.

3.1.2 Fluctuations per layer

In this section we present the fluctuations in the number of hits for different layers for whole spills. The plots have the number of hits in the horizontal axis and the number of their occurrences in the vertical axis. What we observe from the figures 3.4-3.6 is that for different spill number the same layer has a different number of hits. This verifies the theory about the sampling fluctuations per layer due to the absorber (see section 1.4). The statistics are really low and thus we cannot draw solid conclusions about the layers behaviour. For all the layers histograms for different spills at 5 GeV see Appendix B. (figures B.1-B.3)

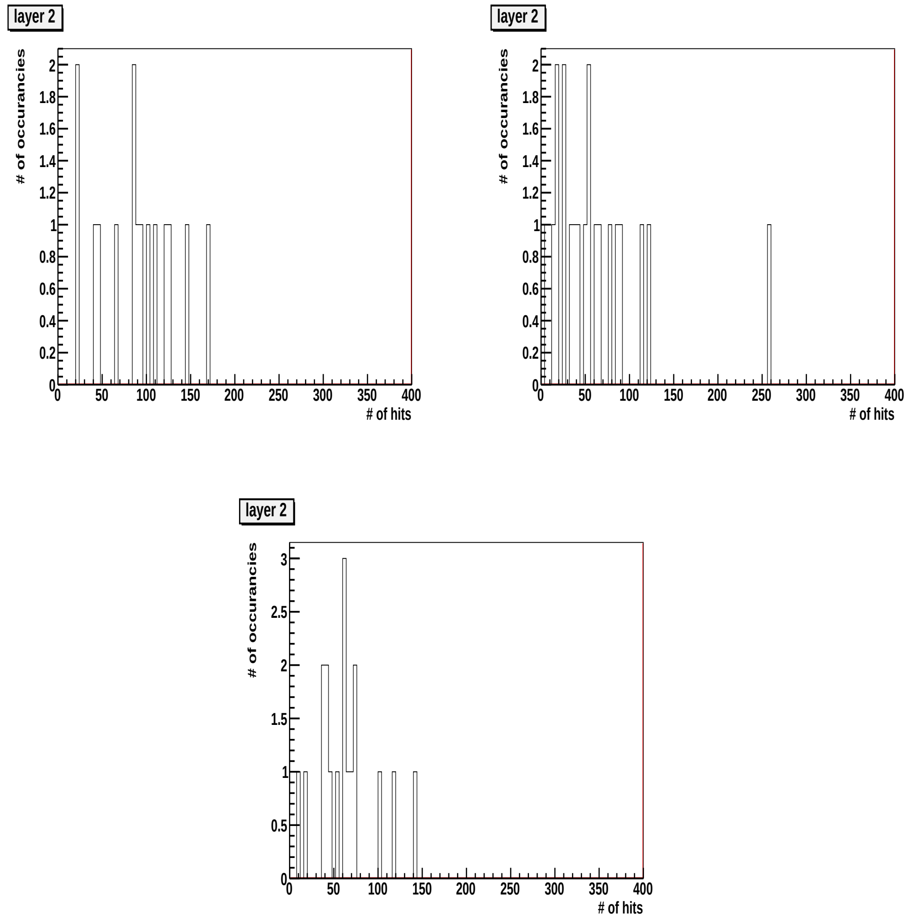

Figure 3.4: From left to right: Layer 2 hit fluctuations histogram for 5 GeV, run 114, spill 001 to spill 003.

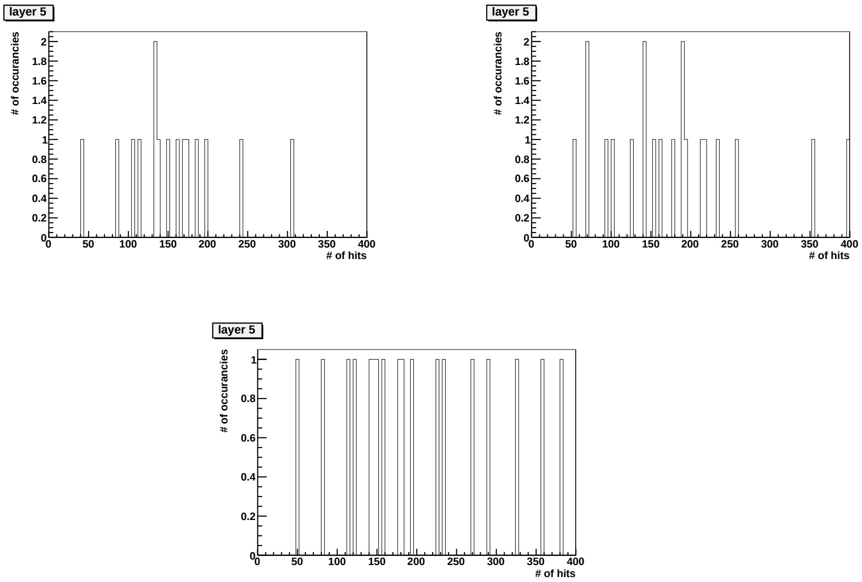

Figure 3.5: Layer 5 hit fluctuations histogram for 5 GeV, run 114, spill 001 to spill 003.

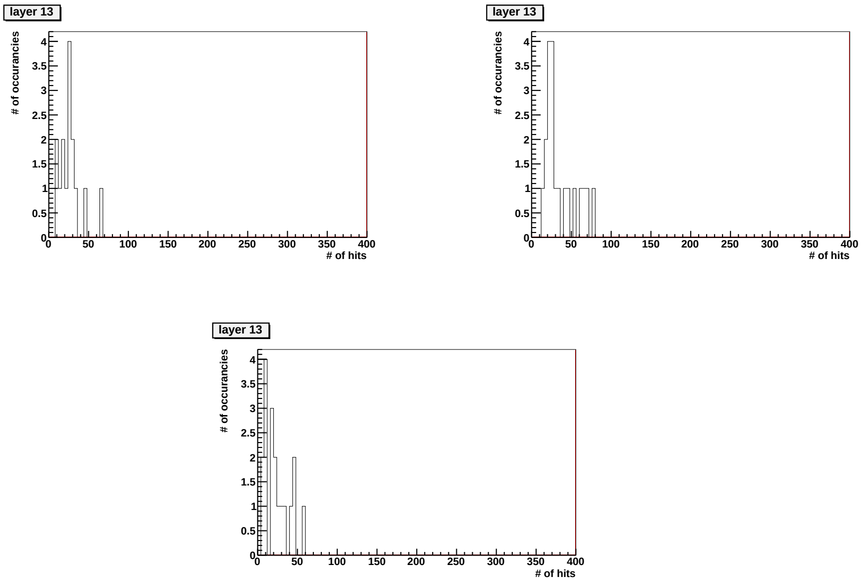

Figure 3.6: Layer 13 hit fluctuations histogram for 5 GeV, run 114, spill 001 to spill 003.

Since the statistics for figures 3.4-3.6 were very low, we decided to draw the same plots for runs 114-116 at 5 GeV which have in total 752 showers. In the following plots we present the hit histograms for several layers. We observe again that the mean value (average number of hits per layer) increases until we reach layer 5 and then the number of starts to decrease. The wide distribution (peak) show again the fluctuations observed from shower to shower.

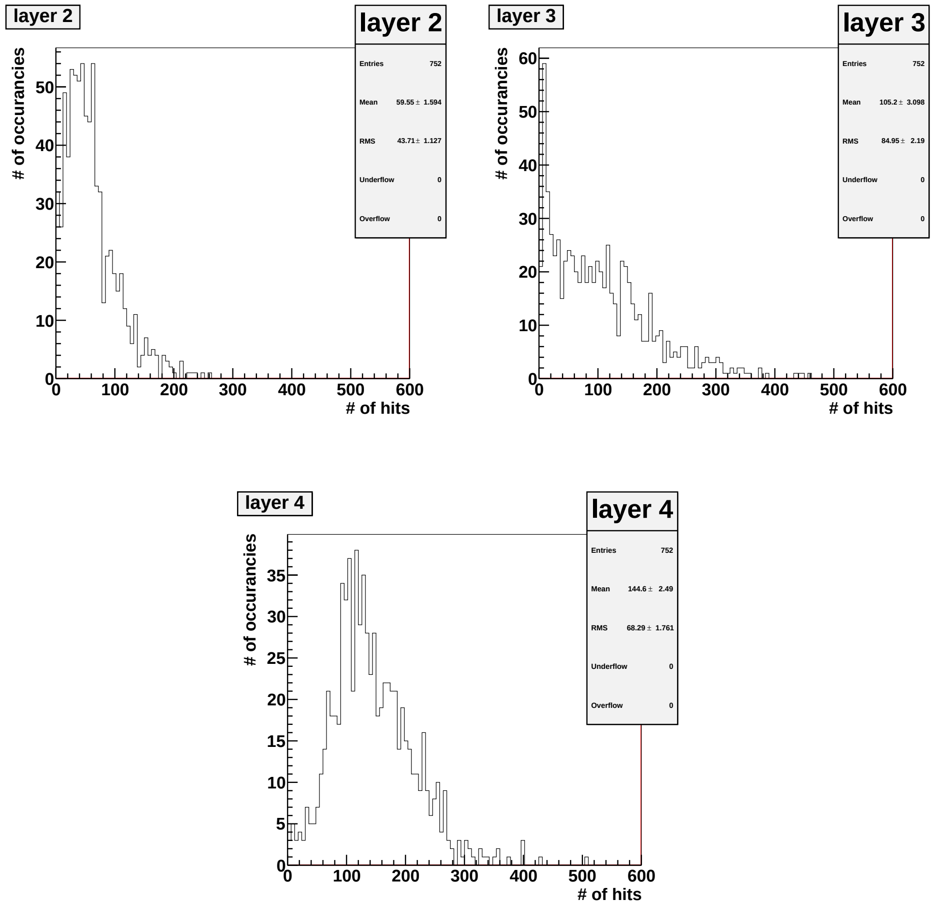

Figure 3.7: Layers 2-4 hit histograms for 5 GeV, runs 114-116. Notice that the mean value (average number of hits per layer) increases.

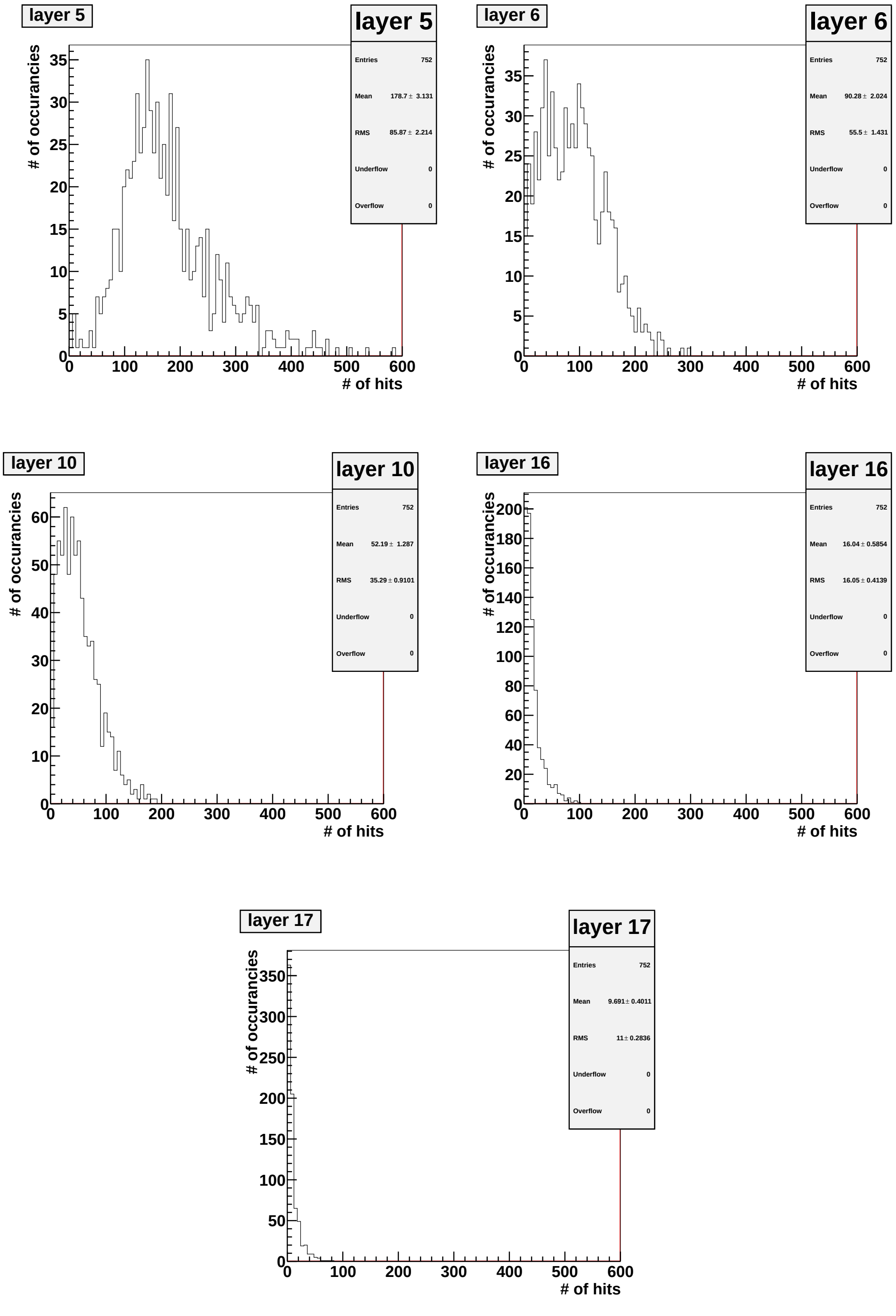

Figure 3.8: First two plots: Layers 5 and 6 hit histograms for 5 GeV, runs 114-116. Last three plots: Layer 10,11,16 profile plots for 5 GeV, runs 114-116. After layer 5 the number of hits decreases since at layer 5 the shower maximum is located.

Next, for the same plots we applied the extra condition about the trigger, the "pile-up" condition (see section 2.2) in order to see if the scenario of two triggers in less than 640 μ sec holds for our data. Plots from layers 2-4 are only shown. What it can be seen is that we don't have any change in the values of the data, thus the "pile-up" phenomenon doesn't hold for our case.

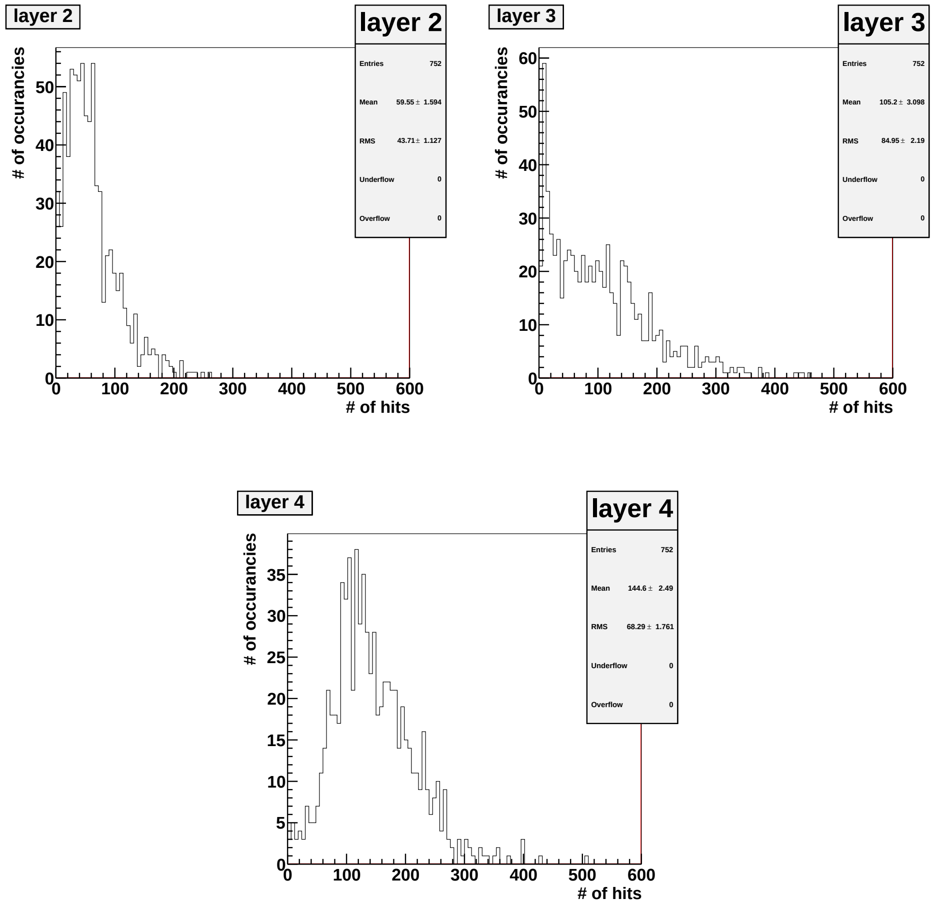

Figure 3.9: Layers 2-4 hit histograms for 5 GeV, runs 114-116 with the extra trigger condition. Notice that the plots are exactly the same with those in figure 3.7.

3.1.3 Calorimeter longitudinal hit profile

In this section, the average number of hits per layer for the whole detector is presented for runs 114-116. We add a gamma function curve to check if our data agree with the simulations as mentioned in section 1.3. The parameters (scale, shape and position) for the gamma distribution have been calculated by simulations.

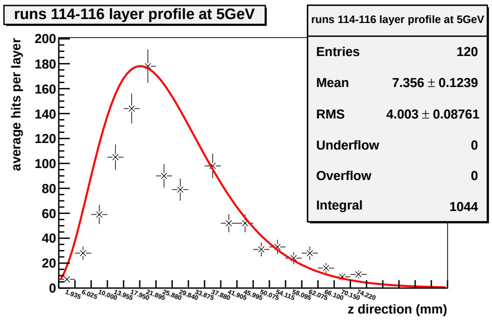

Figure 3.10: Longitudinal profile for runs 114-116 at 5 GeV with a gamma function.

As it can be seen from figure 3.10 almost all layers show a deviation from the simulations. Partially this can be explained form the fact that we had broken chips in some layers (chip numbers 19,59,65,90,95) but also shows that a readjustment of the chips settings should be done. From figure 3.11 we calculate the calibration factors as follows

$$C_{\mathrm{c,l}} = \frac{\text{Simulated number of hits}}{\text{Measured number of hits}} \tag{3.1}$$

where c and l hold for chip and layer respectively.

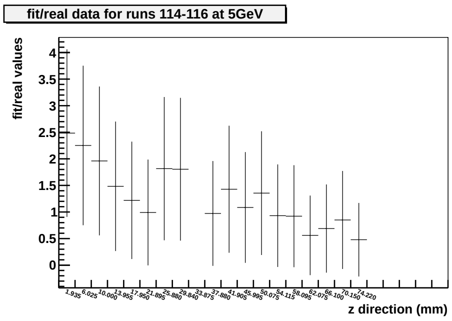

Figure 3.11: Ratio of the theoretical average hits per layer from the gamma distribution over the real average hits, for runs 114-116 at 5 GeV.

3.2 Energy resolution and calibration

In this section, the analysis of the longitudinal profiles of the calorimeter for 2 and 5 GeV is studied more in detail as well as the energy resolution. For the 5 GeV we studied the runs 114-116 (114-119 after section 3.2.1) while for the 2 GeV runs 93-98. From simulations and theory the energy resolution for the FoCal calorimeter is expected to be 9% for 5 GeV and 14% for 2 GeV respectively. For the calibration of the prototype several methods are used. For each one, the procedure followed will be analysed together with the results. The pile-up rejection condition is applied while the central trigger condition is not.

3.2.1 Raw data with chip hits correction, layer interpolation and multiplication factors

The procedure followed in this analysis is:

- The longitudinal profiles from all the runs were plotted along with the theoretical gamma distribution in which we only set the height, so that for 5 GeV the maximum is at layer 5 while for 2 GeV at layer 4.
- From the previous plot we calculated the C_l for each layer.
- We applied the C_l to check the changes on our profiles and whether the data matched the gamma curve or not (figure 3.12).
- We drew a histogram with the total number of hits for each shower before and after applying any C_l to our data. So we drew the raw data before after applying the factors. From this plot we calculated the energy resolution of the detector by dividing the RMS of the histogram over the mean value, i.e the $\frac{\sigma(E)}{E}$ as shown in eq. 1.15-1.16.
- The previous step was repeated but this time we corrected the broken chips (chip # 19,59,65,90,95 are considered not to work up to this point, this changes in the next steps of analysis) by adding "fake" hits. We plotted the same histograms before and after applying the C_l.
- Since layers 8, 19, 20, 21, 22, 23 are totally disconnected (see table 3.1) we considered our detector to have a length up to 18th layer. Nevertheless layer 8 was still considered to be part of our detector. This is why we tried to add in layer 8 "fake" hits that should be there if the complete layer was working. The way we did this, was by adding in layer 8 the mean of the hits in layer 7 and layer 9. Finally, we calculated the energy resolution with the "fake" layer 8 once again before and after applying the C_l.

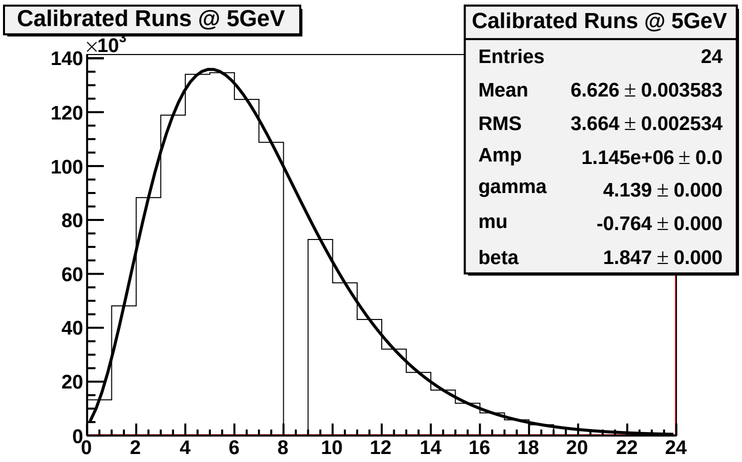

Figure 3.12: Longitudinal profile with the gamma distribution after correction with factors from figure 3.11

From figure 3.10 one can notice that there are very few layers that agree with the theoretical expected values. Most of the layers have a factor larger than 1, which means that the layer and the chips consisting it are not very sensitive or have a high signal threshold level. On the other hand, there are 4-5 layers mostly in the tail of the detector that show high sensitivity (or they have low signal threshold level) and factors below 1. The energy resolution is calculated from the following plots in figure 3.13.

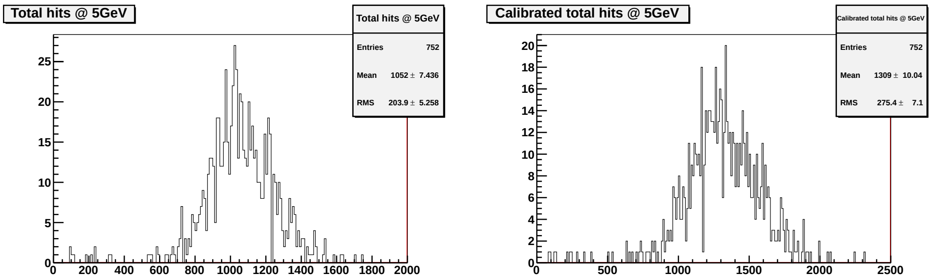

Figure 3.13: Runs 114-116 at 5 GeV. Hits per shower histograms. Left: Energy resolution for raw data 19.3%. Right: Energy resolution for raw data after calibration factors is 21%.

From figure 3.13 it can be seen that by applying the C_1 in the raw data the energy resolution gets worse, in particular from 19.3% goes to 21%.

The same plots after applying the broken chip hits correction are shown. The chip hits correction method is an arbitrary method in which we add by hand hits in chips that we knew to be broken. What we did was to count the number of hits in the layer and try to calculate the number of hits "missing" due to the broken chip by looking at the total number of hits in the layer, as well as in the previous and the next one. The formula we used was

$$N_{hits} = \frac{1}{4}\frac{N^{hits}_{previouslayer} - N^{hits}_{nextlayer}}{2} \tag{3.2}$$

where N_{hits} is the number of hits we add in the broken chip, $N^{hits}_{nextlayer}$ $N^{hits}_{previouslayer}$ is the total number of hits in the next and previous layer of the one that the broken chip is, respectively. We calculate the energy resolution for both cases without and with the C_1 .(see figure 3.14)

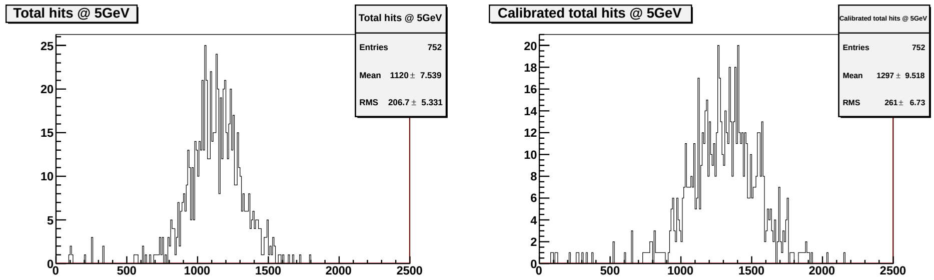

Figure 3.14: Runs 114-116 at 5 GeV. Hits per shower histograms. Calculation of energy resolution for raw data with the broken chip hits correction. Left: Energy resolution before calibration factors is 18.4%. Right: Energy resolution after calibration factors is 20.1%.

The next step is the same as the one followed for figure 3.14 but this time we added "fake" hits in a whole layer that it is broken, i.e layer 8 (since we have mentioned that we consider our calorimeter to be of 18 layers). Again calculation before and after the C_1 takes place.(figure 3.15)

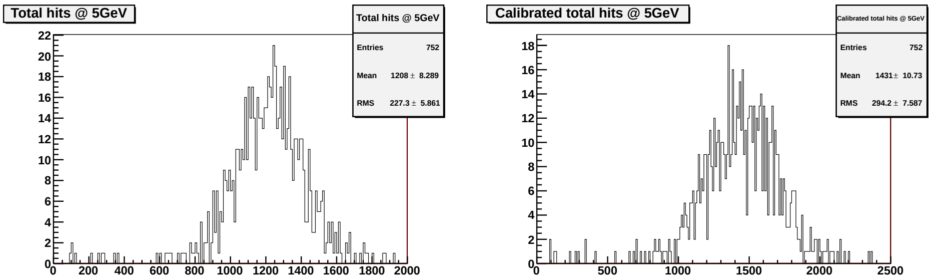

Figure 3.15: Runs 114-116 at 5 GeV. Hits per shower histograms. Calculation of energy resolution for raw data with the broken chip hit correction and layer 8 correction. Left: Energy resolution before calibration factors is 18.8%. Right: Energy resolution after calibration factors is 20.5%.

We followed the same exact procedure for the 2 GeV data.

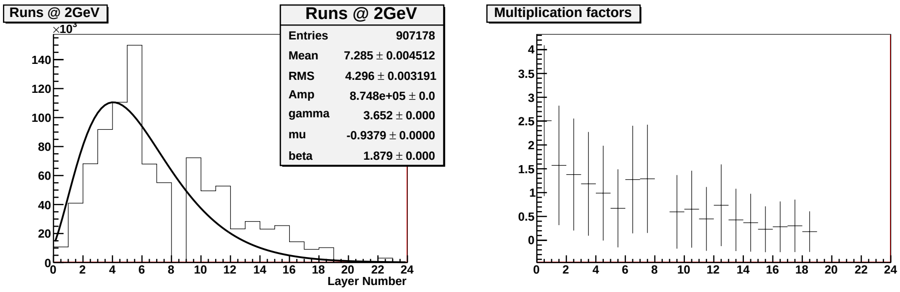

Figure 3.16: Runs 93-98 at 2 GeV. Left: Longitudinal hits profile along with the theoretical gamma distribution. Right: Calibration factors for each layer.

From figure 3.16 it can be seen that similar to the 5 GeV data, only a few layers agree with the theoretical expected values. The major difference from the corresponding plot for 5 GeV is that now most of layers show high sensitivity (i.e factors below 1) and probably need to be adjusted in a higher threshold level.

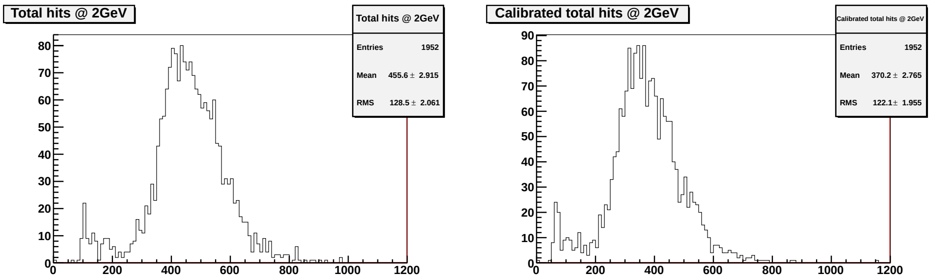

Figure 3.17: Runs 93-98 at 2 GeV. Hits per shower histograms. Calculation of energy resolution for raw data. Left: Energy resolution before calibration factors is 28.2%. Right: Energy resolution after calibration factors is 33%.

From figure 3.17 it can be seen that by applying the calibration factors in the "raw" data the energy resolution gets worse, in particular from 28.2% goes to 33.1%. Next we show the same plots but after applying the broken chip hits correction.

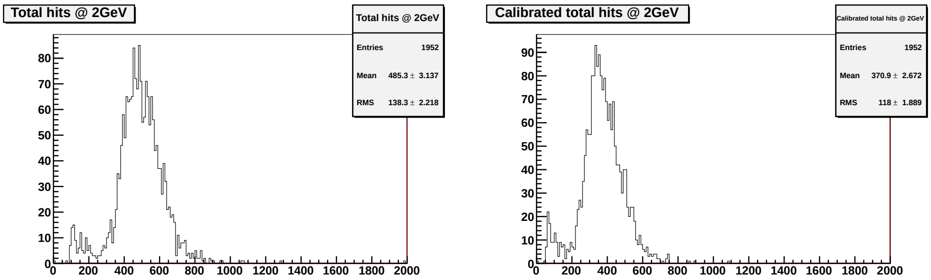

Figure 3.18: Runs 93-98 at 2 GeV. Hits per shower histograms. Calculation of energy resolution for raw data with the broken chip hit correction. Left: Energy resolution before calibration factors is 28.2%. Right: Energy resolution after calibration factors is 31.8%.

For the "raw" data plot without the calibration factors the energy resolution remains the same, however after the correction factors we observe an improvement of 1.2%. Nevertheless, one can still notice that the calibration factors didn't improve our results but on the contrary they deteriorate them. Finally the same method as in figure 3.18 is followed by adding the condition for the broken layer 8 "fake" hits.

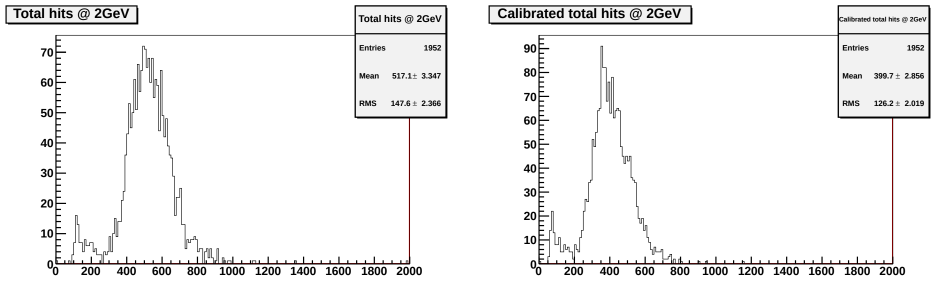

Figure 3.19: Runs 93-98 at 2 GeV. Hits per shower histograms. Calculation of energy resolution for raw data with the broken chip hit correction and layer 8 correction. Left: Energy resolution before calibration factors is 28.3%. Right: Energy resolution after calibration factors is 31.5%.

To summarize the results until now, what can be concluded is that the method that improves our results is using the raw data and applying the chip hits correction. The best results for the energy resolution is for 5 GeV the 18.4% and for 2 GeV the 28.2%. However, comparing these results with the raw data results, we see that the improvement is infinitesimal (for 5 GeV only, for 2 GeV is non-existent). For both energies we are a factor of two up compared to the "expected/wanted" results of 9% and 14% for 5 and 2 GeV respectively. It should be mentioned that we also tried to apply the calibration factors calculated from the 5 GeV data to the 2 GeV data and vice versa but it also didn't improve our results.

3.2.2 Corrected data, i.e. raw data without chip noise

Therefore, we further continued by changing our way of analysis to a different approach, by looking more into depth in the chip level. From the data taken by the runs from the 2 and 5 GeV we now removed the pedestal and the chip noise. We have set the maximum chip noise to be of the order of 10^{-5} times the number of pixels in each chip, i.e. almost 4 hits per chip. This chip noise is called thermal noise. In this analysis if there was a chip found which after the pedestal and chip noise subtraction appeared to have negative number of hits, then zero number of hits were considered instead of negative. The results for the energy resolution from this concept are shown in figure 3.20. For this analysis we used runs 93-98 for the 2 GeV and runs 114-119 for the 5 GeV. We also kept the pile-up condition and applied the central trigger condition. The calculation of the energy resolution is made by a Gaussian fit when it is possible.

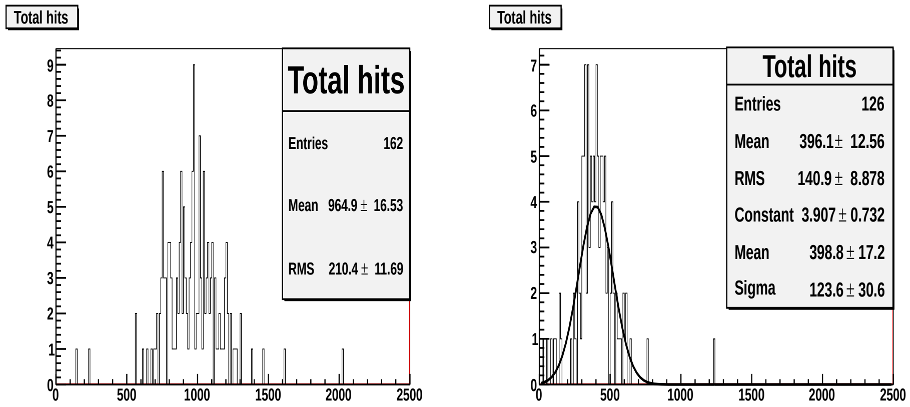

Figure 3.20: Hits per shower plots. Noise is removed from the chips. Left: Runs 114-119 at 5 GeV. Energy resolution calculated to be 21.7%. Right: Runs 93-98 at 2 GeV. Energy resolution calculated from Gaussian fit to be 30.9%.

3.2.3 Corrected data, separation in four quadrants, chip interpolation and calibration factors

The detector was separated in four quadrants (like the way we see in figure 2.17). In each quadrant, there are now 24 chips. In each chip the noise was removed, and if the number of hits was smaller than the noise for a frame, then for this frame and chip the number of hits were considered to be equal to zero. For each quadrant, we used the same gamma fit from the simulation and considered as maximum height of the fit the maximum of all four quadrants. The C_c for the working chips were calculated according to eq. 3.1 and then these factors were applied for every frame from the beginning. The last step was to interpolate the dead chips in the same way we did for the dead layer, i.e by taking the average number of hits from the previous and the next chip. The results from this method are shown in figures 3.21-3.23.

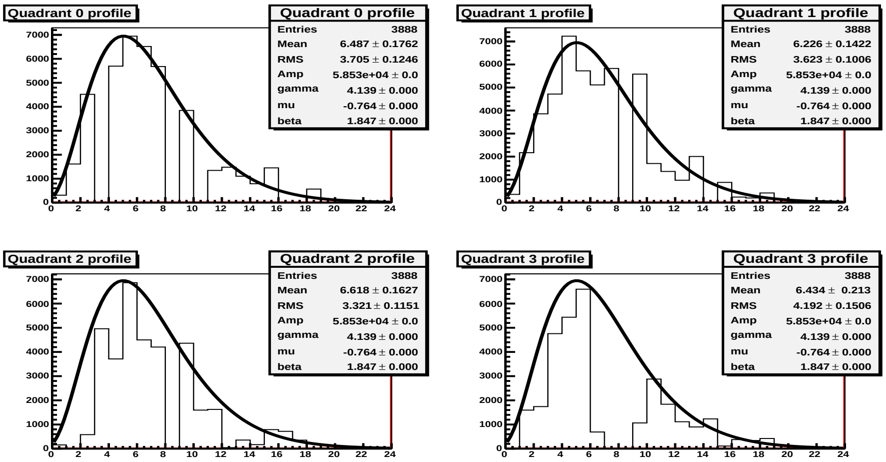

Figure 3.21: Runs 114-119 at 5 GeV. Quadrants hit profile with gamma fit. All quadrants have the same gamma fit taken from upper left plot since it has the most high value among all four. Notice: Upper left is quadrant 1 in ALICE system, upper right is quadrant 0, down left is quadrant 3 and down right is quadrant 2.

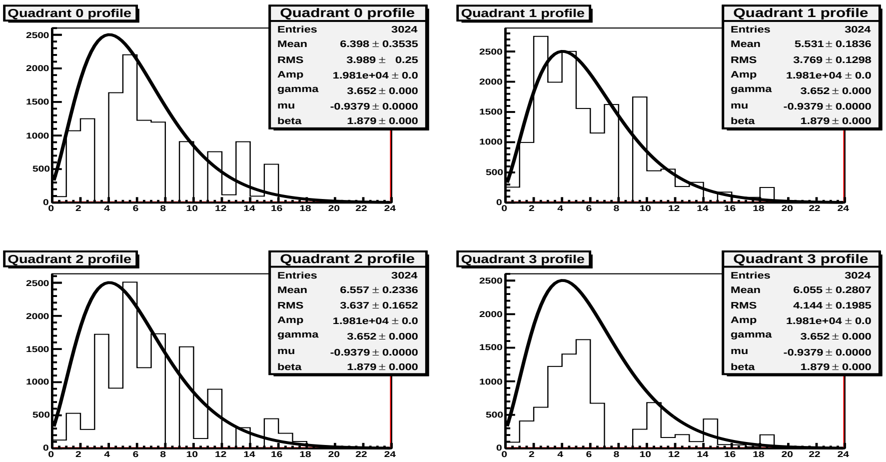

Figure 3.22: Runs 93-98 at 2 GeV. Quadrants hit profile with gamma fit. All quadrants have the same gamma fit taken from upper right plot since it has the most high value among all four. Notice: Upper left is quadrant 1 in ALICE system, upper right is quadrant 0, down left is quadrant 3 and down right is quadrant 2.

Finally the plots for the energy resolution are shown in figure 3.23. As it can be seen, the results became worse and the energy resolution deteriorated. This is a clear mark that this approach failed as well in the effort to improve the resolution.

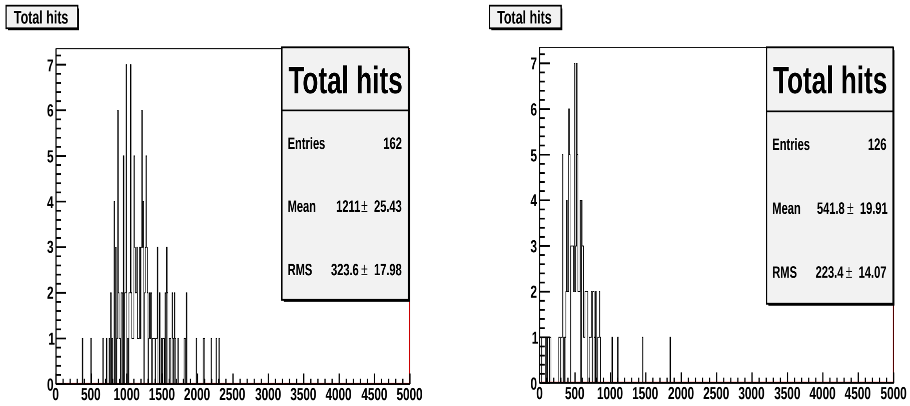

Figure 3.23: Number of hits per shower. Left: Runs 114-119 at 5 GeV. Energy resolution calculated to be 26.6%. Right: Runs 93-98 at 2 GeV. Energy resolution calculated to be 40.9%.

3.2.4 Corrected data, separation in four quadrants and calibration factors

It has been decided to continue with the same procedure but this time by drawing the average number of hits and not interpolating the ”dead” chips. So when we had a ”dead” chip we just skipped it. After applying the calibration factors we created the new quadrant profiles and by analysing them we tried to calculate again the energy resolution for the 2 and 5 GeV (figures 3.24-3.28). Still, what it can be seen is that once more our method didn’t seem to work and the energy resolution didn’t improve as well.

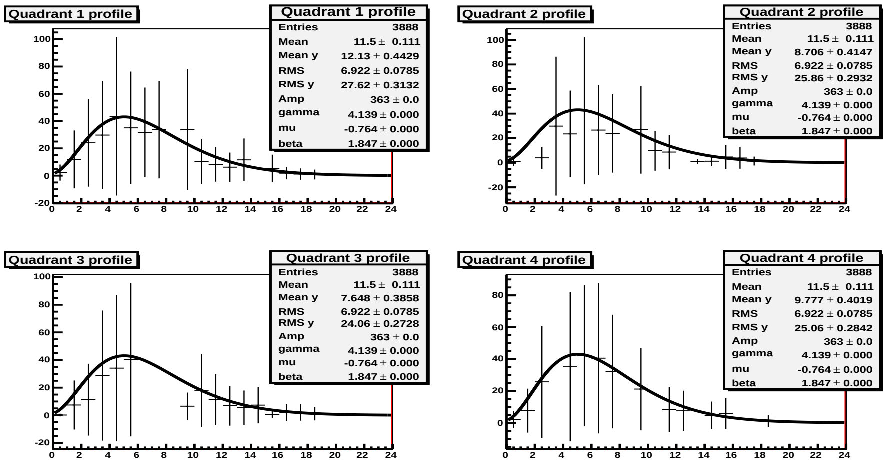

Figure 3.24: Runs 114-119 at 5 GeV. Quadrants hit profile with gamma fit. All quadrants have the same gamma fit taken from down right plot since it has the most high value among all four. Notice: Upper left is quadrant 0 in ALICE system, upper right is quadrant 3, down left is quadrant 2 and down right is quadrant 1.

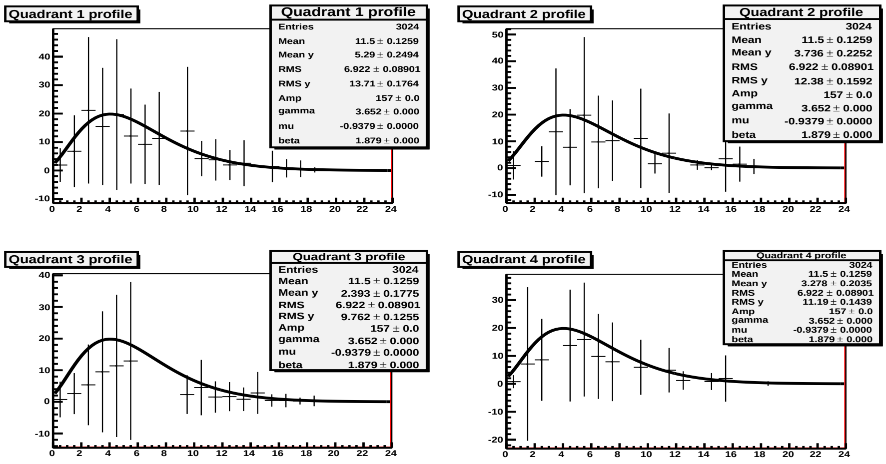

Figure 3.25: Runs 93-98 at 2 GeV. Quadrants hit profile with gamma fit. All quadrants have the same gamma fit taken from upper left plot since it has the most high value among all four. Notice: Upper left is quadrant 0 in ALICE system, upper right is quadrant 3, down left is quadrant 2 and down right is quadrant 1.

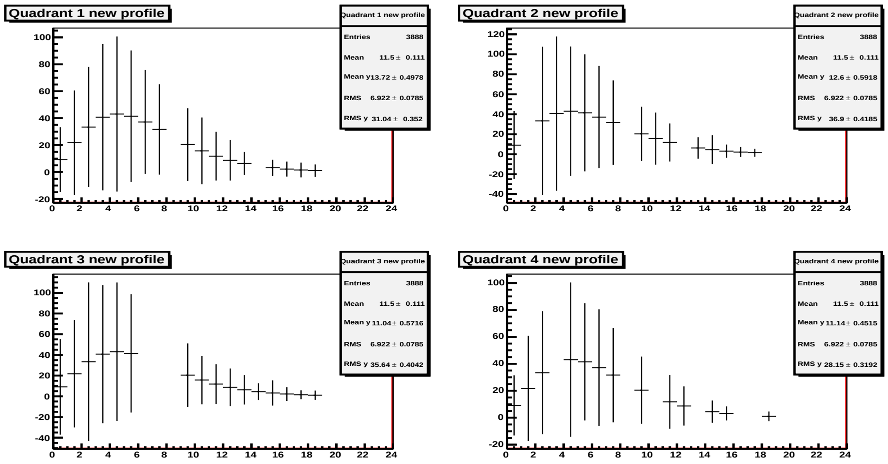

Figure 3.26: Runs 114-119 at 5 GeV. Quadrants corrected hit profile. Notice: Upper left is quadrant 0 in ALICE system, upper right is quadrant 3, down left is quadrant 2 and down right is quadrant 1.

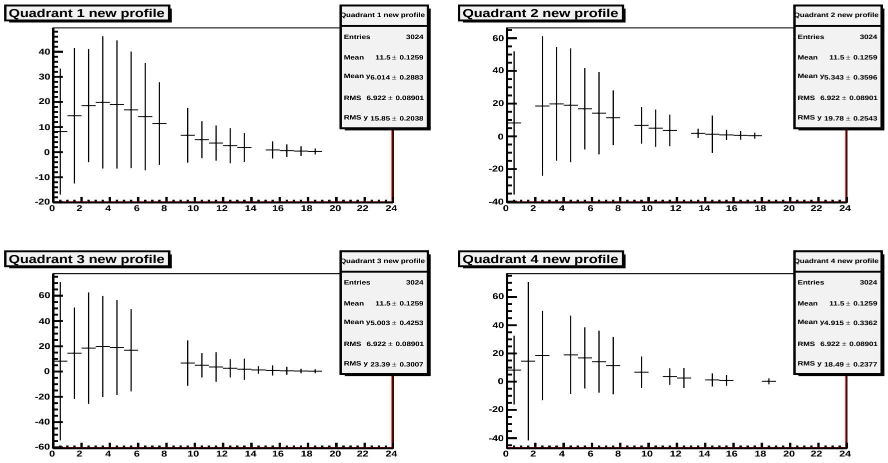

Figure 3.27: Runs 93-98 at 2 GeV. Quadrants corrected hit profile with gamma fit. Notice: Upper left is quadrant 0 in ALICE system, upper right is quadrant 3, down left is quadrant 2 and down right is quadrant 1.

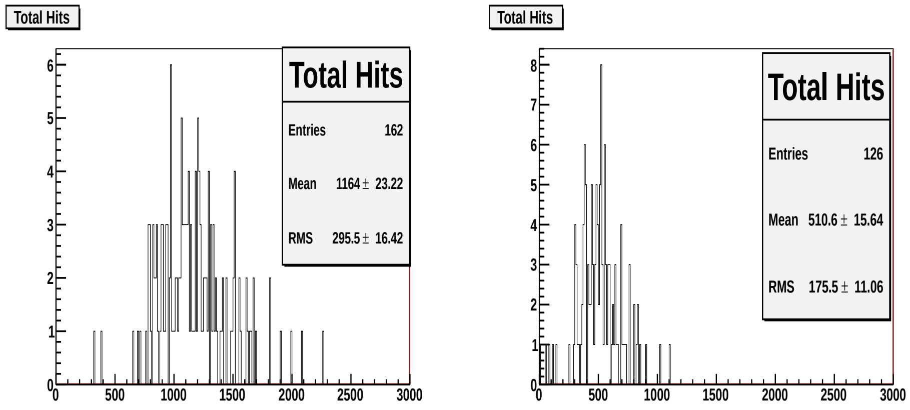

Figure 3.28: Left: Number of hits per shower. Runs 114-119 at 5 GeV. Energy resolution calculated to be 25.3%. Right: Runs 93-98 at 2 GeV. Energy resolution calculated to be 34.3%.

3.2.5 Corrected data, separation in four independent quadrants and step by step chip rejection

As a final approach for the calorimeter's calibration and the energy resolution improvement we decided to try was the following:

- The detector was split in four quadrants.
- In each quadrant specific cuts of 2.5 mm in each side were applied.
- The quadrant (”dominant” quadrant) in which the center of mass from each shower was located was found.
- We took into account only the hits in the ”dominant” quadrant for each shower, skipping the hits in the other three. In this way we treated each quadrant as a different ”detector”.
- We calculated the energy resolution before and after applying the calibration factors found with the same method as section 3.2.4.

For the 5 GeV data we now study runs 114-119 and for 2 GeV runs 93-98. For this method, the central trigger condition was cancelled due to the low statistics but the pile-up condition is still valid.

Before calibration

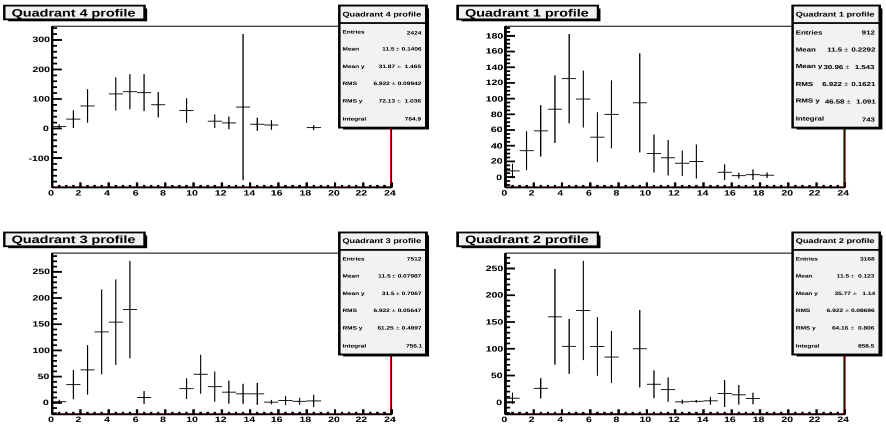

Figure 3.29: Runs 114-119 at 5 GeV. Quadrants profile. Notice: Upper left is quadrant 1 in ALICE system, upper right is 0, down left is 2 and down right is 3.

From figure 3.29 we calculated the ratio of the error over the mean value (figure 3.30). In this way, we decided which chips behave strangely and don't have a constant response (at this point we added in the table 3.1 except from chips 19, 59, 65, 90, 95 we had until now, chips 13, 25, 31, 35, 54, 60). Thus, a list that starts with the "worst working" chip in each quadrant and ends with the "best working" chip was made.

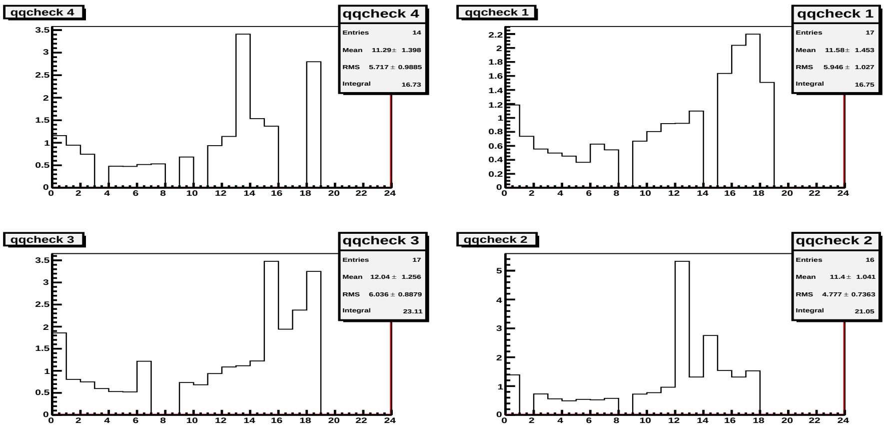

Figure 3.30: Runs 114-119 at 5 GeV. Chips response testing plots. Chips with the largest Y values are considered to be the "worst working chips". Notice: Upper left is quadrant 1 in ALICE system, upper right is 0, down left is 2 and down right is 3.

Using the information from figure 3.30, histograms with the average number of hits were made. In this plots, the average number of hits for 24 working chips, then for 23 working chips, and so on is shown. Each time we removed from our calculation a working chip until we are left with the broken chips, which means that the number of hits is almost zero (see figure 3.31). Upper left plot shows that if we skip 14 working chip and be left with the ten which are broken the number of hits is zero. This confirms figure 3.30 which shows that 10 chips are either broken or disconnected. The same holds for the rest quadrants. Next, we calculated the energy resolution but this time we began to remove chips starting from the first worst,then the second worst etc. A Gaussian was also drawn for the data, from which we calculated the energy resolution using the $\frac{\sigma}{mean}$ given from the fit. The summary plots are only presented in figures 3.32-3.33. For the detailed energy resolution plots see Appendix B, figures B.4-B.11.

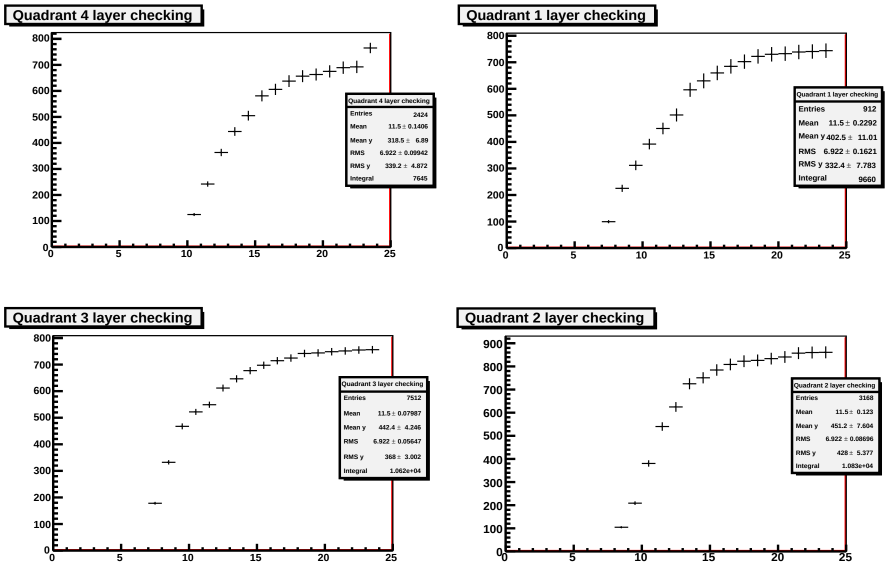

Figure 3.31: Runs 114-119 at 5 GeV. Average number of hits in each quadrant per number of working chips. Notice: Upper left is quadrant 1 in ALICE system, upper right is quadrant 0, down left is quadrant 2 and down right is quadrant 3.

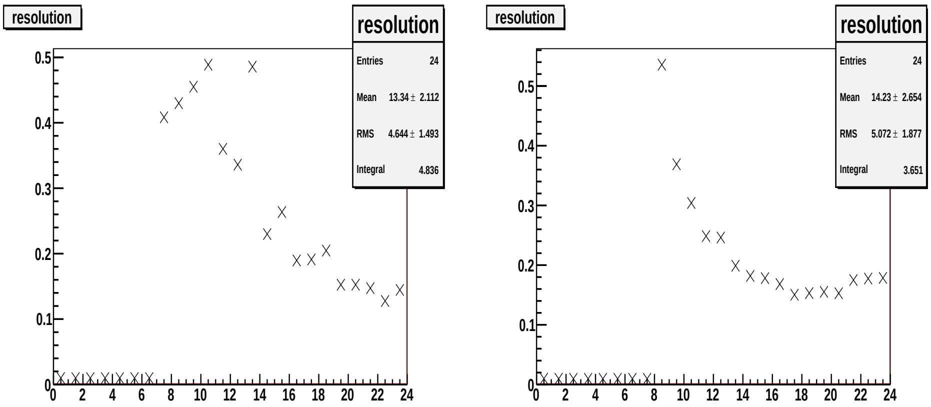

Figure 3.32: Runs 114-119 at 5 GeV. Resolution versus number of working chips per quadrant. Left: Quadrant 0: The best energy resolution value is 13.7% at 23 working chips. Right: Quadrant 3: The best energy resolution value is 14.7% at 18 working chips.

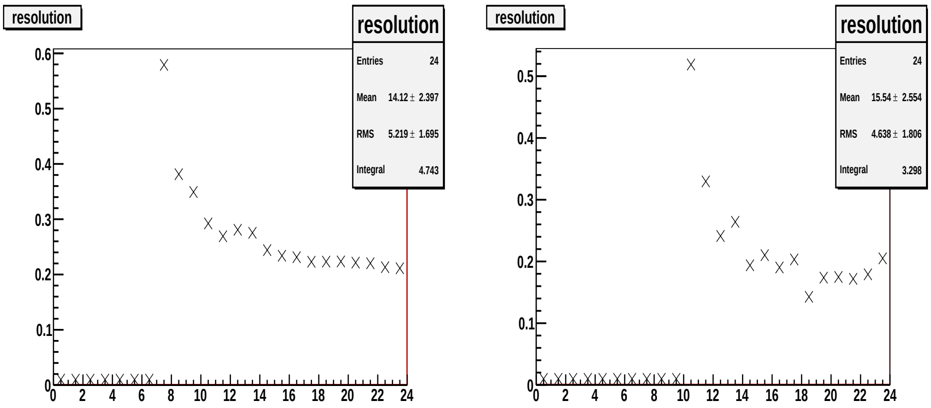

Figure 3.33: Runs 114-119 at 5 GeV. Resolution versus number of working chips per quadrant. Left: Quadrant 2: The best energy resolution value is 21.1% at 24 working chips. Right: Quadrant 1: The best energy resolution value is 14.2% at 19 working chips.

We followed the exact same steps for the 2 GeV data set (figures 3.34-3.38).

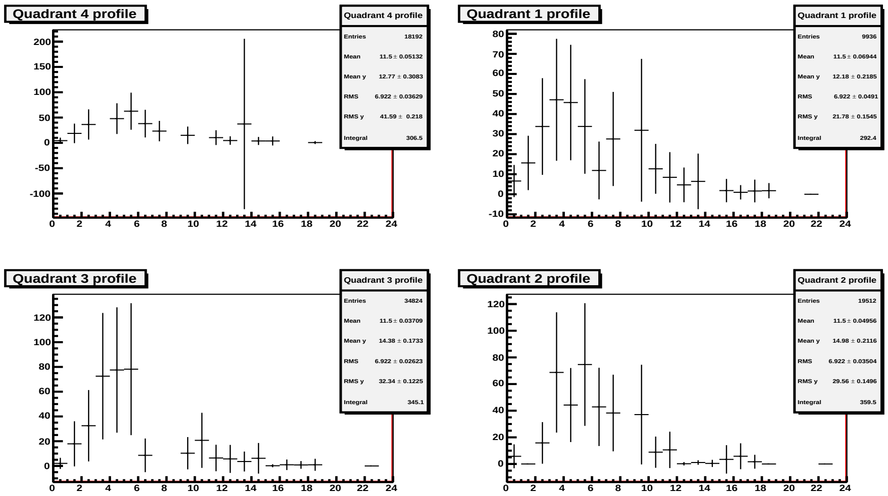

Figure 3.34: Runs 93-98 at 2 GeV. Quadrants hit profile. Notice: Upper left is quadrant 1 in ALICE system, upper right is quadrant 0, down left is quadrant 2 and down right is quadrant 3.

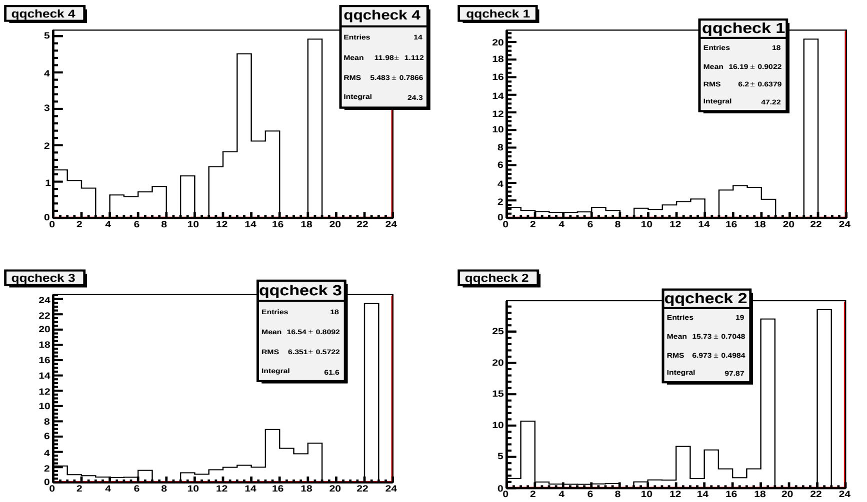

Figure 3.35: Runs 93-98 at 2 GeV. Chips response testing plots. Chips with the largest Y values are considered to be the ”worst working chips”. Notice: Upper left is quadrant 1 in ALICE system, upper right is quadrant 0, down left is quadrant 2 and down right is quadrant 3.

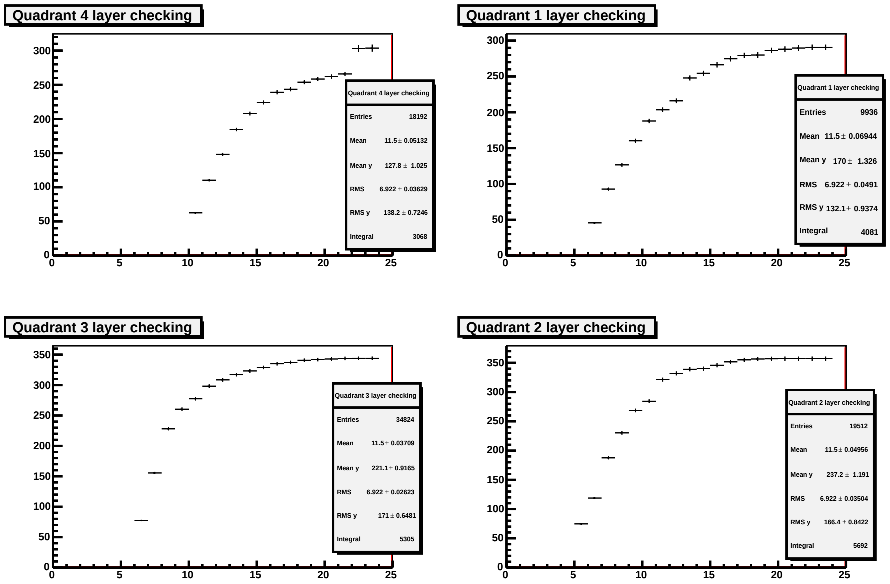

Figure 3.36: Runs 93-98 at 2 GeV. Average number of hits in each quadrant per number of working chips. Notice: Upper left is quadrant 1 in ALICE system, upper right is quadrant 0, down left is quadrant 2 and down right is quadrant 3.

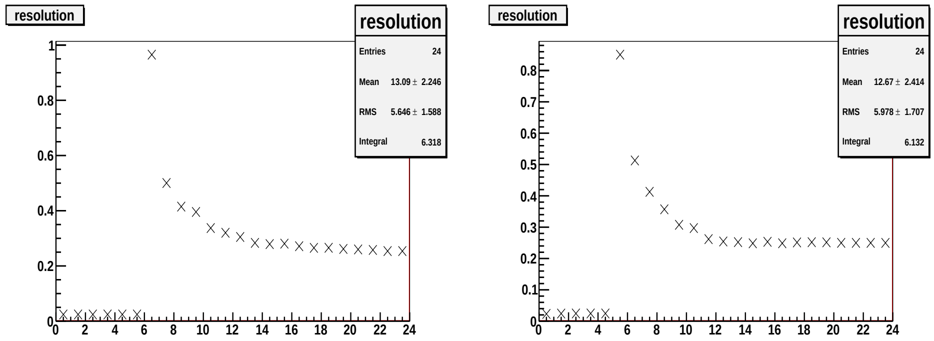

Figure 3.37: Runs 93-98 at 2 GeV. Resolution versus number of working chips per quadrant. Left: Quadrant 0: The best energy resolution value is 25.4% at 23 working chips. Right: Quadrant 3: The best energy resolution value is 25.8% at 24 working chips.

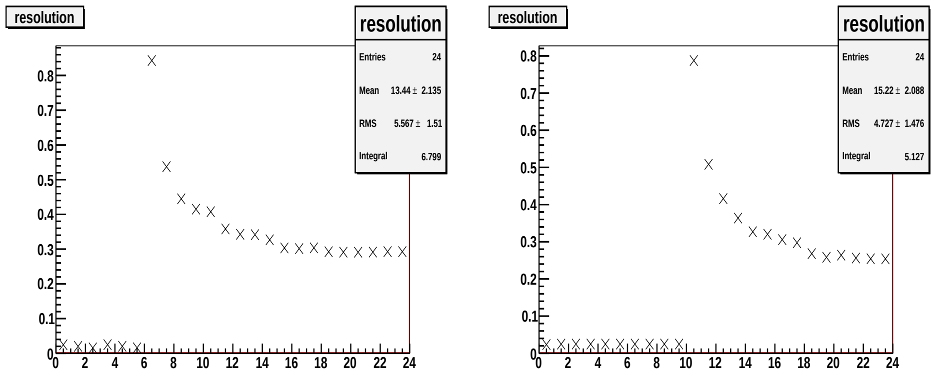

Figure 3.38: Runs 93-98 at 2 GeV. Resolution versus number of working chips per quadrant. Left: Quadrant 2: The best energy resolution value is 29.1% at 23 working chips. Right: Quadrant 1: The best energy resolution value is 25.4% at 24 working chips.

After calibration

After examining the energy resolution from the data without making any corrections or changes, we further tried to apply the C_c the way we did in section 3.2.4. The same gamma function in each quadrant was used, from which the calculation of the C_c for the working chips was made. The interpolation of the "dead" chips was also tried but it didn't help, that's why the results after the interpolation are not presented. Again, only the summary of the results for the energy resolution is shown, while the detailed plots are in Appendix B, figures B.12-B.19.

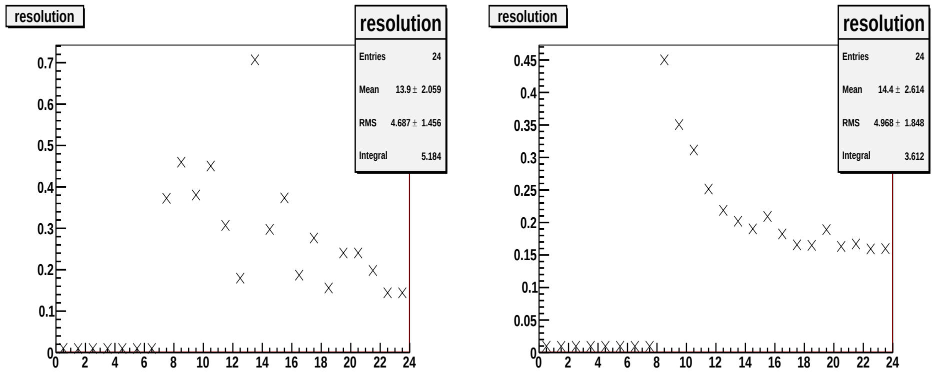

Figure 3.39: Runs 114-119 at 5 GeV. Resolution versus number of working chips per quadrant. Left: Quadrant 0: The best energy resolution value is 14.4% at 24 working chips. Right: Quadrant 3: The best energy resolution value is 13.4% at 23 working chips.

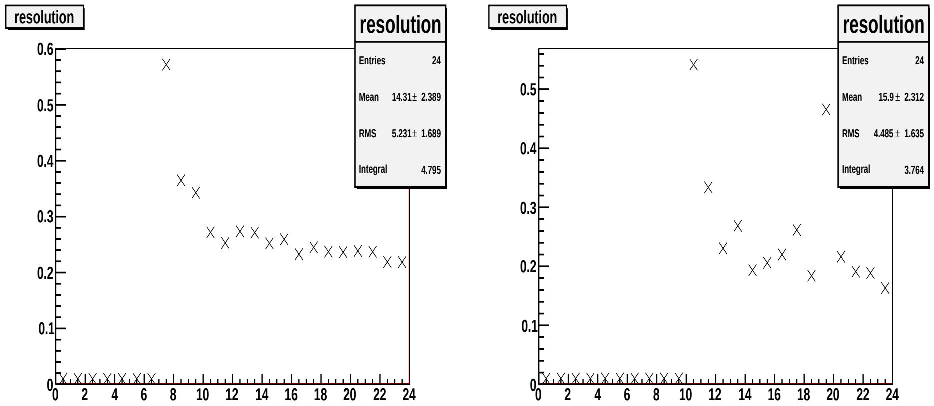

Figure 3.40: Runs 114-119 at 5 GeV. Resolution versus number of working chips per quadrant. Left: Quadrant 2: The best energy resolution value is 21.8% at 24 working chips. Right: Quadrant 1: The best energy resolution value is 16.3% at 24 working chips.

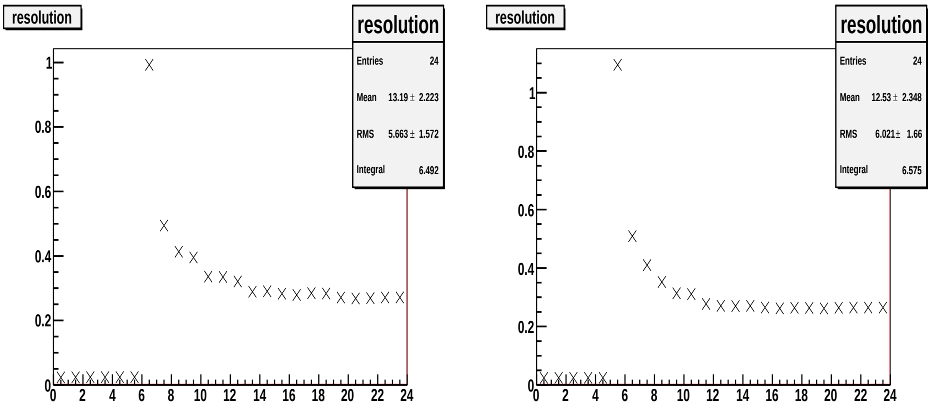

Figure 3.41: Runs 93-98 at 2 GeV. Resolution versus number of working chips per quadrant. Left: Quadrant 0: The best energy resolution value is 26.8% at 21 working chips. Right: Quadrant 3: The best energy resolution value is 25.7% at 19 working chips.

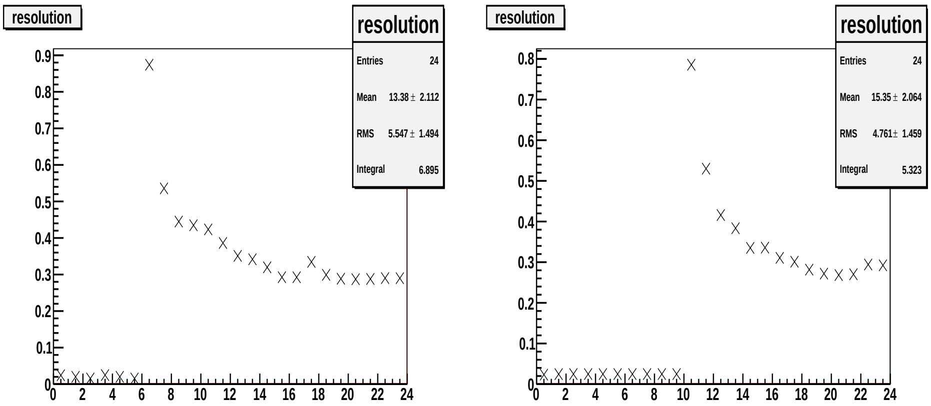

Figure 3.42: Runs 93-98 at 2 GeV. Resolution versus number of working chips per quadrant. Left: Quadrant 2: The best energy resolution value is 28.7% at 21 working chips. Right: Quadrant 1: The best energy resolution value is 26.8% at 21 working chips.

3.2.6 Discussion

From the all the figures shown in section 3.2 it can be seen that applying the calibration factors in the data deteriorated our results. This shows that improving the shower profiles doesn't lead to an improvement of the resolution. Moreover the interpolation of the broken layer 8 also did not improve the energy resolution. The conclusion of figures 3.29-3.42 is that the amount of broken chips or not correctly working chips, influenced to a great extent our results. The best energy resolution calculated was 13.7% for the 5 GeV and 25.4% for the 2 GeV data set. However, these results cannot be considered quite reliable since we talk about quadrants and not about the whole prototype. Still, these values which are coming from the Gaussian fit in our data, are still quite far from the expected values of 9% and 14% for the 5 and 2 GeV, respectively. For the whole prototype the best values for the resolution we obtained were 18.4% for the 5 GeV and 28.2% for the 2 GeV data sets, respectively.

3.3 Lateral profiles at 2 and 5 GeV

In this section, the lateral profiles of the calorimeter are presented, which are useful for studying the lateral development of the showers but also for calculating the Moliere radius of the calorimeter. Along with the lateral profiles, the central trigger condition was also tested as well as the alignment of the calorimeter.

3.3.1 Central trigger condition testing

The central trigger bit is produced by the coincidence of the small vertical and horizontal scintillators (see figure 2.6). The calorimeter again is separated in four quadrants. The center of mass (i.e the average x,y coordinates) of each shower is calculated by examining all the hits. By applying the the central trigger bit "on", what we expected to see is much less hits and ideally all the average x,y coordinates of each shower in the region between -0.5 cm $\leq$ x $\leq$ 0.5 cm and -0.5 cm $\leq$ y $\leq$ 0.5 cm. Indeed, this is shown in figure 3.43-3.44 with very few exceptions. This means that our trigger bit system using the two small scintillators was almost perfectly working.

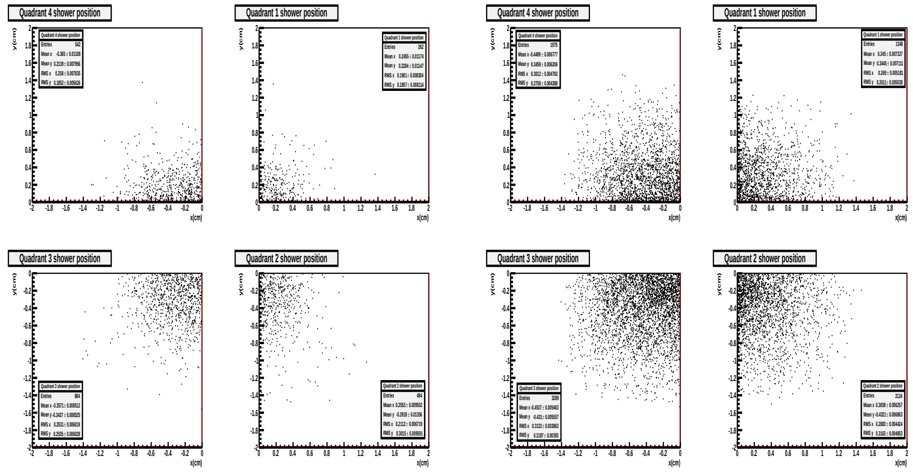

Figure 3.43: Left: Average shower position for the 5 GeV data. Right: Average shower position for the 2 GeV data.

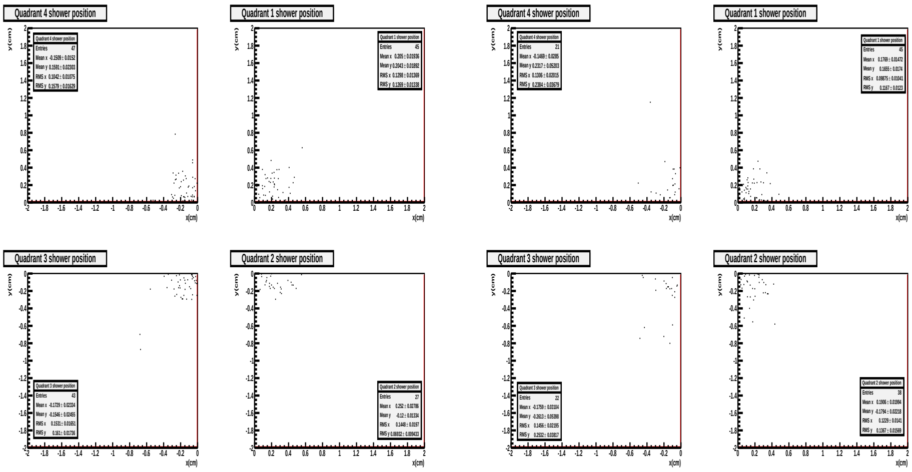

Figure 3.44: Left: Average shower position with central trigger condition ”on”for the 5 GeV data. Right: Average shower position with central trigger condition ”on”for the 2 GeV data.

3.3.2 Alignment investigation

Moving on, we investigated the calorimeter alignment for both x and y direction. For each shower and each layer we calculated the x and y of the hits. Afterwards, we calculated the average x and y for each shower for the whole calorimeter. For each layer, we applied the following calculation

$$A_x = \sum_{i=0}^{N} \frac{x_l - x_{det}}{N} \tag{3.3}$$

and

$$A_y = \sum_{i=0}^{N} \frac{y_l - y_{det}}{N} \tag{3.4}$$

where N is the number of showers and x_l, x_{det} the x,y coordinates for the layer and the detector respectively. In figures 3.45-3.46 the result values from eq. 3.1-3.2 versus the layer number for the 5 and 2 GeV are shown. These plots demonstrate the calorimeter’s alignment.

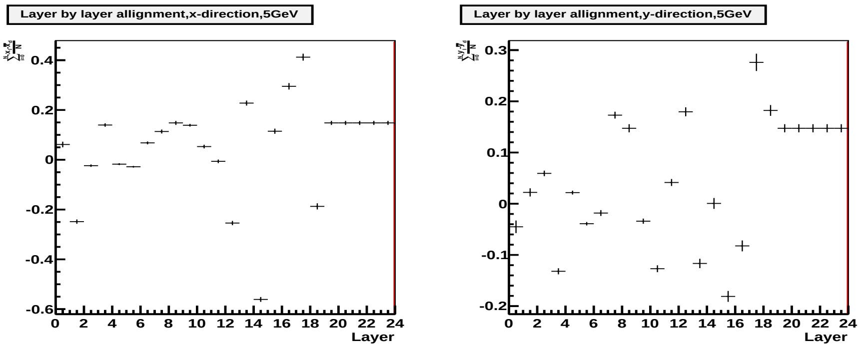

Figure 3.45: Relative alignment A_x and A_y versus layer number for the 5 GeV data. Vertical axis in mm.

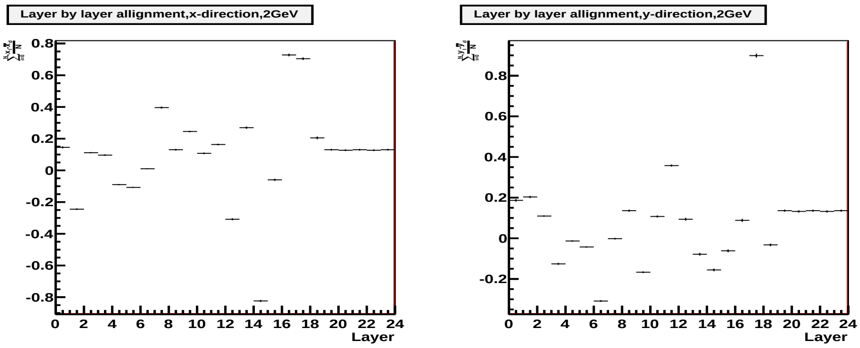

Figure 3.46: Relative alignment A_x and A_y versus layer number for the 2 GeV data. Vertical axis in mm.

By having a closer look at figures 3.45-3.46, it can be seen that the "misalignment" for layers with broken chips happens in the opposite x and y coordinates of those that the broken chip has. For example, for layer 1 a "misalignment" in -x and +y direction appears. Looking at the table 3.1 we see that in layer 1 there is a broken chip in quadrant 3 which has +x, -y coordinates. In this way, the average x and y of this layer is "pushed" in -x and +y direction. The same holds for most of the layers with broken chips.

The same conclusion is drawn if we have a closer to each layer separately (figure 3.47). Taking into account the fact that we have broken chips and that the "misalignment" seen is less than 1 mm in all the layers in both directions, we can safely say that for the beam test there was not an important construction problem.

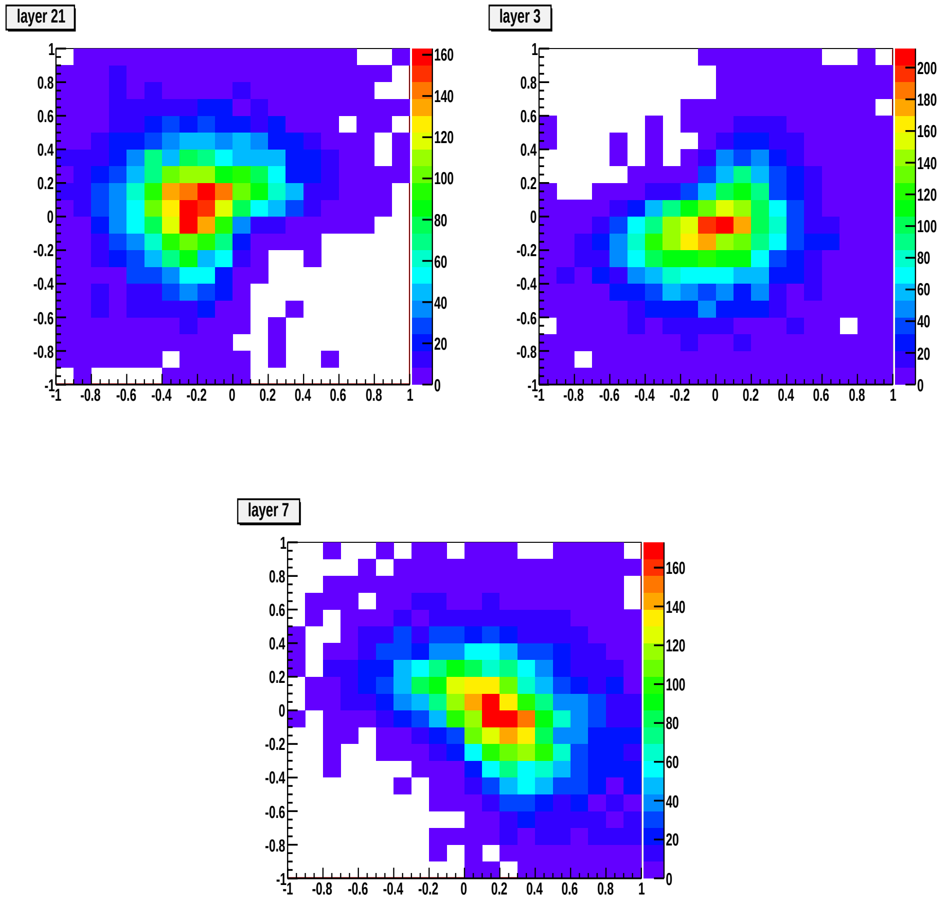

Figure 3.47: Upper left: Layer 1 relative shower position at 5 GeV. Broken chip with coordinates at +x and -y. Upper right: Layer 3 relative shower position at 5 GeV. Broken chip with coordinates at -x and +y. Down: Layer 7 relative shower position at 5 GeV. Broken chip with coordinates at -x and -y.

3.3.3 Lateral profiles and Moliere radius

The last step of the analysis was the study of the lateral profiles of the showers. We divided the detector in four quadrants and calculated the average number of hits in each one. The central trigger condition is now again applied for our data. To study the lateral profiles and investigate the Moliere radius we concentrated to a volume in the prototype which seems like a cylinder. By taking the average x and y coordinates of the showers as the point of reference we "drew" a circle around it for each layer. Then we increased the radius of this circle by a step of 0.2 mm until we reached the end of the detector at 2 cm. In the plots the average number of hits per radius for each quadrant and the particle density per area (figures 3.49-3.50) is shown. From figure 3.49, one can roughly estimate the Moliere radius by looking at the maximum of average hits for each quadrant and try to see where the 90% is located. For both 2 and 5 GeV we can see that the 90% of the maximum is around 11 mm, which verifies theory (see eq. 2.3).

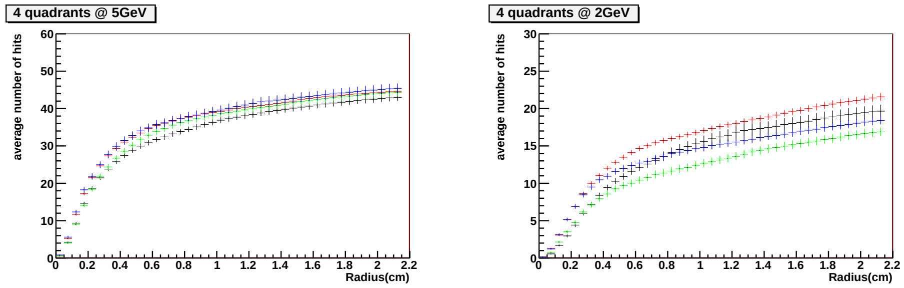

Figure 3.48: Left: Lateral profile for 5 GeV data. Right: Lateral profile for 2 GeV data. Black: Quadrant 0, Red: Quadrant 1, Green: Quadrant 2, Blue: Quadrant 3.

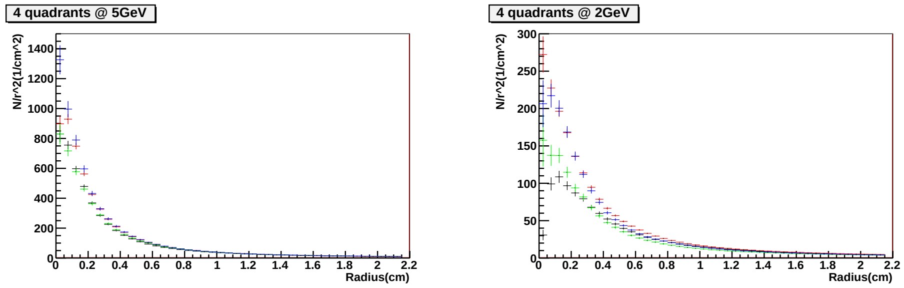

Figure 3.49: Left: Particle density for 5 GeV data. Right: Particle density for 2 GeV data. Black: Quadrant 0, Red: Quadrant 1, Green: Quadrant 2, Blue: Quadrant 3.

3.3.4 Discussion

From the analysis made in section 3.3 it is clear that the lateral profiles looked as expected. The Moliere radius was found to be at 11 mm, as it was more or less expected, through the plots for both 2 and 5 GeV. The central trigger condition that was frequently used in the analysis proved to work almost perfectly. Finally, the alignment test showed that there was a small problem of approximately 0.1-0.2 mm, but it was most likely because of the broken chips we had and not due to construction alignment or assembly problems. However, the deviation observed was insignificant to affect our measurements.

Chapter 4

Conclusions

In conclusion, FoCal prototype showed a quite stable behaviour and worked well as an electromagnetic calorimeter. From the analysis conducted some of the prototype's characteristics were proven to be as expected, such as its radiation length and Moliere radius. On the other hand, the energy resolution is not what we would expect. Even if several methods were followed to improve the resolution, the result remained far from the expected. Nevertheless, we should have in mind that during the beam test we faced several problems such as broken chips, disconnected chips and mistakes in chip tuning, which definitely affected our results and deteriorated the energy resolution. Currently, latest results obtained from simulations done by our group, in which most of the problems that were faced in this study were included, show that the energy resolution deteriorates to similar values obtained in this study. In the future, increase in the statistics, improvements in the analysis methodology and the prototype settings and tries to follow the same methods in the simulations should be made in order to obtain better results and maybe along with replacing the broken chips with new (even if this would be expensive).

Acknowledgements

I would like to take this opportunity to thank the following people: First and foremost, I would like to express my gratitude to Martijn Reicher for his priceless help. Through our daily contact, I greatly improved my programming skills. Even if I was asking him questions several times per day, he was always willing to help and capable to answer thanks to his sharp mind. We also had a really nice time during the beam tests at CERN and DESY. Furthermore, I would like to thank Dr. Gert-Jan for his daily supervision and for the in depth conversations in his office about the project and my work, as well as for taking me in the beam tests at CERN and DESY which was one of the best experiences in my life (special thanks to Ton van der Brink for the whole CERN tour) despite the night shifts task. Prof. Thomas Peitzmann for the opportunity to work for the FoCal group and being part of a really creative and high level environment. Moreover, I would like to thank Davide Lodato, who became my friend, for being there for the times I needed some help and for the really great time at the work breaks down at BBL building and at the DESY beam test. I would also like to thank Elena Rocco, who, even if she became part of the group just 10 months ago, she helped me so much and she pushed me to do things with her own soft way. Finally, I would also like to thank Andrea Dubla for the great time at CERN and the work breaks down at BBL building and Nikola Poljak who is a great person, a brilliant mind and became my friend even if he stayed at the FoCal group for less than 5 months. Thanks to everyone in the 7th floor of the BBL building.

Bibliography

[1] Richard Wigmans. *Calorimetry: Energy measurement in particle physics*, volume 107. Oxford University Press, 2000.

[2] *http://pdg.lbl.gov/2011/download.*

[3] Heidelberg University. *Interactions of particles with matter, Lecture 2.*

[4] Jim Brau. Calorimetry lectures. *SLUO Lecture Series*, 1999.

[5] Christian W Fabjan and Fabiola Gianotti. Calorimetry for particle physics. *Reviews of Modern Physics*, 75(4):1243, 2003.

[6] Guenter Grindhammer and S Peters. The parameterized simulation of electromagnetic showers in homogeneous and sampling calorimeters. *arXiv preprint hep-ex/0001020*, 2000.

[7] Leonardo Rossi, Peter Fischer, and Tilman Rohe. *Pixel detectors: From fundamentals to applications.* Springer, 2006.

[8] Focal LoI. 2013.

[9] Presentation by Elena Rocco at the annual Nikhef Jamboree 2012, Utrecht University, ALICE experiment.

[10] Presentation by Martijn Reicher, Utrecht University, ALICE experiment.

[11] D Fehlker, J Alme, A van den Brink, AP de Haas, G-J Nooren, M Reicher, D Röhrich, M Rossewij, K Ullaland, and S Yang. Electronics for a highly segmented electromagnetic calorimeter prototype. *Journal of Instrumentation*, 8(03):P03015, 2013.

[12] Drawings from Ton van Brink, Utrecht University, ALICE experiment.

[13] Bachelor thesis, J.V.S van Wijck, Het testen van FoCal, Report number: UU(SAP) 12-8.

Appendix A

Appendix A

The equipment used for the tests is:

- **Discriminator unit (Octal Discriminator Unit Nikhef) :** Is an electronic signal processing device, designed to mimic mathematical operation of finding a maximum of a pulse by finding the zero of its slope. The pulse taken by the scintillator is analog. The discriminator differentiates a copy of the signal input in order to take a digital signal. The threshold level mentioned above is set in the discriminator.
- **Quad scaler and counter/timer unit (CAEN Model N145) :** Is an electronic device that can be used to measure counts in a specific time interval, or it can be used as a timer. Time intervals can be set for either msec or μsec.
- **Coincidence unit (LeCroy Model 622) :** It is a device that implements a Boolean function that is a logical operation on one or more logic inputs and produces one single logic output. It operates both AND and OR functions.
- **TTL to NIM converter unit (LeCroy Model 222) :** This device changes the ttl signal to a nim signal. In digital electronics, there are many different logic families. Two of them are the NIM family and the TTL family. A NIM signal has the following definition of a digital "1" and a digital "0": when the signal voltage is between -0.8 V and -1 V, its a digital "1", while when it is exactly 0 V, its a digital "0". A TTL signal has the following definition of a digital "1" and a digital "0": when a signal voltage is between 1.5 V and 5 V, its a digital "1".While when it is between 0 V and 0.7 V, its a digital "0".
- **Generator unit (LeCroy Model 222):** This electronic device takes the signal coming from the detectors and the coincidence units and produces a normal signal used for triggering. We can also insert a time delay using this device.

- **Delay unit (LeCroy Model 222) :** This device allows us to set a delay (few nsec) to our signals in order to have many signals at a time coincidence. Thus, we can have a signal in our input and take the output of the signal with a preferable time delay.
- **Signal splitter (Signal Splitter Unit Nikhef) :** This is a simple electronic device that is used when we want to use the same signal in different units. With this device we can insert one signal and take up to 8 of the same.

Table A.1: Simple, coincidence and accidental coincidence counts of the scintillators.

	Front scintillator	Back scintillator		
Voltage(V)	Counts per sec	Counts per sec	Coincidence counts per sec	Accidental coincidence counts per sec(10^{-9})
1700	1.22	1.85	0.01	157.99
1710	1.39	1.97	0.01	192.38
1720	1.48	2.12	0.04	220.52
1730	1.63	2.17	0.05	249.99
1740	1.86	2.42	0.09	315.08
1750	2.09	2.65	0.10	387.69
1760	2.28	2.88	0.11	460.85
1770	2.45	3.2	0.10	550.14
1780	2.69	3.31	0.14	623.27
1790	2.92	3.59	0.08	734.54
1800	3.28	3.79	0.11	870.97
1810	3.65	3.98	0.11	1017.72
1820	4.09	4.28	0.17	1227.16
1830	5.04	4.42	0.17	1561.49
1840	6.71	5.43	0.14	2551.61
1850	10.46	7.79	0.16	5706.03
1860	16.14	9.29	0.17	10501.18
1870	26.63	9.49	0.17	17697.89
1880	42.10	9.86	0.24	28988.40
1890	61.49	10.02	0.19	43157.02
1900	84.80	10.16	0.20	60314.03
1910	117.10	10.6	0.25	86890.43
1920	151.69	11.5	0.25	122110.51

Table A.2: Trigger bits from run 115.

Virtex	Spill	Spill triggers	FxB triggers	PxB triggers	PxHxV triggers	PxF triggers
0	0	817	30	22	4	38
0	1	818	31	21	3	41
0	2	816	0	0	1	1
0	3	816	33	18	1	38
0	4	816	34	22	3	50
0	5	816	45	25	6	50
0	6	816	46	25	4	49
0	7	818	40	25	3	43
0	8	814	28	17	1	32
0	9	816	0	0	0	1
0	10	816	37	24	1	47
0	11	815	15	11	1	26
0	12	816	31	18	3	35
0	13	816	33	22	4	38
0	14	816	8	4	2	6
0	15	816	38	23	1	37
0	16	816	7	4	1	6
1	0	817	31	22	3	38
1	1	817	30	23	3	41
1	2	816	0	0	1	2
1	3	816	33	17	1	36
1	4	816	33	22	3	47
1	5	817	45	16	5	48
1	6	816	46	24	4	50
1	7	818	43	25	3	44
1	8	814	29	17	1	31
1	9	816	0	0	0	1
1	10	816	38	23	1	47
1	11	816	15	12	1	26
1	12	816	31	18	3	34
1	13	816	32	24	4	36
1	14	816	8	6	2	9
1	15	816	37	23	1	37
1	16	816	7	4	1	6

Appendix B

Appendix B

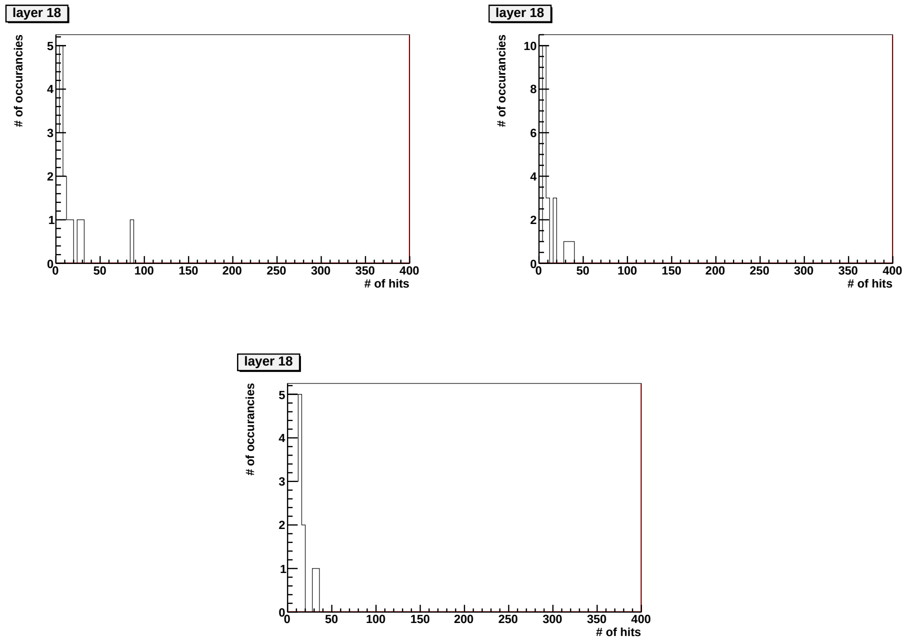

Figure B.1: From left to right: Layer 18 profile plots for 5 GeV, run 114, spill 001 to spill 003.

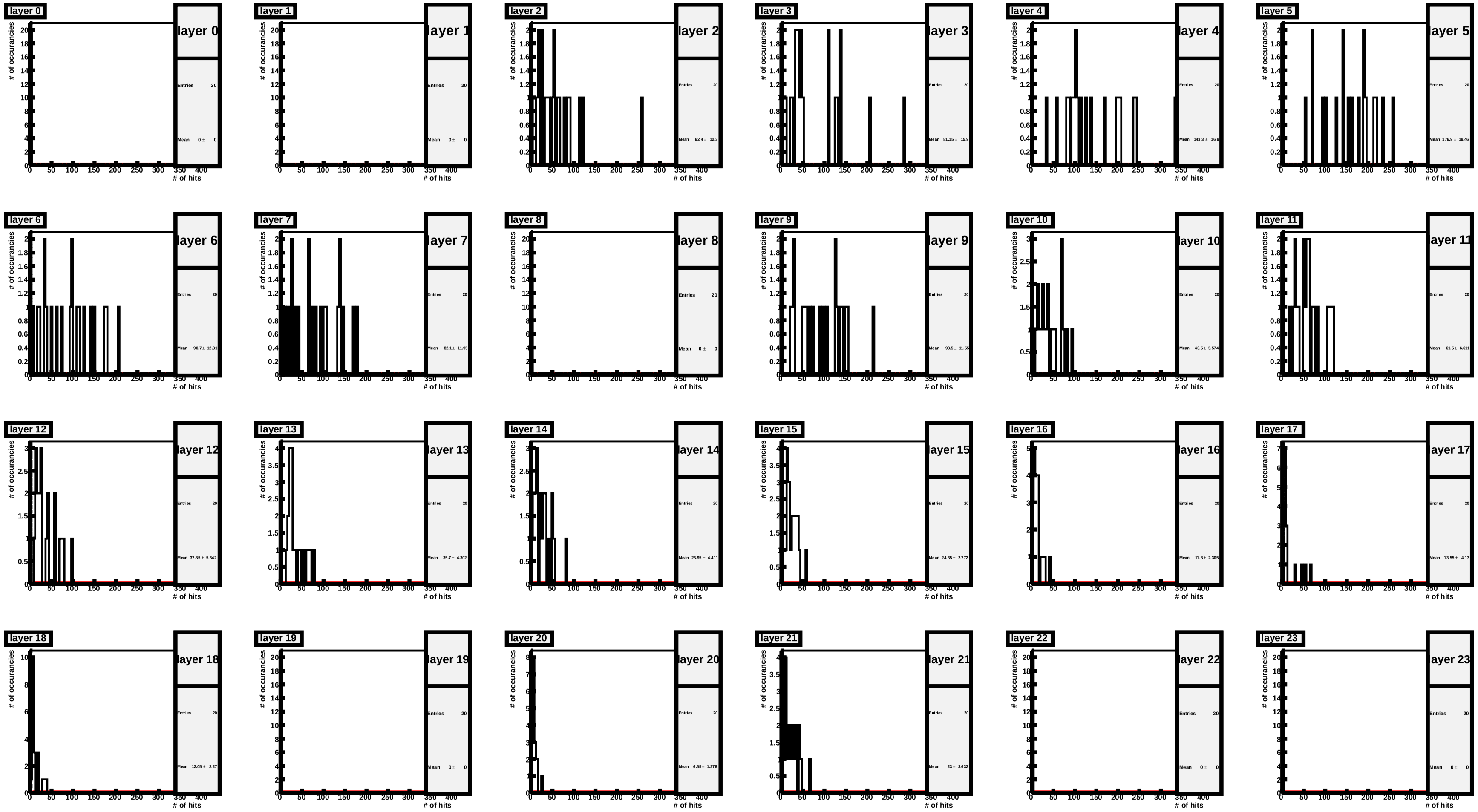

Figure B.2: Layers 0-24 profile plots for 5 GeV, run 114 spill 002. Notice that layers 20 and 21 are layers 0 and 1 in the detector respectively.

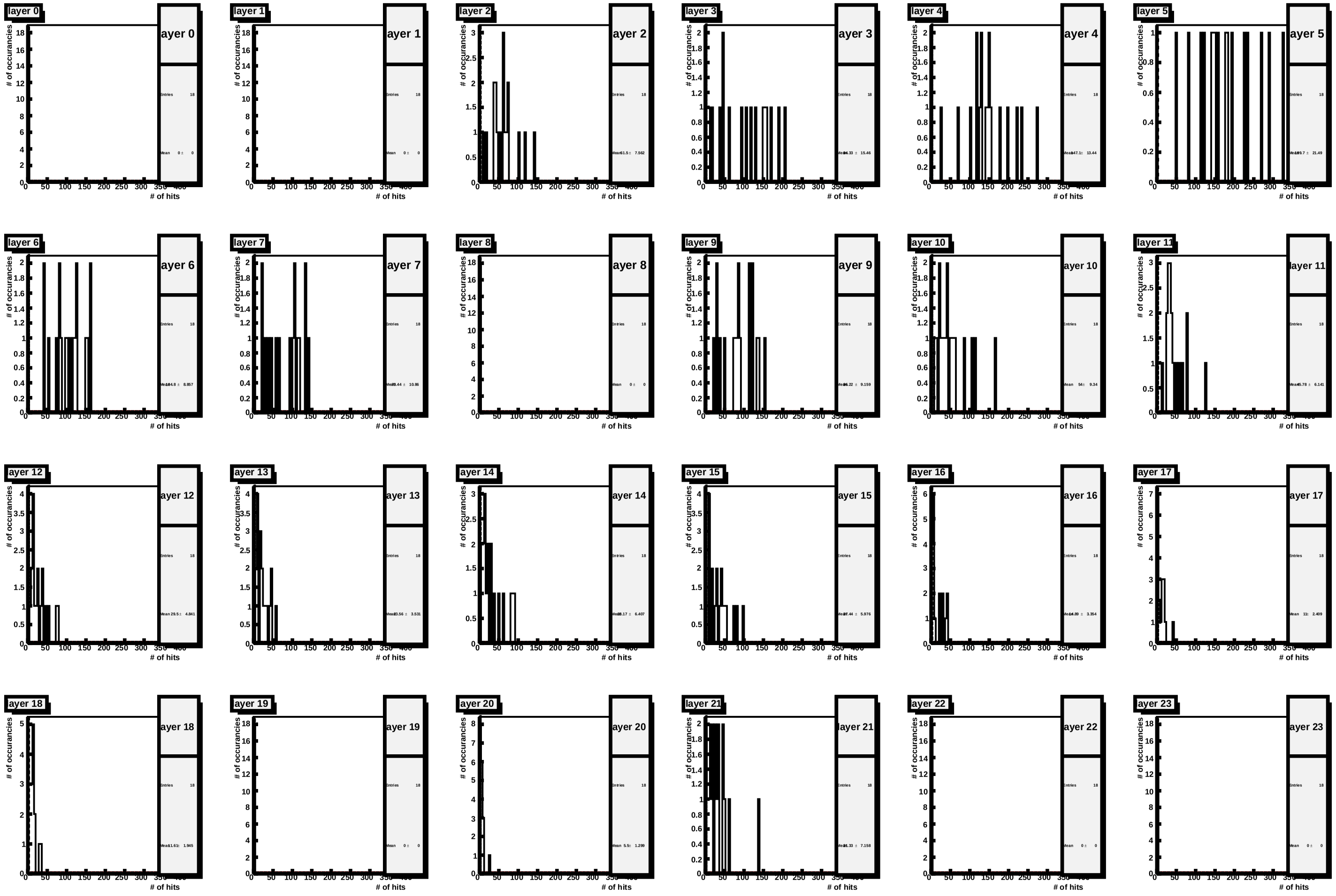

Figure B.3: Layers 0-24 profile plots for 2 GeV, run 114 spill 002. Notice that layers 20 and 21 are layers 0 and 1 in the detector respectively.

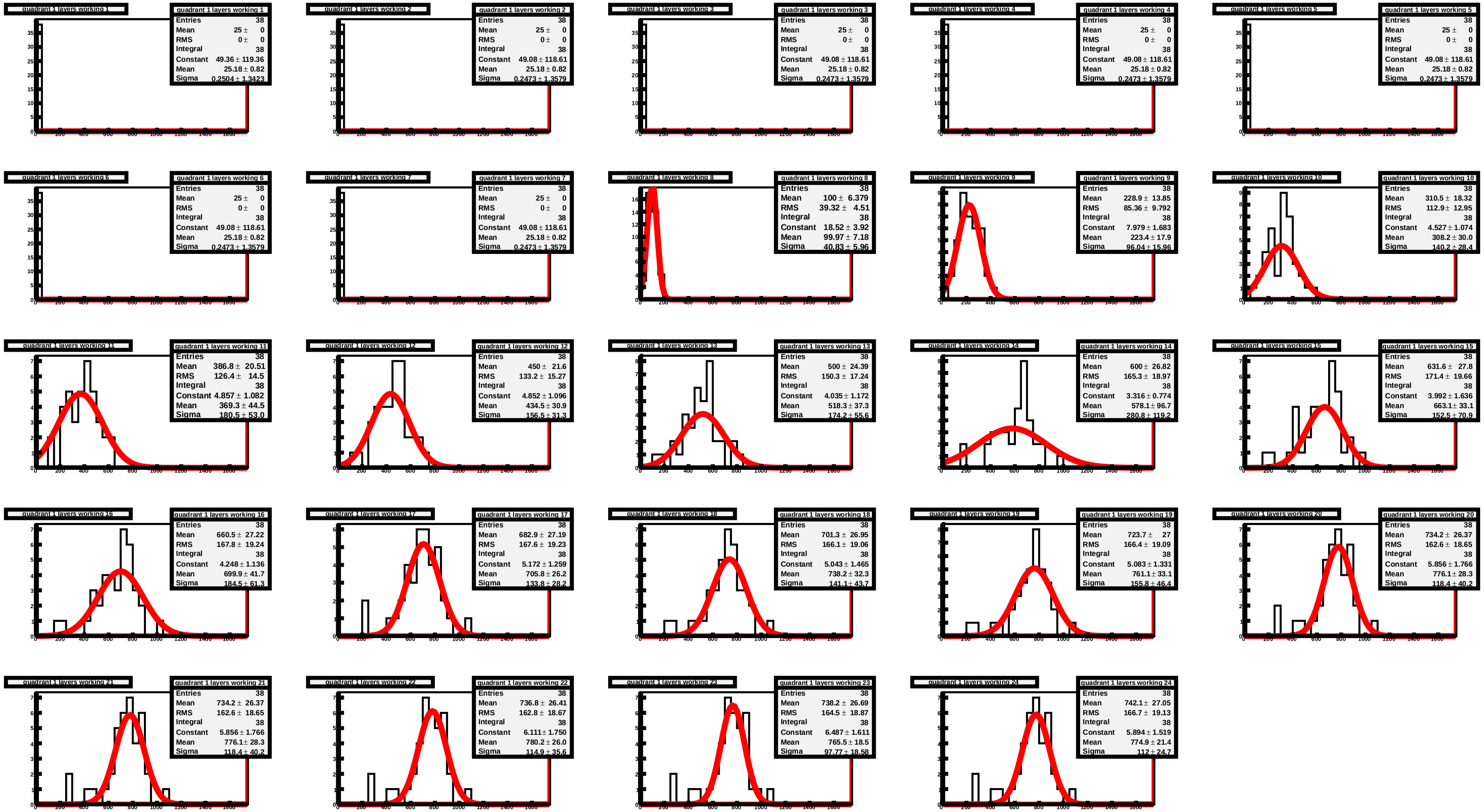

Figure B.4: Runs 114-119 at 5 GeV. Quadrant 0: The best energy resolution value is 12.7% at 23 working chips.

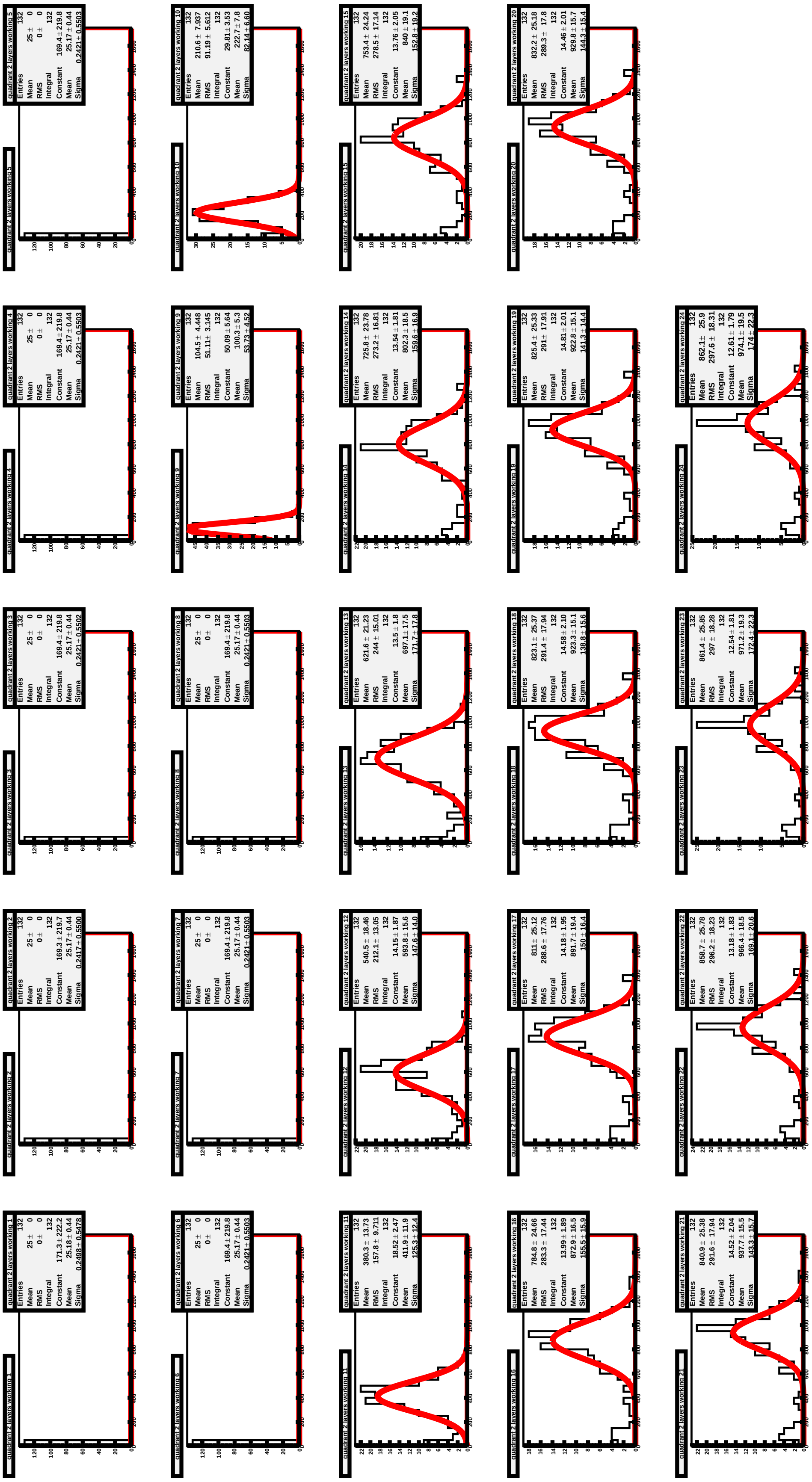

Figure B.5: Runs 114-119 at 5 GeV. Quadrant 3: The best energy resolution value is 15% at 18 working chips.

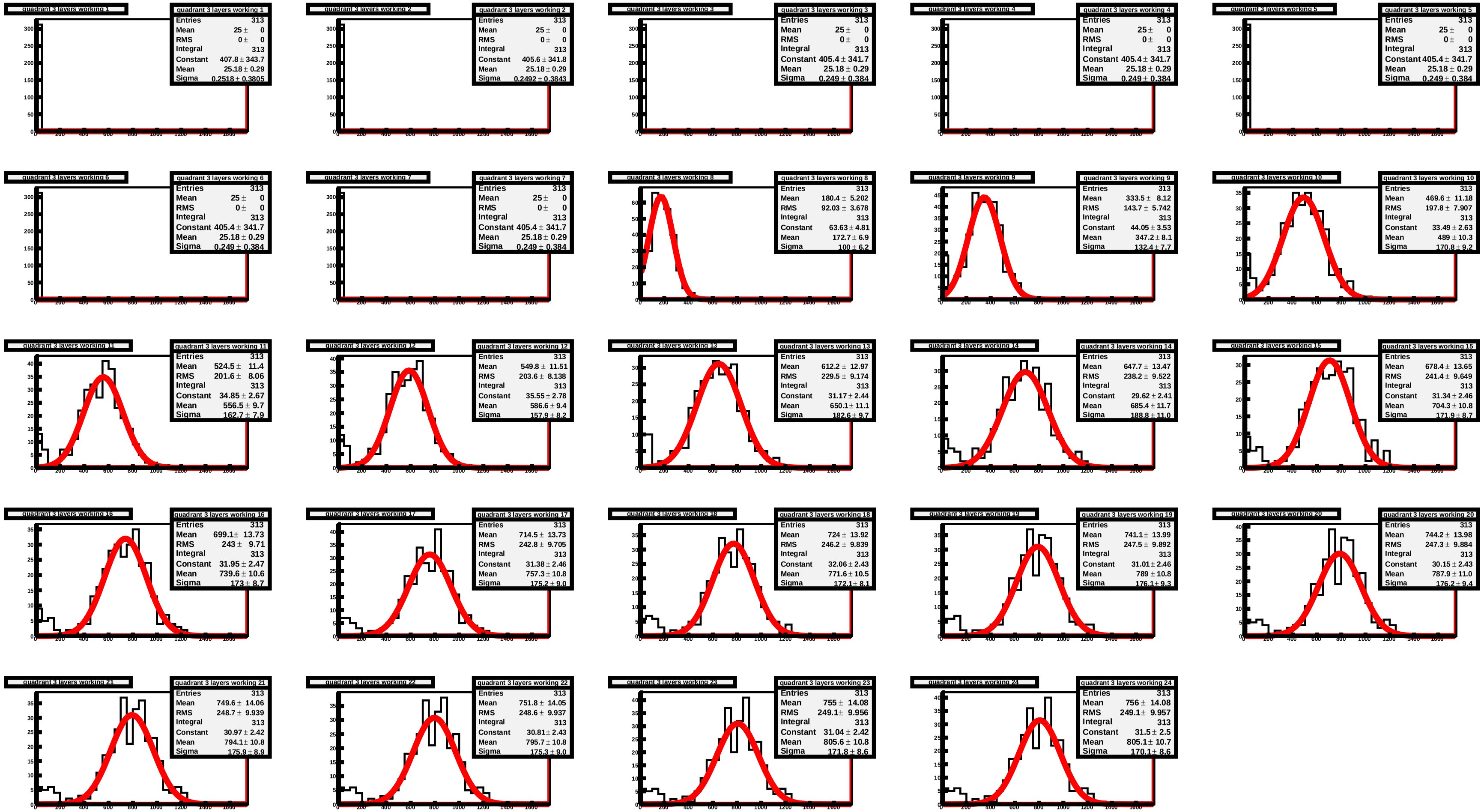

Figure B.6: Runs 114-119 at 5 GeV. Quadrant 2: The best energy resolution value is 21.1% at 24 working chips.

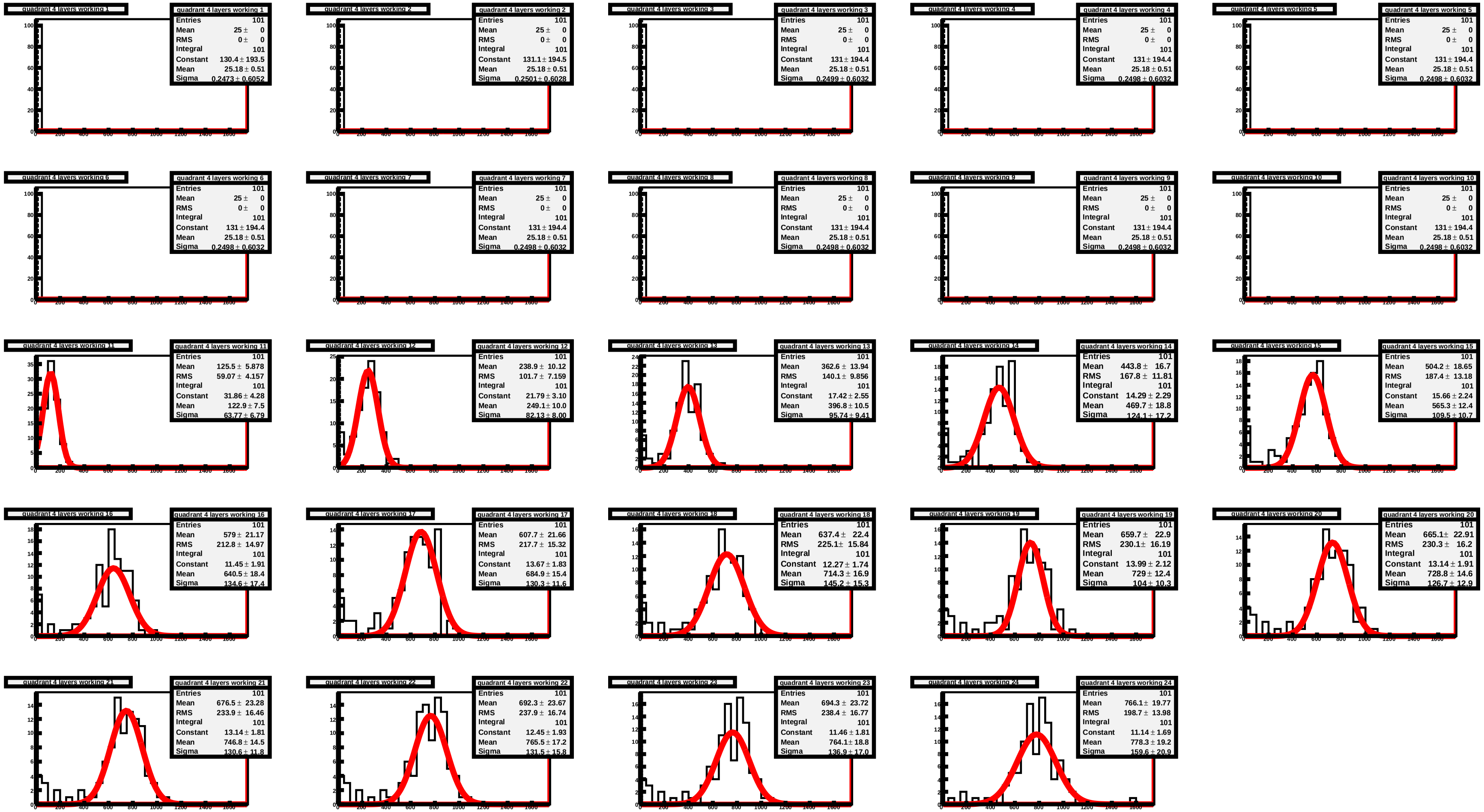

Figure B.7: Runs 114-119 at 5 GeV. Quadrant 1: The best energy resolution value is 14.2% at 19 working chips.

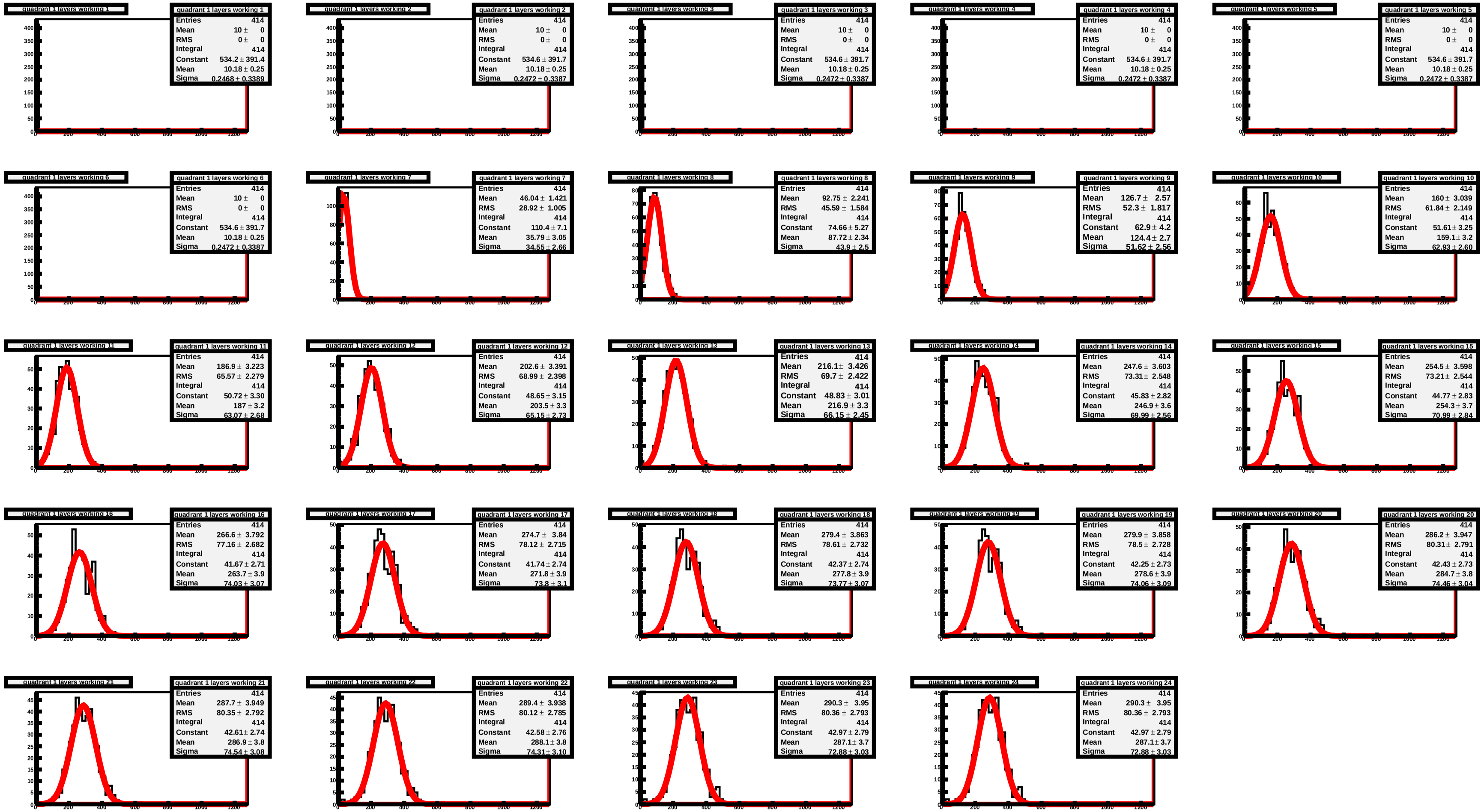

Figure B.8: Runs 93-98 at 2 GeV. Quadrant 0: The best energy resolution value is 25.4% at 23 working chips.

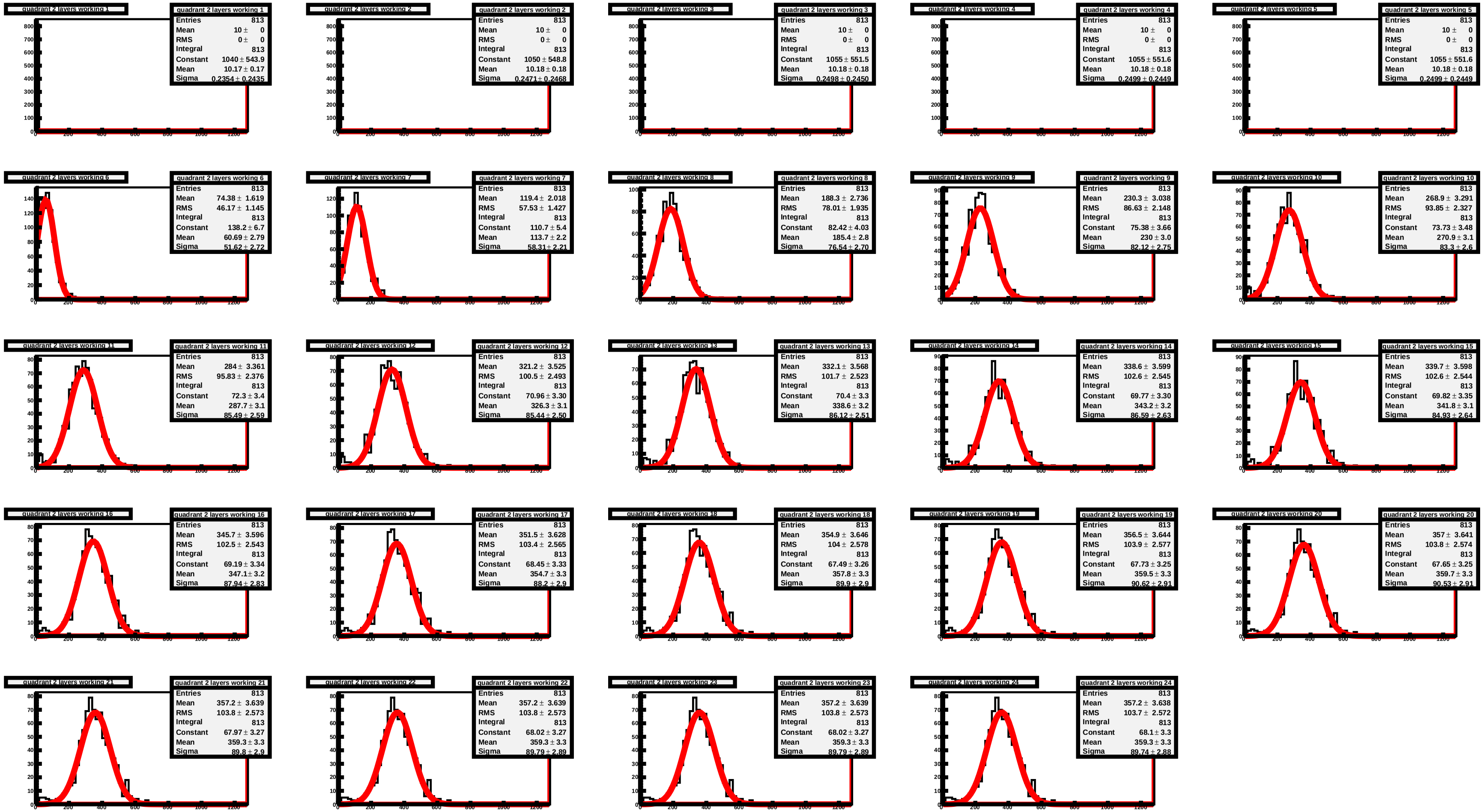

Figure B.9: Runs 93-98 at 2 GeV. Quadrant 3: The best energy resolution value is 24.7% at 24 working chips.

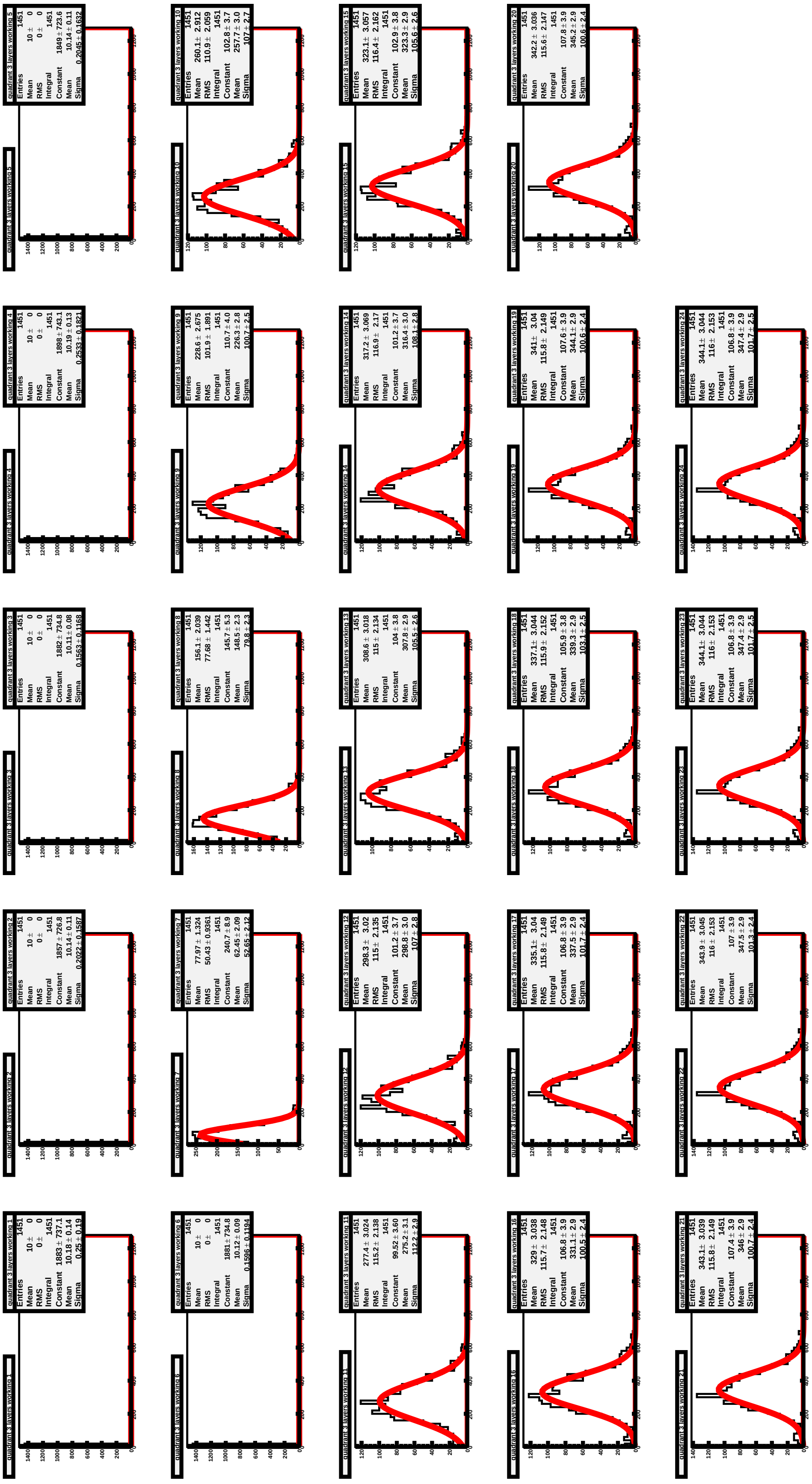

Figure B.10: Runs 93-98 at 2 GeV. Quadrant 2: The best energy resolution value is 29.1% at 23 working chips.

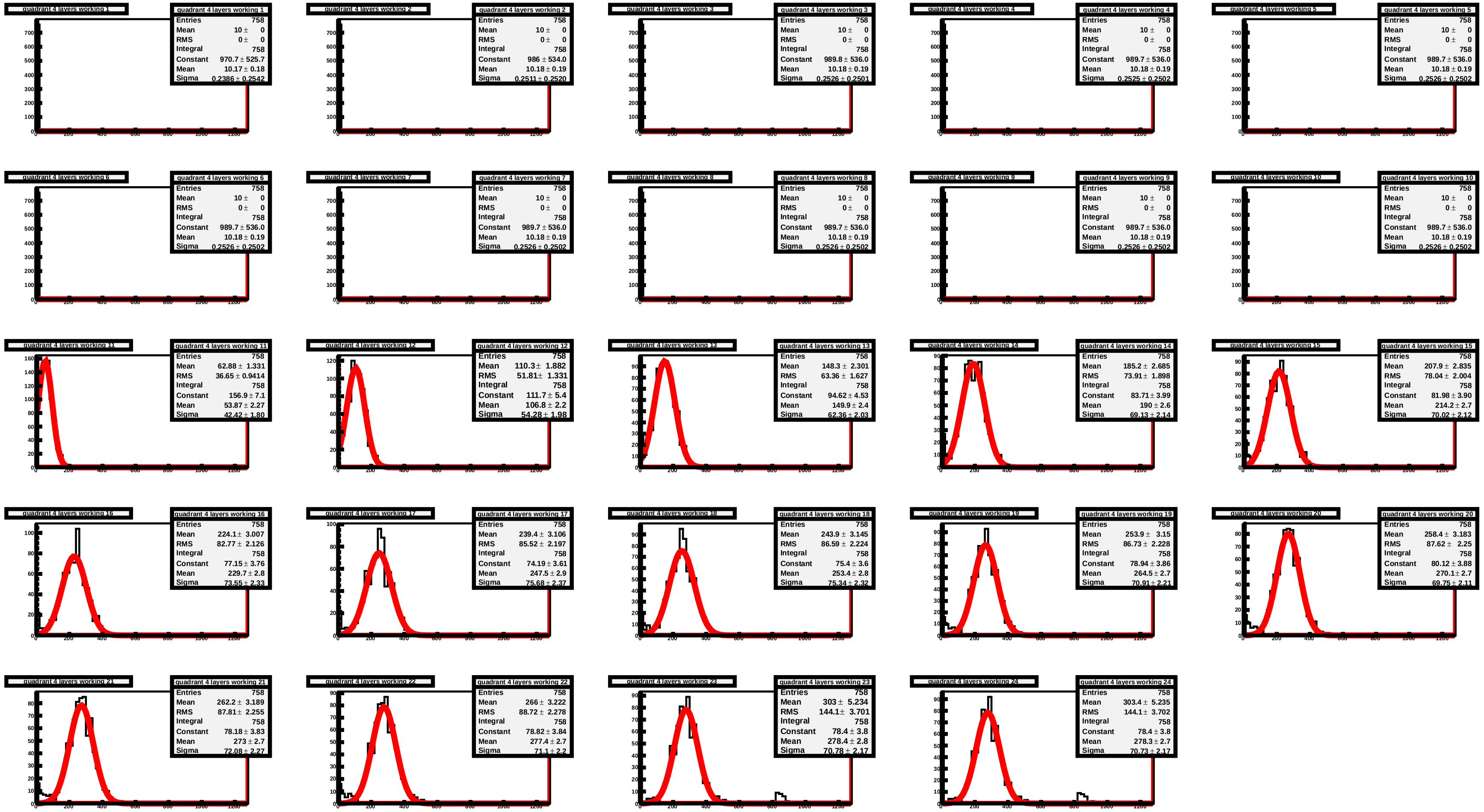

Figure B.11: Runs 93-98 at 2 GeV. Quadrant 1: The best energy resolution value is 25.4% at 24 working chips.

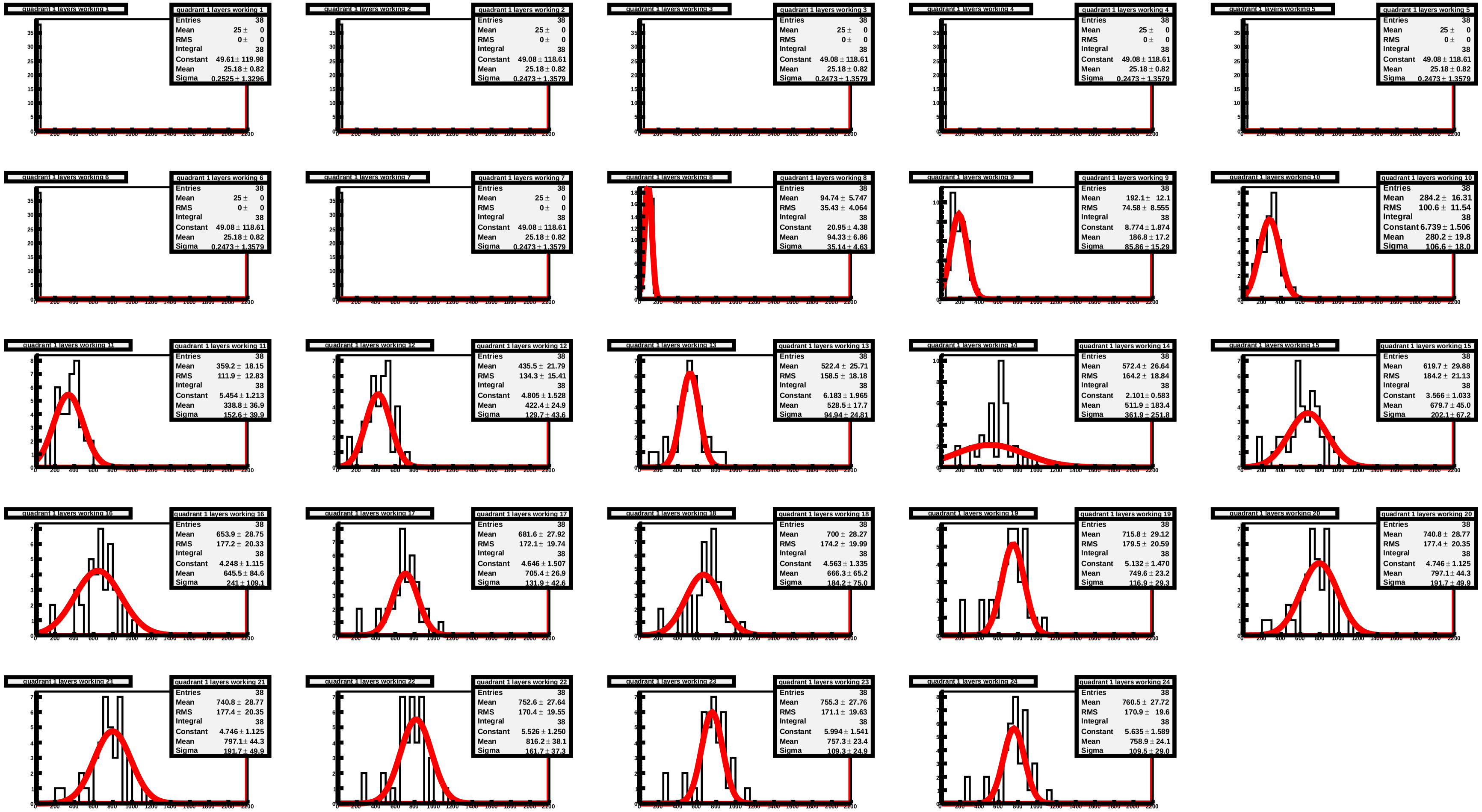

Figure B.12: Runs 114-119 at 5 GeV. Quadrant 0: The best energy resolution value is 14.4% at 24 working chips.

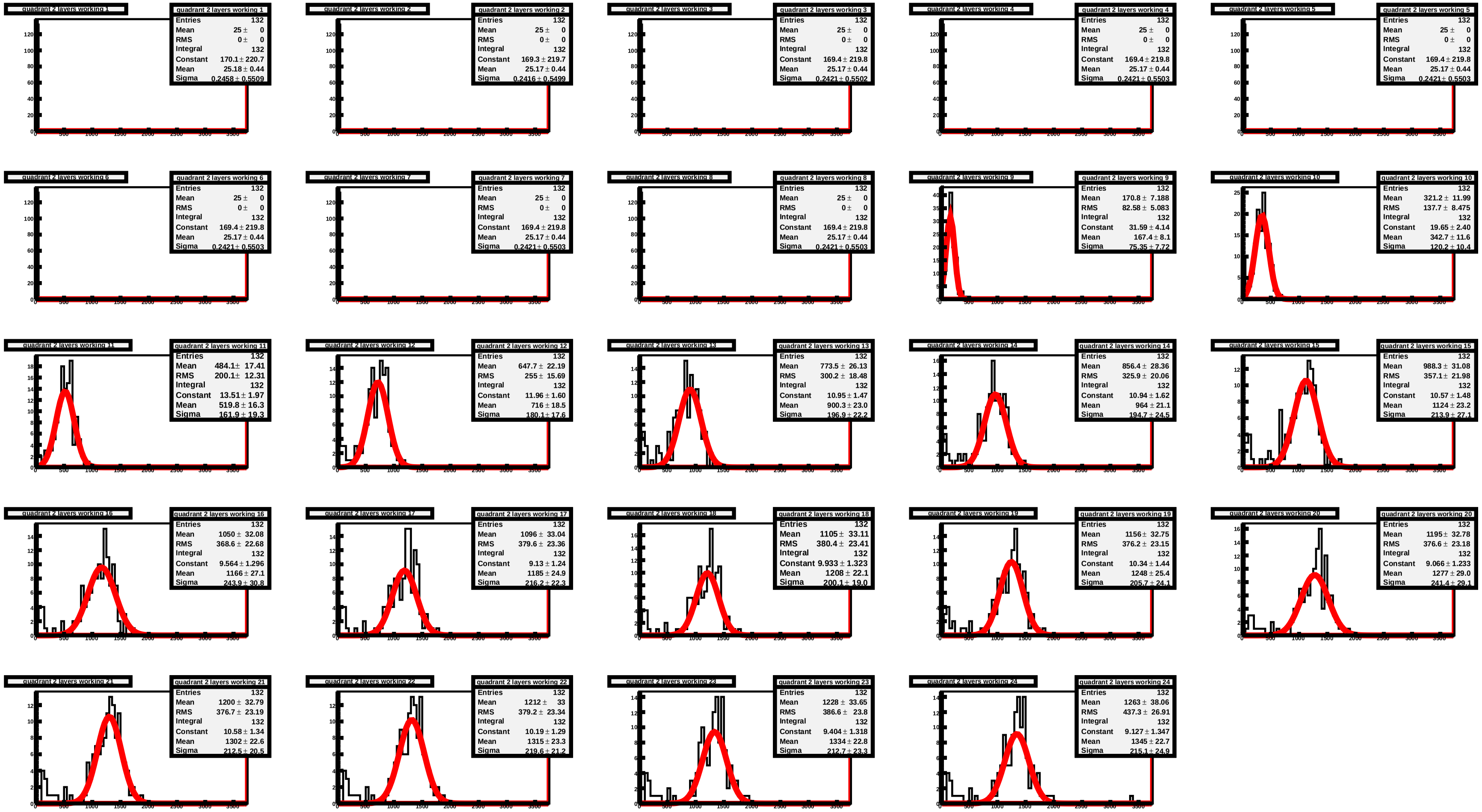

Figure B.13: Runs 114-119 at 5 GeV. Quadrant 3: The best energy resolution value is 15.9% at 23 working chips.

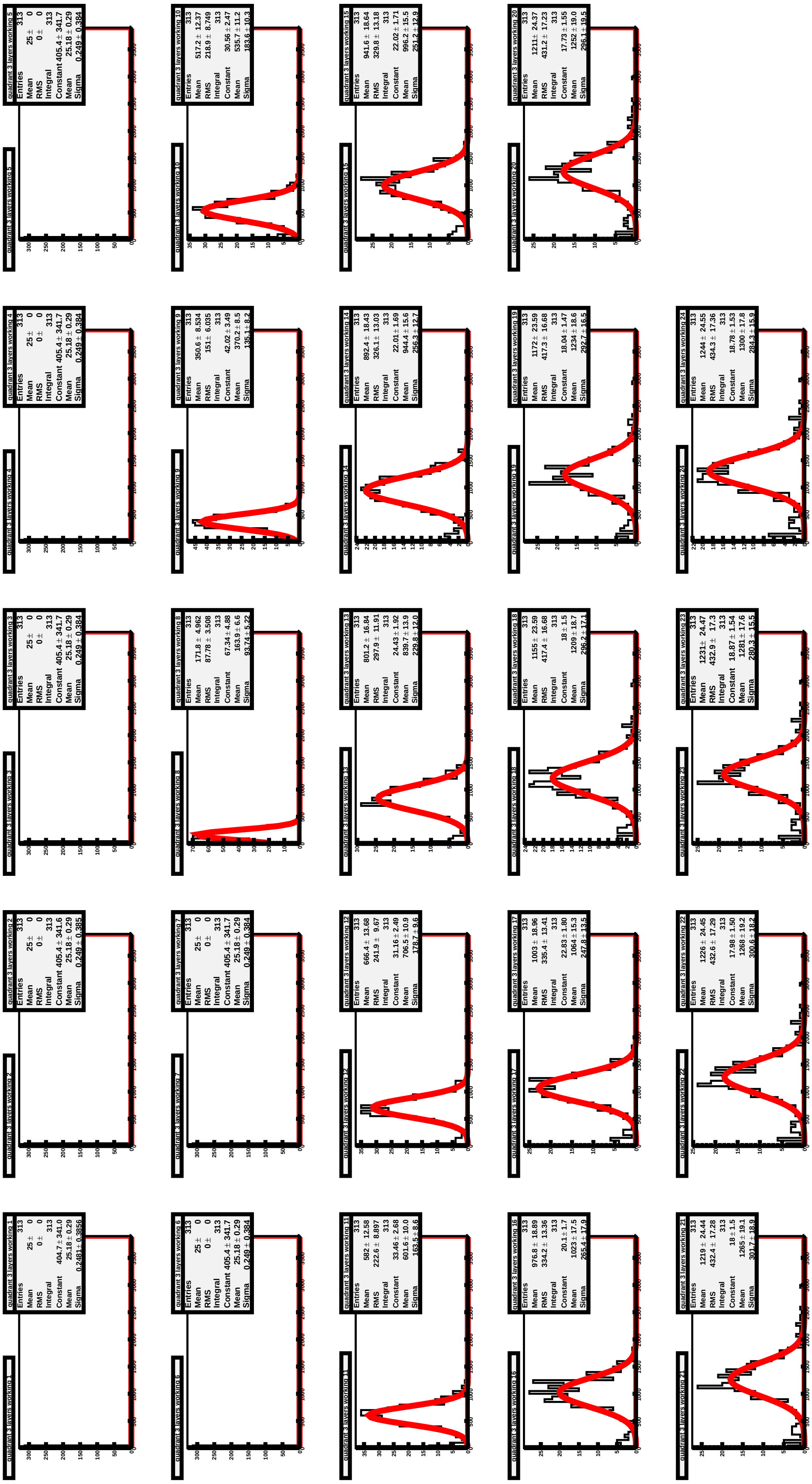

Figure B.14: Runs 114-119 at 5 GeV. Quadrant 2: The best energy resolution value is 21.8% at 24 working chips.

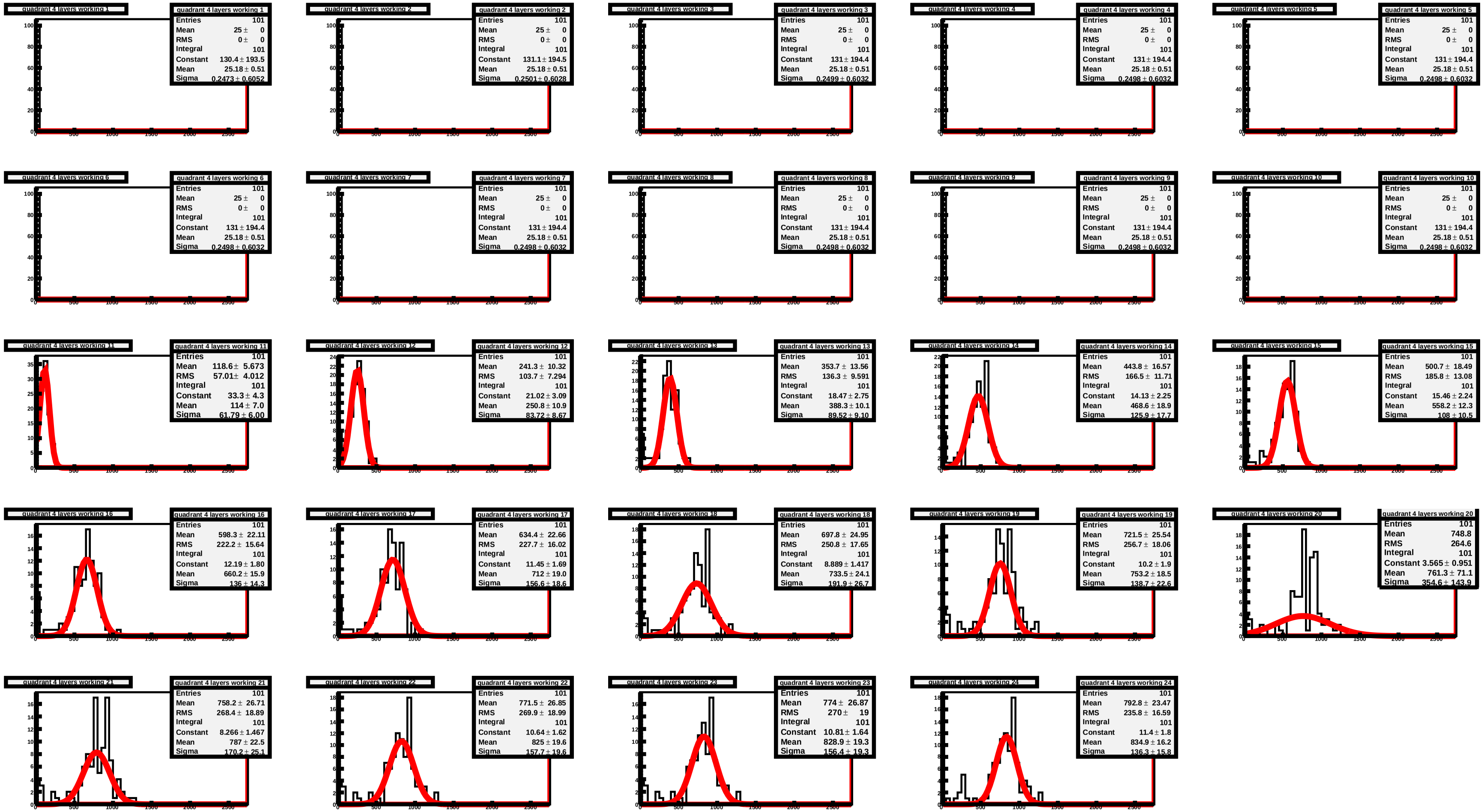

Figure B.15: Runs 114-119 at 5 GeV. Quadrant 1: The best energy resolution value is 16.3% at 24 working chips.

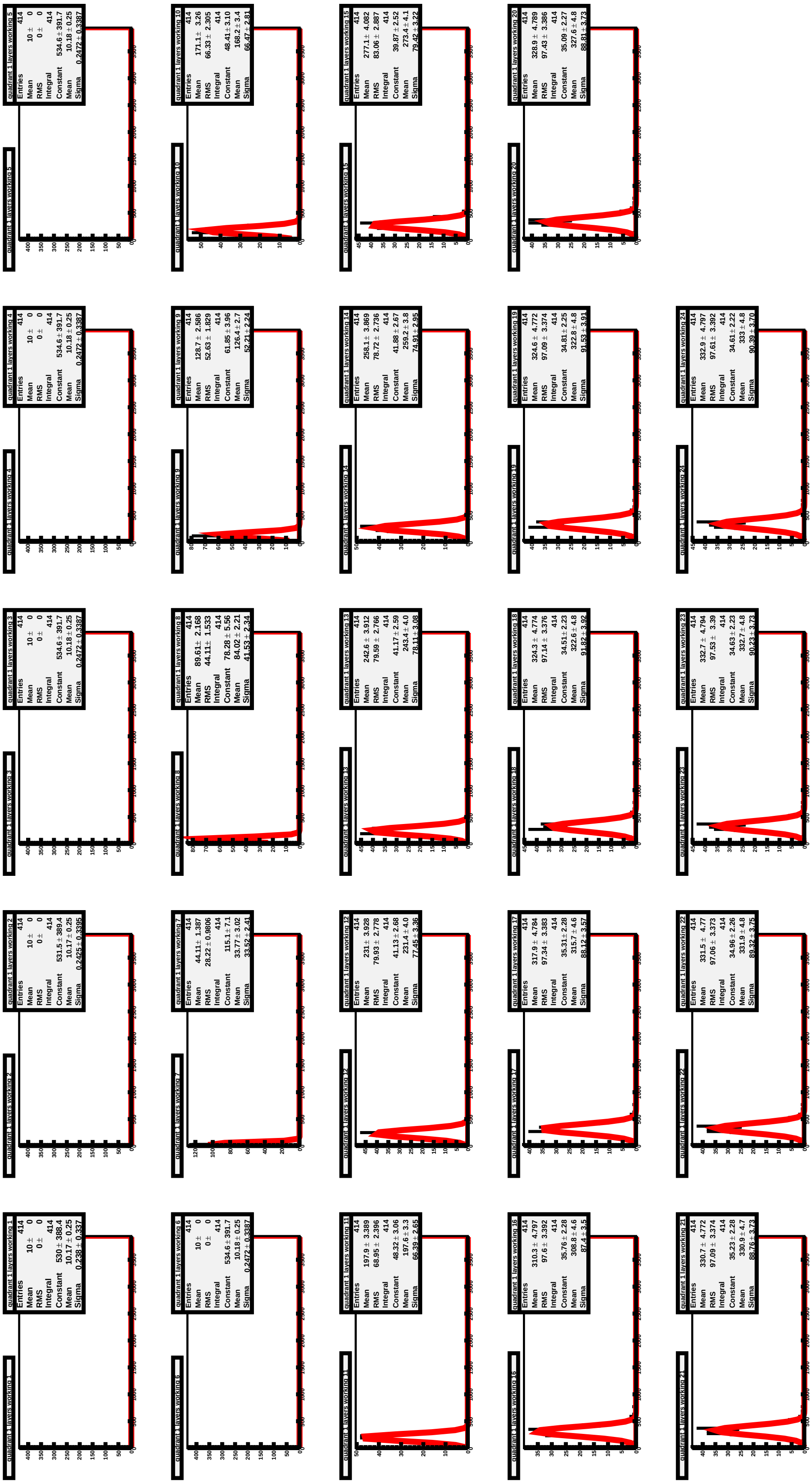

Figure B.16: Runs 93-98 at 2 GeV. Quadrant 0: The best energy resolution value is 26.8% at 21 working chips.

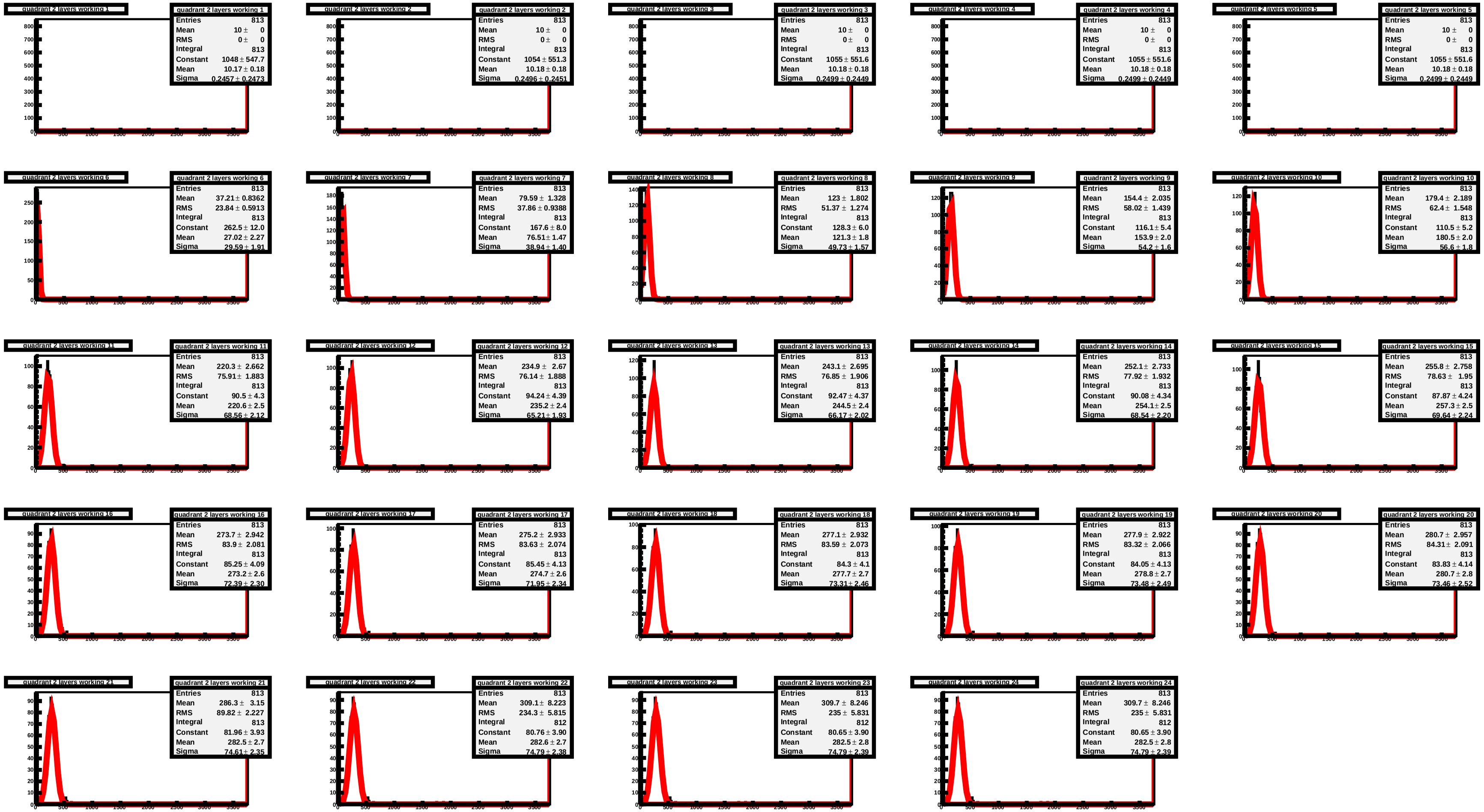

Figure B.17: Runs 93-98 at 2 GeV. Quadrant 3: The best energy resolution value is 26.1% at 20 working chips.

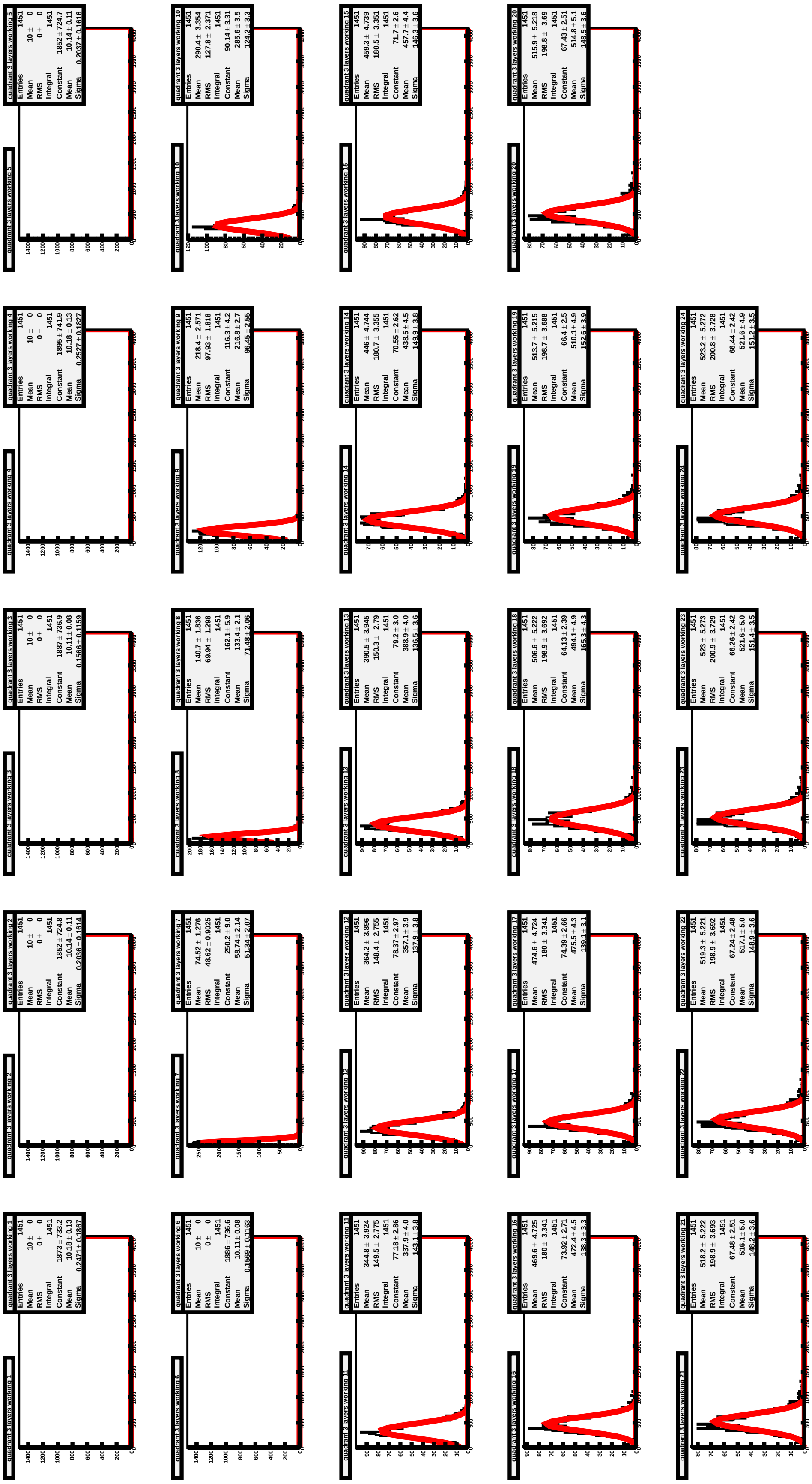

Figure B.18: Runs 93-98 at 2 GeV. Quadrant 2: The best energy resolution value is 28.7% at 21 working chips.

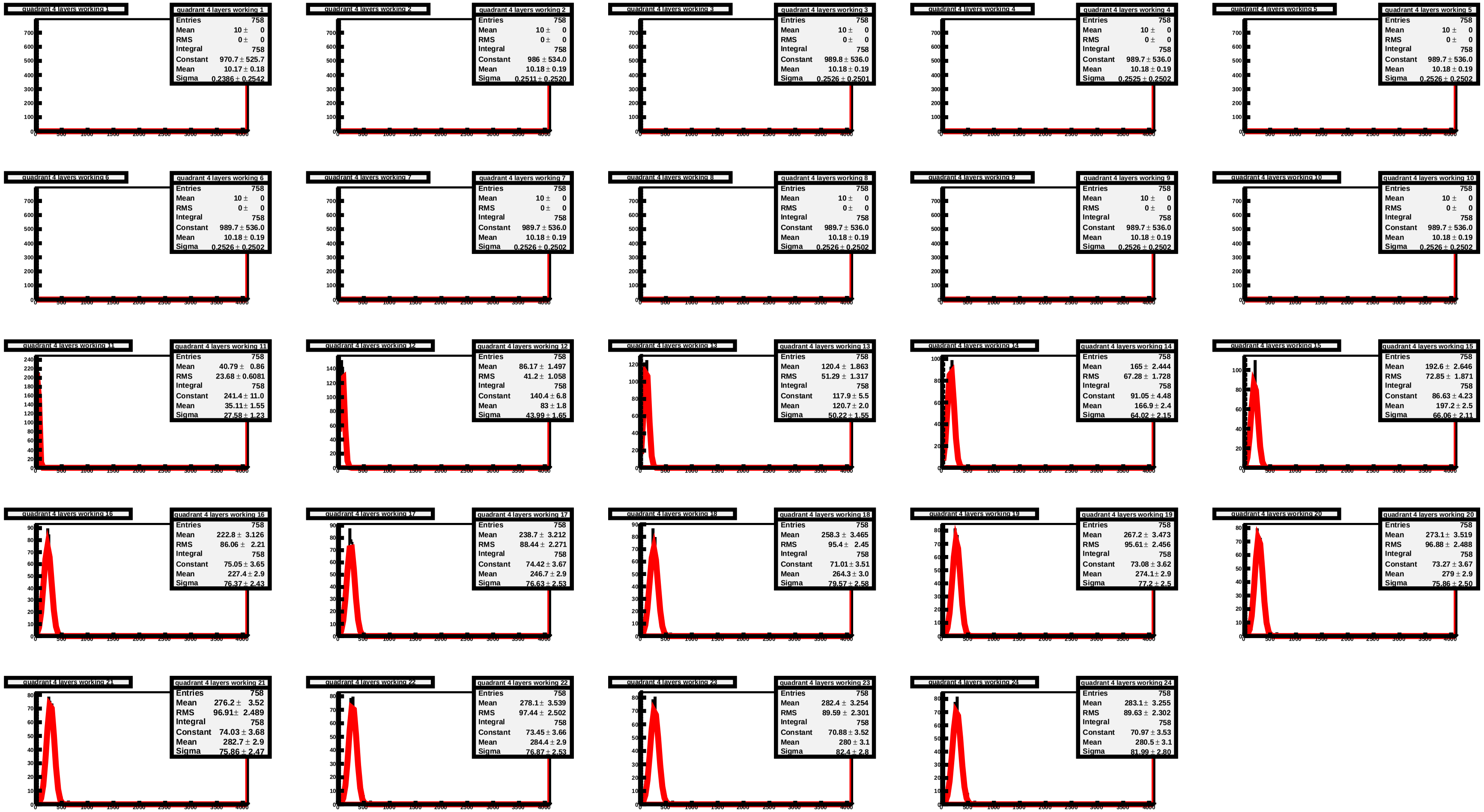

Figure B.19: Runs 93-98 at 2 GeV. Quadrant 1: The best energy resolution value is 26.8% at 21 working chips.

List of Figures

List of Tables